Dissertation

submitted to the
Combined Faculty of Natural Sciences and Mathematics
of the Ruperto-Carola-University of Heidelberg, Germany
for the degree of
Doctor of Natural Sciences

Put forward by
MSc. Physics Maximilian David Hartmann
born in Marburg an der Lahn

Oral examination: July 7th, 2021

Attosecond dynamics of strong-field generated ions

Referees: Prof. Dr. Thomas Pfeifer
Prof. Dr. Selim Jochim

Attosecond dynamics of strong-field generated ions — The main topic of this thesis is the time-resolved study of the dynamics occurring during the strong-field ionization of atoms and its application to the advancement of attosecond science. Using attosecond transient absorption spectroscopy (ATAS) in the regime where the near-infrared pump and the extreme ultraviolet probe pulses overlap, sub-cycle structures in the buildup of xenon ion population are observed and analyzed. It is established that these structures can serve as a timing tool to track dynamics with attosecond precision, thereby opening up a new domain of measurement schemes based on ATAS. At the same time, the line shapes of the observed resonances are used to reveal the dynamics of the time-dependent dipole moment of the atoms during the strong-field ionization. The investigation of the phase of the dipole moment suggests that a strong-field induced modification of the configuration interaction and dipole couplings between bound and continuum states occurs through polarization of the system. This phenomenon calls for an extended analytical description of strong-field ionization in multi-electron systems beyond the single-active electron approximation that takes laser-induced polarization of the atom into account.

Attosekunden Dynamik von in starken Feldern erzeugten Ionen — Das Hauptthema dieser Arbeit ist die zeitaufgelöste Untersuchung der Dynamiken, die während der Starkfeldionisation von Atomen auftreten und deren Anwendung zur Entwicklung neuer Messmethoden. Mit Hilfe der Attosekunden Transienten Absorptionsspektroskopie (ATAS) im Regime in dem die nah-infraroten Anregungspulse mit den extrem ultravioletten Abfragepulsen überlappen, werden subzyklus Strukturen beim Aufbau der Xenon-Ionen-Population beobachtet und analysiert. Es wird festgestellt, dass diese Strukturen als Zeitmessinstrument dienen können, um Dynamiken mit Attosekundenpräzision zu verfolgen, wodurch sich ein neuer Bereich von auf ATAS basierenden Messverfahren eröffnet. Gleichzeitig werden die Linienformen der beobachteten Resonanzen verwendet, um die Dynamik des zeitabhängigen Dipolmoments der Atome während der Starkfeldionisation aufzuzeigen. Die Untersuchung der Phase der Dipolantwort lässt vermuten, dass eine durch das Starkfeld induzierte Modifikation der Konfigurationswechselwirkung und Dipolkopplungen zwischen gebundenen und Kontinuumszuständen stattfindet. Dieses Phänomen erfordert eine Erweiterung der analytischen Beschreibung der Starkfeldionisation in Mehr-Elektronen-Systemen, die über die Annäherung durch ein einzelnes, aktives Elektron hinausgeht und die Polarisation des Atoms durch das Laserfeld miteinbezieht.

List of Publications

Parts of this work have been published or prepared in the following references:

M. Hartmann, V. Stooß, P. Birk, G.D. Borisova, C. Ott, and T. Pfeifer.
Attosecond precision in delay measurements using transient absorption spectroscopy.
Opt. Lett. **44**, 4749-4752 (2019). For more information see [1].

V. Stooß, M. Hartmann, P. Birk, G.D. Borisova, T. Ding, A. Blättermann, C. Ott, and T. Pfeifer.
XUV-beamline for attosecond transient absorption measurements featuring a broadband common beam-path time-delay unit and in situ reference spectrometer for high stability and sensitivity.
Rev. Sci. Instrum. **90**, 053108 (2019). For more information see [2].

Further publications with own contributions:

S. Hu, M. Hartmann, A. Harth, C. Ott, and T. Pfeifer.
Noise effects and the impact of detector responses on the characterization of extreme ultraviolet attosecond pulses.
Appl. Opt. **59**, 2121-2127 (2020). For more information see [3].

V. Stooß, P. Birk, A. Blättermann, M. Hartmann, G.D. Borisova, C. Ott and T. Pfeifer.
Strong-field-gated buildup of a Rydberg series.
Phys. Rev. Research **2**, 032041(R) (2020). For more information see [4].

P. Birk, V. Stooß, M. Hartmann, G.D. Borisova, A. Blättermann, T. Heldt, K. Bartschat, C. Ott and T. Pfeifer.
Attosecond transient absorption of a continuum threshold.
J. Phys. B: At. Mol. Opt. Phys. **53**, 124002 (2020). For more information see [5].

G.D. Borisova, V. Stooß, A. Dingeldey, A. Kaldun, T. Ding, P. Birk, M. Hartmann, T. Heldt, C. Ott and T. Pfeifer.
Strong-field-induced single and double ionization dynamics from single and double excitations in a two-electron atom.
J. Phys. Commun. **4**, 055012 (2020). For more information see [6].

D. Kolbasova, M. Hartmann, R. Jin, A. Blättermann, C. Ott, S.-K. Son, T. Pfeifer and R. Santra.
Probing ultrafast coherent dynamics in core-excited xenon by using attosecond XUV-NIR transient absorption spectroscopy.
Phys. Rev. A **103**, 043102 (2021). For more information see [7].

M. Rebholz, T. Ding, V. Despré, L. Aufleger, M. Hartmann, K. Meyer, V. Stooß, A. Magunia, D. Wachs, P. Birk, Y. Mi, G.D. Borisova, C. da Costa Castanheira, P. Rupprecht, G. Schmid, K. Schnorr, C. D. Schröter, R. Moshammer, Z.-H. Loh, A. R. Attar, S. R. Leone, T. Gaumnitz, H. J. Wörner, S. Roling, M. Butz, H. Zacharias, S. Düsterer, R. Treusch, G. Brenner, J. Vester, A. I. Kuleff, C. Ott, and T. Pfeifer.
All-XUV pump-probe transient absorption spectroscopy of the structural molecular dynamics of diiodomethane.
submitted to Phys. Rev. X (2021).

T. Ding, M. Rebholz, L. Aufleger, M. Hartmann, V. Stooß, A. Magunia, P. Birk, G.D. Borisova, D. Wachs, K. Meyer, C. da Costa Castanheira, P. Rupprecht, Y. Mi, A.R. Attar, T. Gaumnitz, Z.-H. Loh, S. Roling, M. Butz, H. Zacharias, S. Düsterer, R. Treusch, S.M. Cavaletto, C. Ott, and T. Pfeifer.
Measuring the frequency chirp of extreme-ultraviolet free-electron laser pulses by transient absorption spectroscopy.
Nat. Commun. **12**, 643 (2021). For more information see [8].

T. Ding, M. Rebholz, L. Aufleger, M. Hartmann, V. Stooß, A. Magunia, P. Birk, G.D. Borisova, D. Wachs, C. da Costa Castanheira, P. Rupprecht, Y. Mi, A.R. Attar, T. Gaumnitz, Z.-H. Loh, S. Roling, M. Butz, H. Zacharias, S. Düsterer, R. Treusch, C. Ott, and T. Pfeifer.
XUV-pump XUV-probe transient absorption spectroscopy at FELs.
Faraday Discuss. (2020). For more information see [9].

L. Aufleger, P. Friebel, P. Rupprecht, A. Magunia, T. Ding, M. Rebholz, M. Hartmann, V. Stooß, C. Ott, and T. Pfeifer.
Pulse length effects on autoionizing states under the influence of intense SASE XUV fields.
J. Phys. B: At. Mol. Opt. Phys. **53**, 234002 (2020). For more information see [10].

C. Ott, L. Aufleger, T. Ding, M. Rebholz, A. Magunia, M. Hartmann, V. Stooß, D. Wachs, P. Birk, G.D. Borisova, K. Meyer, P. Rupprecht, C. Da Costa Castanheira, R. Moshammer, A.R. Attar, T. Gaumnitz, Z.-H. Loh, S. Düsterer, R. Treusch, J. Ullrich, Y. Jiang, M. Meyer, P. Lambropoulos, and T. Pfeifer.
Strong-Field Extreme-Ultraviolet Dressing of Atomic Double Excitation.
Phys. Rev. Lett. **123**, 163201 (2019). For more information see [11].

T. Ding, M. Rebholz, L. Aufleger, M. Hartmann, K. Meyer, V. Stooß, A. Magunia, D. Wachs, P. Birk, Y. Mi, G.D. Borisova, C. da Costa Castanheira, P. Rupprecht, Z.-H. Loh, A. R. Attar, T. Gaumnitz, S. Roling, M. Butz, H. Zacharias, S. Düsterer, R. Treusch, S.M. Cavaletto, C. Ott, and T. Pfeifer.
Nonlinear Coherence Effects in Transient-Absorption Ion Spectroscopy with Stochastic Extreme-Ultraviolet Free-Electron Laser Pulses.
Phys. Rev. Lett. **123**, 103001 (2019). For more information see [12].

T. Ding, C. Ott, A. Kaldun, A. Blättermann, K. Meyer, V. Stooß, M. Rebholz, P. Birk, M. Hartmann, A. Brown, H. Van Der Hart, and T. Pfeifer.
Time-resolved four-wave-mixing spectroscopy for inner-valence transitions.
Opt. Lett. **41**, 709–712 (2016). For more information see [13].

Contents

1. Introduction

Human perception is governed by movement/motion [14] and drives our recurrent interest in dynamical processes. Dynamics are vital to understanding (learning) and to cope with the future (planning). Even apparently static objects are governed by intrinsic dynamics, that we are not aware of. The unseen changes escape our perception, because it is limited to certain scales in space and time (e.g. acoustic $\gtrsim$ 0.1 ms, visual $\gtrsim$ 0.1 s/ $\gtrsim 1'$), beyond which we need tools to assist our investigation. Testing the limits of our (machine-assisted) perception and pushing beyond is part of the scientific mission. As the archaeologists of earth and universe, the geologist analyzing unmoving rocks is ultimately interested in the dynamics of tectonic plates, while astronomers[1] are concerned with dynamics far beyond the time scales humanity as a whole can hope to experience (age of the universe $\approx 4 \cdot 10^{17}$ s).

The dynamics investigated in this work focus on the ionization of atoms and are diametrically opposed to such astronomical time and length scales. The evolution of atoms and molecules is governed by the motion of the electrons in these systems. Adopting the semi-classical Bohr model of the hydrogen atom, one can evaluate that the electron in the ground state of this two-body system orbits the nucleus (proton) at a distance of $0.529 \cdot 10^{-10}$ m at a velocity of $c/137$ and takes $\approx$ 150 as (1 as = 10^{-18} s) per revolution. These dynamics are omnipresent and shape our world as they govern the formation of chemical bonds and the evolution of chemical reactions [19]. With the goal to gain insight into everyday processes of nature it is therefore necessary to first understand these dynamics, knowledge that can then be used to control and steer atoms and molecules to our advantage.

Ultrashort, coherent pulses of light are a particularly versatile tool to trigger and probe electron dynamics on its natural attosecond time scale. Thanks to the discovery of Kerr lens mode-locking [20; 21] and the invention of chirped pulse amplification (CPA) [22] visible to infrared laser pulses can nowadays be amplified to millijoule pulse energies [23] and temporally compressed to a few femtoseconds [24]. The discovery of high-order harmonic generation (HHG) [25–27] was the final step to open the door to the attosecond domain [28–30], providing coherent, extreme ultraviolet (XUV) radiation in the form of attosecond pulse trains (APTs) [31] or isolated attosecond pulses (IAPs) [32]. Hereby, HHG enables the study of electron dynamics directly in the time domain, which typically requires photon energies in the range of 10–100 eV to excite valence and outer-core energy levels.

The experimental method used in this work is attosecond transient absorption spectroscopy (ATAS), which is an extension of conventional TAS using visible and infrared pulses [33] to the extreme ultraviolet (XUV) spectral range [34]. An ATAS measure-

[1] Except apparently those that treat us to such spectacular discoveries as those of exoplanets [15], a super-massive object at the center of our galaxy [16; 17] and gravitational waves [18].

ment consists in recording time-integrated, spectrally-dispersed XUV pulses that have interacted with an absorption target as a function of the delay with respect to an additional, typically near-infrared (NIR) control pulse. In the time domain, the XUV pulses excite the target atoms and thereby generate an oscillating, electric dipole, which decays by emitting a time-dependent response. Through interference with the incoming pulse, this response is imprinted onto the recorded spectra in the form of absorption lines [35; 36]. Two time-delay regimes between the XUV excitation pulse and a second control pulse have to be distinguished from one another. When the excitation comes first, the dressing pulse can manipulate the response of the atoms and thereby influence the absorption [37]. In this regime, ATAS is typically used to investigate the coupling between bound states [13], including strong-field-induced effects [38]. In contrast, when the dressing pulse precedes the XUV pulse, it can pump the system and its natural evolution is probed [39–41]. Through the dipole response, the all-optical approach of ATAS is directly sensitive to dynamics that occur close to (i.e., within) the atom, even during disruptive perturbations. The technique thus provides an opportunity to directly probe the bound-state dynamics of atoms and molecules interacting with strong laser fields. The resonance condition for absorption lines further ptovides charge-state specificity in ions [42] as well as site-selectivity [43] and structure sensitivity [44] in molecules.

Studying the perturbed dipole/polarization decay in neutral atoms is limited to moderate intensities ($\approx 10^{13}$ W/cm^2) before ionization completely suppresses the dipole emission. At higher intensities, one is either stuck with exploring the absorption of singly-excited helium or finds a way to turn the ionization into a tool [4; 45]. An alternative is to fully embrace the ionization as trigger of the dynamics. This approach is taken here.

But why would ramping up the intensity be crucial for the investigation of quantum dynamics? Quantum dynamics is the study of quantum systems driven out of equilibrium. By raising the intensity, the atomic potentials can be bent to the point where electrons become unbound, which is obviously far from equilibrium. Thus, by studying atoms, while they are being ionized provides a good vantage point to observe how the electronic wave function adapts to massive distortion. On top, with ATAS the atomic dipole acts as a probe susceptible to modifications of the wave function directly within the atom, which is an advantage over the detection of reaction products (e.g. electrons, ions) far away from the interaction region.

The motivation to study ionization dynamics in strong laser fields is manifold [46]. Its importance as first step in high harmonic generation [47; 48] is capital, but amongst others it also leads to phenomena such as above-threshold ionization (APT) [49], x-ray lasing [50], molecular dissociation [51; 52], non-sequential double-ionization (NSDI) [53] and is a crucial step in other methods e.g. laser induced electron diffraction (LIED) [54] or high-harmonic spectroscopy [55].

A simplified analytical description of strong-field ionization, that can be used to calculate sub-cycle ionization rates, was developed by Ammosov, Delone, and Krainov [56] more than three decades ago. But not until recently did the experimental methods catch up to study the process directly in the time domain. In this work, ATAS is applied to

the time-delay region between a near-infrared, femtosecond pump pulse and an XUV, attosecond probe pulse where both pulses overlap. This way, the strong-field generated ion population is extracted as it builds up. It was recently demonstrated, that this buildup is non-monotonous opposed to what is predicted by ADK theory [57]. Here, an additional line shape analysis of the ion absorption lines is used to gain a better understanding of the underlying dynamics of the dipole response of the target atoms. In addition it is found that the overshoots in the buildup can be exploited to track attosecond time delays in the XUV probe step.

This thesis is structured as follows: chapter 2 introduces the basic theoretical concepts used throughout the rest of this work. The focus lies on the description of ultrashort pulses of light, strong-field phenomena and the relevant concepts of quantum dynamics. It also lays out the fundamentals of the experimental methods, namely transient absorption spectroscopy and electron spectroscopy.

Chapter 3 presents the experimental equipment with which the measurements were carried out. Since the laser system and the experimental setup for attosecond absorption spectroscopy are covered in every PhD thesis from our group, the account tries to focus on the changes introduced and the personal experiences gained during this thesis. We published a detailed description of the setup and its features in [2]. The interested reader may also consult my co-workers and predecessors accounts [58–61]. Our first successful measurements that combine the technique of attosecond streaking spectroscopy with ATAS are presented alongside the time-of-flight photoelectron spectrometer. To the best of the authors knowledge, this is the first time that these techniques have been combined in a single measurement, an innovation that was facilitated by the design of a new hybrid absorption cell.

This is followed by the results chapters 4 to 6. Chapter 4 gives an introduction into the peculiarities of performing spectroscopy on strong-field generated ions and clarifies the atomic structure of the target, which is xenon throughout the following chapters. It also features an account of the data evaluation methods that were used. Chapter 5 contains the results on our study to use the overshoots in individual ion absorption lines as a timing tool to resolve attosecond delays. Using the dispersion in thin-foil aluminum filters, the group-delay dispersion imposed on the XUV probe pulses at the resonance positions was extracted with 5 as precision. Most parts of this chapter have been published in [1]. In addition, future applications of the new method are envisioned in a small outlook. The newest data of an NIR intensity scan are presented in chapter 6. The time-delay dependent analysis reveals unexpected sub-cycle oscillations in the asymmetry of the absorption line shapes. This asymmetry is subsequently linked to the initial phase of the time-dependent dipole response of the atoms. A few-level simulation allows to interpret these results as a field-dependent modification of the configuration interaction and dipole couplings in the atom. It is found that field-driven multi-electron dynamics need to be taken into consideration to account for these phase oscillations and their intensity dependence.

Finally, chapter 7 concludes this thesis by giving a summary and an outlook.

2. Theoretical background

This thesis deals with the interaction between light and atoms on ultrashort timescales. To set the scene for the following chapters, it is therefore necessary to lay out the theoretical background of the concepts that will be used later to analyze and interpret the experimental data. Starting with the description of ultrashort laser pulses and their interaction with matter in sections 2.1 and 2.2, the following chapter introduces the essential fundamentals of quantum dynamics in section 2.3 and concludes by detailing the experimental methods used later on, namely attosecond transient absorption spectroscopy and attosecond streaking, in sections 2.4 and 2.5.

2.1. Ultrashort pulses of light

As the shutter time of a camera determines the fastest events it can capture without blurring, the limiting factors to resolve quantum dynamics directly in the time domain are the duration of the triggers used to initiate and steer the experiments. Since the invention of lasers, the resulting coherent pulses of light have become the primary tool to drive the access to evermore shorter timescales. As a consequence scientists have pushed the pulse durations from the picosecond regime in the 1960s [62] to a few femtoseconds [24] in the optical and to tens of attoseconds [63; 64] in the extreme ultra-violet (XUV) spectral region. A good account of the properties and characteristics of ultrashort pulses is given in [65].

2.1.1. Mathematical description

The central quantity in the description of ultrashort laser pulses is the space and time dependent electric field $\mathbf{F}(t, \boldsymbol{x})$. Within the context of this thesis we can restrict ourselves to linearly polarized fields and focus on the temporal structure of laser pulses by studying the scalar quantity $F(t)$. Even though the electric field is in principle directly accessible and thus, a real quantity, it simplifies the theoretical treatment to extend $F(t)$ to the complex plane. The real-valued electric field can always be recovered by rejecting the imaginary part of its complex counterpart. The temporal field $F(t)$ is related to the spectral field $F(\omega)$ in the frequency domain via Fourier transformation, where ω is the angular frequency:

$$F(\omega) = \frac{1}{\sqrt{2\pi}} \int_{-\infty}^{\infty} F(t) e^{-i\omega t} \mathrm{d}t, \tag{2.1}$$

$$F(t) = \frac{1}{\sqrt{2\pi}} \int_{-\infty}^{\infty} F(\omega) e^{i\omega t} \mathrm{d}\omega. \tag{2.2}$$

The complex functions $F(t)$ and $F(\omega)$ fully characterize the shape of a laser pulse and can be rewritten in terms of amplitudes and phases:

$$F(t) = \mathcal{F}(t)\,\mathrm{e}^{\mathrm{i}\phi(t)}, \tag{2.3}$$

$$F(\omega) = \mathcal{F}(\omega)\,\mathrm{e}^{\mathrm{i}\varphi(\omega)}\,. \tag{2.4}$$

The intensity (in W/cm^2) of an ultrashort laser pulse is defined by averaging over one optical period T:

$$I(t) = \epsilon_0 cn\frac{1}{T}\int_{t-T/2}^{t+T/2} F^2(t')\mathrm{d}t' \approx \frac{1}{2}\epsilon_0 cn\mathcal{F}^2(t), \tag{2.5}$$

where ϵ_0, c and n are the dielectric permittivity, the vacuum speed of light and the refractive index of the propagation medium. The approximation with regard to the envelope is strictly applicable only when the amplitude $\mathcal{F}(t)$ is slowly varying compared to oscillations of the electric field. Of greater practical interest than the temporal intensity $I(t)$ is the spectral intensity $S(\omega)$:

$$S(\omega) = 2\epsilon_0 cn|F(\omega)|^2 = 2\epsilon_0 cn\mathcal{F}(\omega)^2. \tag{2.6}$$

Usually $S(\omega)$ is measured with slow detectors and therefore a time-averaged quantity. As equation 2.6 shows, the spectral phase $\varphi(\omega)$ is lost during the measurement and with it crucial information about the pulse shape. Common measures often used synonymously with the pulse duration and the spectral bandwidth are the full widths of the intensity functions at half their maximum value (FWHM) in their respective domain. Here, they shall be abbreviated by ΔT_{FWHM} for the pulse duration and $\Delta\omega_{FWHM}$ for the spectral width.

A common description of the spatial profile of a laser is using the model of Gaussian beams. Here, the intensity profile $I(r,z)$ along the the beam radius r and axis of propagation z is

$$I(r,z) = I_0\left(\frac{W_0}{W(z)}\right)^2 \exp\left(-\frac{2r^2}{W(z)^2}\right), \tag{2.7}$$

where I_0 is the intensity at the center of the beam waist W_0. The profile is completely described by the waist $W(z)$ and the Rayleigh range z_R:

$$W(z) = W_0\sqrt{1+(z/z_R)^2}, \qquad z_R = \pi W_0^2/\lambda\,, \tag{2.8}$$

where the latter is the distance to the focus at $z = 0$ at which the beam has expanded by a factor of $\sqrt{2}$. The angle of beam divergence in the far-field can be determined to be $\theta(z) = \arctan\left(z/z_R\right)$, which as a consequence is dependent of the wavelength λ. Integrating over the intensity profile establishes the relation between the time-averaged, on-axis intensity I_0 in the focus and the beam's total power P as

$$I_0 = \frac{2P}{\pi W_0^2}. \tag{2.9}$$

Time and frequency correspondence

The Fourier relationship between the representations of the electric field in the time and frequency domains has important implications for the generation of ultrashort light pulses. According to the *similarity theorem* of the Fourier transformation [66], a stretch in one domain results in a contraction plus an amplitude modification in the other domain. The result is an inverse relationship between ΔT_{FWHM} and $\Delta\omega_{FWHM}$, similar to the uncertainty principle of quantum physics. This behavior is best illustrated by considering a Gaussian pulse with standard deviation $\sigma_t = \sqrt{\alpha}$ in the time along with its Fourier transform in the frequency domain:

$$F(t) = \frac{1}{\sqrt{2\pi\alpha}} \exp\left(-\frac{t^2}{2\alpha}\right), \qquad F(\omega) = \sqrt{\frac{2\alpha}{\pi}} \exp\left(-2\alpha\omega^2\right). \tag{2.10}$$

The resulting width of $E(\omega)$ amounts to $\sigma_\omega = 1/\sqrt{4\alpha}$. The pulse duration and spectral bandwidth of the intensity functions can now be expressed in terms of the standard deviation of these Gaussian functions:

$$\Delta T_{FWHM} = 2\sqrt{\ln 2}\ \sigma_t = 2\sqrt{\ln 2\ \alpha}, \qquad \Delta\omega_{FWHM} = 2\sqrt{\ln 2}\ \sigma_\omega = \sqrt{\ln 2/\alpha}. \tag{2.11}$$

Consequently, ultrashort light pulses have to be supported by broadband spectra, while a narrow band laser in turn needs to run as stable as possible. This behavior is also illustrated in figure 2.1(II).

Temporal and spectral phases

A broad spectrum is needed to support a short laser pulse. But does that mean that every spectrum of sufficient width points to the existence of femtosecond pulses? If this were true, we could perform time resolved experiments by focusing sunlight into our targets. The logical fallacy is resolved by considering the temporal and spectral phases $\phi(t)$ and $\varphi(\omega)$. First $\phi(t)$ is expressed as a Taylor series:

$$\phi(t) = \sum_{n=0}^{\infty} \frac{\phi_n}{n!}\, t^n = \phi_{CEP} + \omega_c t + \Phi(t). \tag{2.12}$$

The ϕ_{CEP} is a constant phase that defines the offset between the oscillations of the electric field with carrier frequency ω_c and the peak of the amplitude function. Therefore the name *carrier-envelope phase* (CEP). The carrier or center frequency ω_c is not unambiguously defined. It is often assigned to the frequency at the maximum of the spectrum or defined as a weighted average of all spectral components. $\Phi(t)$ contains all higher phase orders ($n \geq 2$). Their effect becomes more intuitive by studying the instantaneous frequency of the pulses. The instantaneous frequency $\omega(t)$ of an oscillation is defined as the time derivative of the temporal phase:

$$\omega(t) = \frac{\mathrm{d}}{\mathrm{d}t}\phi(t) = \omega_c + \frac{\mathrm{d}}{\mathrm{d}t}\Phi(t). \tag{2.13}$$

If the phase has only linear terms $\Phi(t) = 0$, $\omega(t)$ is constant and the frequency does not change over the duration of the pulse. In this scenario, the pulse is called *Fourier transform limited* (FTL), because it has the shortest duration possible with the given spectrum. For $\Phi(t) \neq 0$ the pulse is said to be *chirped*. If the frequency increases (decreases) with time, the pulse is called up-chirped (down-chirped). The spectrum of a chirped pulse would in principle support a shorter pulse duration, if all frequency components were in phase. Propagation in media imprints a chirp upon pulses depending on the material properties.

The spectral phase $\varphi(\omega)$ can be expanded into a Taylor series as well:

$$\varphi(\omega) = \sum_{n=0}^{\infty} \frac{\varphi_n}{n!} (\omega - \omega_c)^n = \varphi_{CEP} + \tau_{GD}(\omega - \omega_c) + \frac{\mathrm{GDD}}{2}(\omega - \omega_c)^2 + \frac{\mathrm{TOD}}{6}(\omega - \omega_c)^3 + \dots \quad (2.14)$$

The first four orders of this expansion and their effect on the electric field are depicted in figure 2.1. The constant term φ_{CEP} is equal to the temporal phase offset ϕ_{CEP}. τ_{GD} is the group delay and determines the pulse's absolute position in time. Any higher phase orders introduce a frequency-dependent delay of different spectral components, which eventually smears out the pulse. The first of these contributions goes by the prominent name of *group-delay dispersion* (GDD). Higher orders ($\varphi_{\mathrm{TOD}}, \dots$) are simply referred to as *third-order dispersion* (TOD) and so on. As seen in in figure 2.1, positive (negative) GDD leads to an up-chirp (down-chirp) of the pulse, while positive (negative) TOD additionally produces post-pulses (pre-pulses).

2.1.2. Propagation effects

To study the propagation of ultrashort laser pulses in matter, we turn to the wave equation for the electric field $\mathbf{F}(t, \boldsymbol{x})$ in homogeneous media without currents and charges derived from Maxwell's equations:

$$\left(\nabla^2 - \frac{1}{c^2}\frac{\partial^2}{\partial t^2}\right) \mathbf{F}(t, x, y, z) = \mu_0 \frac{\partial^2}{\partial t^2}\mathbf{P}(t, x, y, z). \quad (2.15)$$

The polarization $\mathbf{P}$ accounts for the response of the medium. To study the impact of effects depending on the strength of the incident field, we expand $\mathbf{P}(t)$ in a Taylor series:

$$\mathbf{P}(t) = \epsilon_0 \left(\chi^{(1)}\mathbf{F}(t) + \chi^{(2)}\mathbf{F}(t)\mathbf{F}(t) + \chi^{(3)}\mathbf{F}(t)\mathbf{F}(t)\mathbf{F}(t) + \dots\right). \quad (2.16)$$

The different $\chi^{(n)}$ are the n^{th}-order susceptibilities and are in general tensors of order $n+1$. As for the spatial dependence of the electric field, which has to be taken into account in the following, plane waves propagating in z-direction in a medium with wave vector $k(\omega)$ are assumed as a solution to equation 2.15:

$$F(\omega, z) = \mathcal{F}(\omega, 0) \exp(-\mathrm{i}k(\omega)z). \quad (2.17)$$

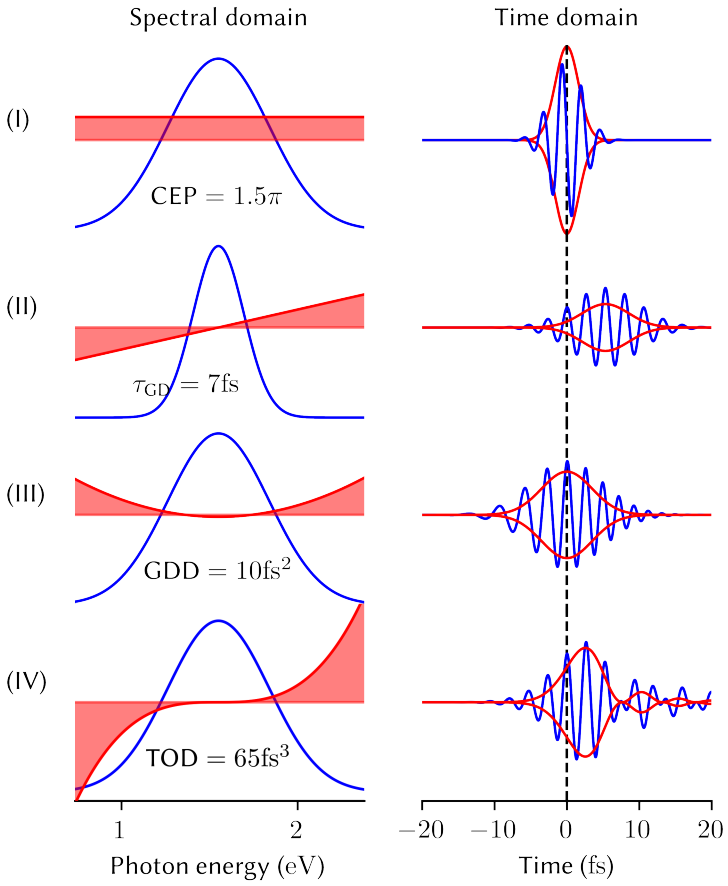

Figure 2.1.: Pulses in the spectral and temporal domain. (left) Spectral amplitude (blue) and different spectral phase orders (red). (right) The resulting electric field (blue) with its envelope (red) in the time domain. Top to bottom: (I) Fourier transform-limited pulse with constant phase $\varphi_{CEP} = \frac{3}{2}\pi$: The peak of the field does not coincide with the peak of the envelope. (II) Linear phase and narrow spectrum: the pulse's absolute position in time is shifted and it is longer although still in its FTL. (III) Quadratic phase: the pulse is up-chirped and stretched in time. (IV) Cubic phase: the chirp induces post-pulses and a small delay.

Dispersion

The first order susceptibility $\chi^{(1)}$, related to the refractive index $n = \sqrt{1+\chi^{(1)}}$, is responsible for dispersion[1]. Inside a medium with a frequency-dependent refractive index, the wave vector becomes a frequency-dependent propagation factor

$$k(\omega) = n(\omega)\frac{\omega}{c}. \tag{2.18}$$

For most transparent materials e.g. glasses, the refractive index is monotonously increasing with frequency ($\mathrm{d}n/\mathrm{d}\omega \geq 0$) which leads to *normal* dispersion. As a result, the phase of the pulse is modified upon propagation, because the phase fronts of each spectral component travel at the phase velocity

$$v_p(\omega_0) = \left.\frac{\omega}{k}\right|_{\omega_0} = \frac{c}{n(\omega_0)}. \tag{2.19}$$

[1]Both n and χ can contain a complex component which leads to absorption, but for now we focus on transparent optical elements, such as lenses and prisms (and air), where this contribution is negligible.

The velocity of the whole pulse in turn is governed by the group velocity

$$v_g = \frac{\mathrm{d}\omega}{\mathrm{d}k} = v_p \left(1 + \frac{\omega}{n}\frac{\mathrm{d}n}{\mathrm{d}\omega}\right)^{-1}. \tag{2.20}$$

Finally, the group velocity dispersion (GVD) determines how the spread of the different spectral components affects the pulse:

$$\mathrm{GVD}(\omega_0) = \left.\frac{\mathrm{d}^2\omega}{\mathrm{d}k^2}\right|_{\omega_0} = \frac{\mathrm{d}}{\mathrm{d}\omega}\left(\frac{1}{v_g(\omega)}\right)_{w_0} = \frac{2}{c}\left(\frac{\partial n}{\partial \omega}\right)_{w_0} + \frac{\omega_0}{c}\left(\frac{\partial^2 n}{\partial \omega^2}\right)_{w_0}. \tag{2.21}$$

The GVD is a material property that can be used to evaluate the chirp that is imprinted onto a laser pulse in a medium, because it is a measure of the GDD per unit length, i.e. GDD = GVD · L, where L is the length of the medium. In normal-dispersive materials the low frequency components of the pulse traverse the medium faster than the high frequency components, which causes an up-chirp. Since the chirp induced by unavoidable optics stretches the pulses, dispersion compensation with elements with *anomalous* dispersion ($\mathrm{d}n/\mathrm{d}\omega < 0$) is crucial in the work with ultrashort pulses. In general, two types of compressors are employed to achieve a down-chirp. Grating and prism compressors use the angular dispersion in these elements, which can be arranged such that the total setup has negative dispersion. The second approach uses chirped mirrors, special dielectric mirrors composed of thin multi-layer stacks, which can be designed to have negative GDD.

Non-linear processes

Because the strength of higher-order susceptibilities $\chi^{(n)}$ is continuously decreasing, the observation of non-linear, optical effects requires high field strengths. The simplest nonlinear effect of second order is second harmonic generation (SHG). As the name states, it converts two photons with energy $\hbar\omega_0$ to one photon with twice the energy $\hbar\omega_{SHG} = 2\hbar\omega_0$ and is often used in pulse characterization.

The third-order non-linearities induced by $\chi^{(3)}$ cause (besides other effects) the propagation medium to exhibit an intensity-dependent refractive index:

$$n(\mathbf{r}, t) = n_0 + n_2 I(\mathbf{r}, t). \tag{2.22}$$

This is the so called optical Kerr effect, which is the source of *self-focusing* and *self-phase modulation* (SPM). In self-focusing, the time- and space-dependent refractive index $n(\mathbf{r}, t)$ creates a lensing effect, due to the spatial intensity profile of the laser beam. This is made use of in femtosecond Ti:sapphire laser oscillators. The Kerr effect inside the laser crystal now benefits high-power pulsed operation over cw operation by inducing fewer losses per cavity round-trip on high intensity pulses. This technique called Kerr lens mode-locking, revolutionized the generation of ultrashort laser pulses and gave solid

state lasers the upper hand over dye lasers. Since it uses no active element, it enables passive mode-locking. Self-phase modulation is a process used for spectral broadening in hollow-core fibers. Focusing short pulses into a gas filled capillary, the temporal intensity profile of the pulses leads to a temporal-dependence of the refractive index of the gas. Thus the propagation through the gas induces a modulation of the phase of the pulse (equation 2.12). By analyzing the instantaneous frequency (equation 2.13) while assuming a Gaussian intensity function $I(t) = I_0 \exp\left(-(t/\tau)^2\right)$,

$$\omega(t) = \omega_c - \frac{\omega_c}{c}\frac{\mathrm{d}}{\mathrm{d}t}n(t) = \omega_c + \frac{\omega_c}{c}\frac{2I_0 n_2}{\tau^2} t\mathrm{e}^{-(t/\tau)^2}, \tag{2.23}$$

we see that new frequency components lower/higher than ω_c are produced in the leading/trailing edge of the pulse. Together with a chirped mirror compressor this technique is routinely used to generate high-power pulses with sub-10 fs duration.

2.2. Strong-field phenomena

The potential to resolve fast processes is not the only feature of short laser pulses. Their temporal compression in combination with spatial focusing boost the intensity available in experiments and provides means to explore strong-field effects. What does this imply?

In the context of this thesis, a field is considered strong, when its influence is compareble to the internal forces of the target atom. In the ground state of the hydrogen atom the electric field experienced by the electron and the definition of the atomic unit of field strength is $5.14 \cdot 10^{11}$ V/m. The femtosecond laser pulses used in this work reach peak intensities on the order of 10^{14} W/cm^2 or field strengths of $\approx 3 \cdot 10^{10}$ V/m. At these field strengths, the pulses can distort atomic potentials quite substantially, which is the source of a rich palette of phenomena.

One important notion to consider in strong fields, is the ponderomotive force $F = -e\mathcal{F}(t)$ which a pulse exerts on a free electron. While the pulse last, it leads to a quiver motion of the electron in the oscillating field. The time-averaged kinetic energy of this motion, the so-called ponderomotive potential U_p, is of particular interest:

$$U_p = \frac{e^2\mathcal{F}_0^2}{4m_e\omega^2} = \frac{m_e\left\langle v_{osc}^2(t)\right\rangle}{2}, \tag{2.24}$$

a pulse property, related to but distinct from the pulse intensity. It is the starting point for the theory of electrons in strong fields which was pioneered by Keldysh [67]. He concluded that ionization in a low-intensity laser field has multi-photon character, while it is governed by tunneling at high intensities. To quantify this assessment, he introduced what is now known as the Keldysh parameter:

$$\gamma = \sqrt{\frac{I_p}{2U_p}} = \omega\tau_{tunnel}, \tag{2.25}$$

where I_p is the ionization potential of the atom. For $\gamma < 1$, when the ponderomotive potential is equal to or stronger than the atomic binding potential, tunneling dominates. The Keldysh parameter can also be interpreted as the lasers frequency multiplied by the tunneling time τ_{tunnel}[68][2], which is the time the electron spends under the barrier in classical considerations (see figure 2.2 II). When the field is sufficiently strong, the tunnel barrier and the tunneling time becomes short enough for the electron to escape during a single half cycle, before the field reverses direction. The strong frequency dependence of the ponderomotive potential can also be interpreted in this sense: the longer the wavelength of the driving field, the longer each interval with a low tunnel barrier. In the limit of $\gamma > 1$, the field is too weak to bend the atomic potential and only (perturbative) multi-photon ionization takes place. The Keldysh parameter is therefore often used to distinguish the weak-field from the strong-field regime.

2.2.1. Stark effect

The ponderomotive potential is also important as the continuum limit of the AC-Stark effect. High-lying Rydberg states and the threshold are shifted up in energy according to U_p. For ionization purposes, this additional energy has to be overcome to liberate an electron, while the pulse acts upon the atom. Within the context of ATAS, this transient shift in energy is imprinted on the observed transition lines[71; 72] and can be used to retrieve the pulse duration and intensity *in situ* [73].

For an arbitrary quantum state, the Stark shift is the change in energy that results from placing the particle in an electric field. Optical fields are by nature oscillating fields at their extreme and so the AC-Stark effect describes the shift of atomic levels under the influence of laser pulses. For the case of non-degenerate quantum states, perturbation theory yields [74]

$$\Delta E_{AC} = -\frac{\alpha}{4}\mathcal{F}^2(t) \quad \text{and} \quad \Delta E_{inst} = -\frac{\alpha}{2}F^2(t). \tag{2.26}$$

Here, α is the optical polarizability, while $\mathcal{F}(t)$ is the envelope and $F(t)$ is the electric field itself. With ΔE_{inst} the concept of an instantaneous Stark effect that follows directly the field itself and not its envelope, is introduced.

The polarizabilities above are actually tensorial quantities, but their reduction to scalars is valid for centrosymmetric targets in linear polarized fields, as is the case in our experiments. Nonetheless their calculation is a cumbersome business as the following form of the Stark shift of the state $|\psi_0\rangle$ illustrates [75]:

$$\Delta E = -\sum_n \frac{|\langle\psi_0|\hat{\boldsymbol{d}}\boldsymbol{F}|\psi_n\rangle|^2}{E_n - E_0}. \tag{2.27}$$

[2] This is only an illustrative model and by no means a contribution to the vivid debate on tunneling times (i.a. [69; 70]).

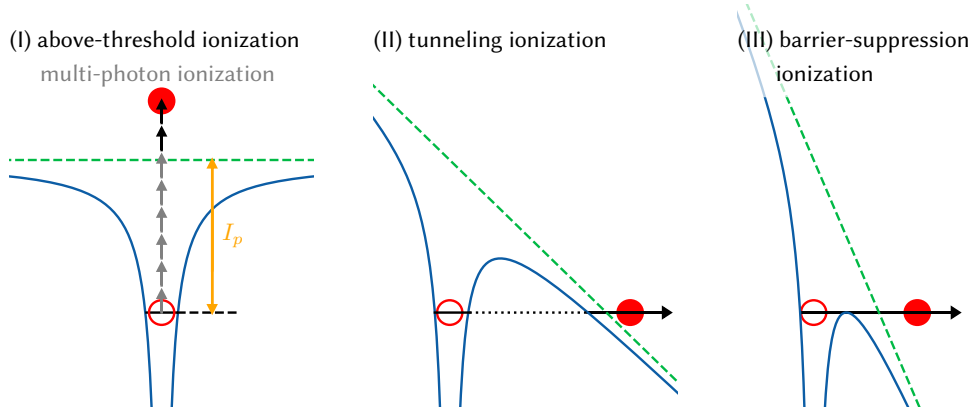

Figure 2.2.: Different regimes of ionization. (I) At the lowest intensities ($\gamma \gg 1$) multi-photon ionization (MPI) prevails. With higher intensities the atom can absorb excess photons through above-threshold ionization (ATI) which leads to characteristic peaks in the electron spectrum. (II) When the ponderomotive potential becomes comparable to the ionization potential I_p ($\gamma < 1$) tunneling through the barrier is possible. (III) Finally for $\gamma \ll 1$, the barrier is completely suppressed. In the BSI regime the ionization rate scales linearly with intensity.

The accurate calculation of polarizabilities in principle requires a sum over a wide spectrum of possible electronic configurations of the target. Therefore, reliable data on polarizabilities is scarce except for specific use cases, such as optical ion clocks [76], where special efforts in this direction are undertaken.

2.2.2. Strong-field ionization

Keldysh's theory of ionization was soon refined by Perelomov, Popov, and Terent'ev [77] (PPT), Faisal [78] and Reiss [79] (KFR) and Ammosov, Delone, and Krainov [56] (ADK) to yield better quantitative ionization rates. A more recent development was presented by Yudin and Ivanov [80, 81]. Experimental realizations followed [82; 83] and as the intensity of lasers increased, the theory was further complemented by a description of over-the-barrier (OBI) or barrier-suppression ionization (BSI)[46; 84], where the field bends the atomic potential so much that the bound states become free. A broad review on this development is given in [85]. The Keldysh parameter accessed in the experiments here is $\gamma_{exp} \lesssim 1$. In the further discussion, strong-field ionization is therefore treated in the sense of tunneling ionization and implies a strong perturbation of the atomic potentials.

ADK ionization rates

To model strong-field ionization (SFI) the ADK [56] ionization rate is used in this work:

$$\Gamma_{ADK}(t) = \sqrt{\left(\frac{2e}{n^*}\right)\frac{1}{2\pi n^*}}\frac{(2l+1)(l+|m|)!}{2^{|m|}(|m|)!(l-|m|)!}I_p\left(\frac{3\mathcal{F}(t)}{\pi(2I_p)^{3/2}}\right)^{1/2}\times \left(\frac{2(2I_p)^{3/2}}{\mathcal{F}(t)}\right)^{2n^*-|m|-1}\exp\left[-\frac{2(2I_p)^{3/2}}{3\mathcal{F}(t)}\right]. \tag{2.28}$$

The parameters in the ionization rate Γ_{ADK} that define the target are the effective principal quantum number $n^* = Z/\sqrt{2I_p}$, the angular momentum and magnetic quantum numbers l and m, the ionization potential I_p and charge number Z. The effective principle quantum number takes into account the treatment of the atom in the single-active electron approximation and incorporates the screening of the core due to the inactive electrons. Using the envelope of the field $\mathcal{F}(t)$ yields a cycle-averaged ionization rate, but replacing it with the pulses' electric field $\mathcal{F}(t) \longrightarrow F(t)$ and dropping the last factor in braces on the first line of equation 2.28 $\left(3\mathcal{F}(t)/\pi(2I_p)^{3/2}\right)^{1/2}$, we obtain an instantaneous/subcycle ionization rate[3]. From the exponent in the last factor, which includes the electric field, we see that Γ_{ADK} depends highly non-linearly on the input pulses. For a better illustration, the ionization of xenon is visualized in figure 2.3 with 5 fs pulses with different peak intensities. The non-linear behavior restricts the ionization to the peaks of the strongest half-cycles of the electric field. Furthermore, the window between negligible ionization and saturation covers only a range of $0.7\text{–}2 \cdot 10^{14}\,\mathrm{W/cm^2}$ and depletion of the ground state shifts the ionization towards the leading edge of the pulse for higher intensity.

To model saturation and depletion in ionization or even incorporate double ionization, we can consider the evolution in the populations $P_0(t)$, $P_+(t)$ and $P_{2+}(t)$ of the neutral, singly- and doubly-ionized species by solving the following coupled differential equations numerically:

$$\begin{aligned} \dot{P}_0 &= -\ \Gamma^0_{ADK}P_0 \\ \dot{P}_+ &= \Gamma^0_{ADK}P_0 - \Gamma^+_{ADK}P_+ \\ \dot{P}_{2+} &= \Gamma^+_{ADK}P_+, \end{aligned} \tag{2.29}$$

starting with $P_0(0) = 1$ ($P_+(0) = P_{2+}(0) = 1$), where $\Gamma^0_{ADK}(t)$ and $\Gamma^+_{ADK}(t)$ denote the instantaneous ionization rates of the neutral and the singly-charged ion, respectively. The number of ionization events at any given moment $I(t)$, dubbed the *fractional ionization* in figure 2.3, is then given by differentiation of the ion population with respect to time.

[3] Although the notion of a deterministic ionization rate is not quite quantummechanically correct [86].

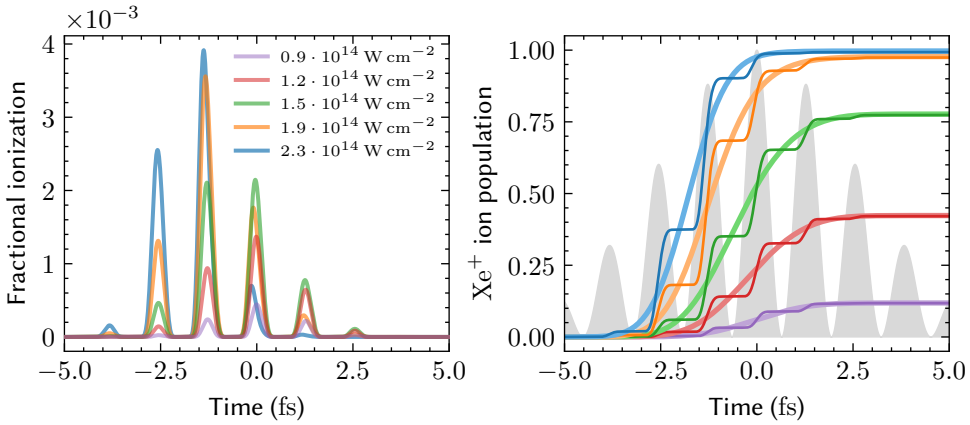

Figure 2.3.: SFI of xenon according to the ADK model with a 5 fs laser pulse with different peak intensities. (left) Fractional ionization of the neutral at any given point in time. The ionization is restricted to the peaks of the field and shifts towards the leading edge of the pulse with higher intensity. (right) Buildup of ion population within the pulse. The steps are a signature of the sub-cycle nature in the ionization, the pale sigmoidal curves show the cycle-averaged ionization (see text). In the backdrop the squared electric field $|F(t)|^2$ is depicted as a reference.

Reversible polarization dynamics

The very nature of strong-field ionization implies that the ground state is substantially modified and the field-free atomic wave functions are no longer eigenstates of the total atom-field Hamiltonian. This means that during the interaction of the pulse with the atom, a strong mixing of states occurs, which results in an induced polarization of the atom (compare equation 2.27). While the tunneling in the ionization process means that some of the population in the neutral ground state is eventually lost, another part is transiently redistributed across the spectrum of bound states and may relax back once the half-cycle is over. Since the presence of a valence hole is generally attributed to ionization, the transient polarization of the atom may lead to reversible ionization dynamics opposed to the irreversible, monotonically increasing dynamics observed in figure 2.3. As we will see in chapter 4, this effect—scrutinized in detail by Sabbar et al. [57]—leads to overshoots in the ion population buildup. Some hints at this effect can be traced back to earlier experimental [24; 87] and theoretical [88; 89] studies.

2.2.3. High-harmonic generation

Probably the most important implication of strong-field ionization is that it constitutes the first step in high-harmonic generation (HHG). Driven by tabletop laser sources in the visible and infrared spectral regions, HHG can be used to generate extreme-ultraviolet (XUV) radiation in the form of attosecond pulse trains (APTs) or even isolated attosecond pulses (IAPs). The semi-classical three-step model first proposed by Corkum [47]

and sketched in figure 2.4, best illustrates this phenomenon. Irradiating a gas target with a driving field strong enough to induce SFI, some electrons [4] may tunnel out of their binding potential (I). Once freed, they are accelerated by the intense driving field (II) and have a chance to recombine with the parent ion (III). Upon recombination the binding energy plus the excess kinetic energy is released as a high-energetic photon. Since the release and return times for a successful recollision are confined to a fraction of the driving field cycle which is in the femtosecond range, the emitted radiation inherently features attosecond duration. The HHG process is non-perturbative in the sense of perturbation theory where higher order non-linearities are more suppressed. Instead the emitted light has constant intensity over a large range of photon energies up to the cut-off energy $E_{cutoff} = I_p + 3.17U_p$. An attosecond pulse is released every half-cycle of the laser field which results in the formation of an APT for driving pulses with several cycles. The spectra of these pulses interfere and lead to the formation of discrete, odd harmonics with a separation of $2\omega_{laser}$.

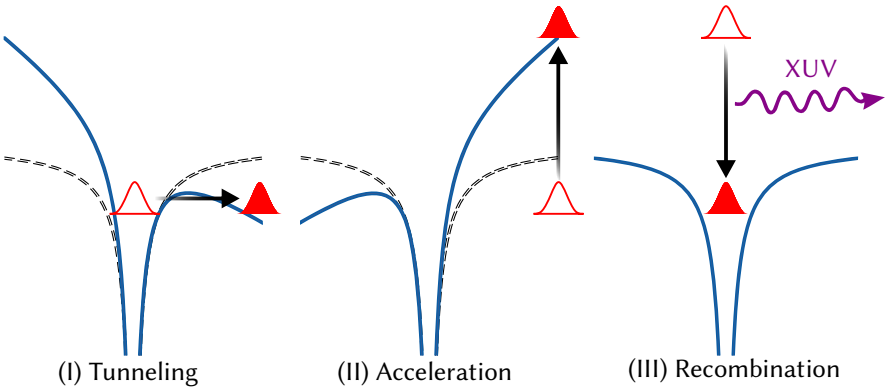

Figure 2.4.: Illustration of the three step model of high-harmonic generation. The laser field bends the atomic potential, which allows some electrons (red) to tunnel free (step I). As the laser field passes, its slope changes sign and the electrons are accelerated back towards the atomic core (step II), where they have a certain chance to recombine with the parent ion. The excess energy is released as a high energetic photon (step III).

To generate macroscopic amounts of XUV light the radiation of many microscopic emitters has to be added coherently. This is accomplished by taking the phase matching between the driving pulse and the generated radiation into account [89]. The quantum description of HHG pioneered by Lewenstein et al. [48] has to be considered to balance the propagation phase of the electrons in the continuum with the geometrical phase of the laser focus and the dispersion in the partially ionized medium. Experimentally this is realized by adjusting the target position with respect to the focus and the gas pressure of the conversion medium. HHG radiation is particularly well-suited for time-resolved

[4] Actually, part of the electronic wave function.

measurements, because the individual attosecond pulses that are produced every half-cycle, are intrinsically phase locked to the driving laser and no jitter-prone, artificial synchronization is needed.

While HHG allows the generation of broadband, attosecond pulses at high photon energies with "cheap" tabletop experiments, the conversion efficiency is quite low at $\mathcal{O}\left(10^{-6}\right)$ which sets limits on the XUV pulse energies in the nJ range[5] that can safely be treated perturbatively. For the study of nonlinear effects in the XUV spectral range, free-electron laser (FEL) facilities with µJ pulse energies are more suitable. The contribution by the author to such experiments that were carried out at the Free electron LASer in Hamburg (FLASH) in the course of two beam-times is not discussed here, but is reported in [8–12].

2.3. Quantum dynamics

In the case of non-relativistic quantum mechanics, it is the Schrödinger equation that governs the dynamics of any quantum system:

$$\mathrm{i}\hbar\frac{\mathrm{d}}{\mathrm{d}t}\left|\psi\right\rangle = \hat{\boldsymbol{H}}\left|\psi\right\rangle. \tag{2.30}$$

In this notation, the Schrödinger equation is quite general as it does not specify the Hilbert space in which the Hamiltonian $\hat{\boldsymbol{H}}$ operates.

Within this work, we focus on states, whose resonace energies lie far above the ionization threshold of the atom. As a result, they are embedded into the continua of states of free electrons. Their couplings with the continuum states as well as other bound states manifest as dynamics that we wish to observe and explain. This section is dedicated to the tools and method we need for this venture.

2.3.1. Laser-coupled few-level systems

To gain insight into quantum systems too complex for analytical treatment, simulations provide means to access their dynamics on a numerical basis. If the model is a good enough approximation of the real, physical object, simulations allow to interpret the experimental data and deepen our understanding of the experiment as a whole.

For the study of dynamics induced by explicitly time-dependent fields such as the XUV and NIR pulses it is convenient to split the total Hamiltonian $\hat{\boldsymbol{H}} = \hat{\boldsymbol{H}}_0 + \hat{\boldsymbol{V}}$ into two parts and treat the problem in the interaction picture with the atomic Hamiltonian of the unperturbed, time-independent system $\hat{\boldsymbol{H}}_0$ and the (light-matter) interaction operator $\hat{\boldsymbol{V}}$.

[5] Of course the range of systems is broad. Low-repetition-rate/high-power setups differ from high-repetition-rate/low-power systems. An overview is given in [90].

We expand the wave function in a set of energy eigenstates of the unperturbed system

$$|\psi\rangle = \sum_{i=1}^{n} c_i |i\rangle , \tag{2.31}$$

where the $c_i = c_i(t)$ are the complex-valued, time-dependent state coefficients. The time-dependence of the system is thus carried both by the wave function and the interaction operator $\hat{\boldsymbol{V}}(t)$. The evolution of the system is then found by determining the evolution of the n state coefficients[6]. To this end, the Hamiltonian on its part is represented by a $n \times n$ matrix, with the energies $E_i = \langle i|\hat{\boldsymbol{H}}_0|i\rangle$ on the diagonal and the couplings on the off-diagonals $V_{ij} = \langle i|\hat{\boldsymbol{V}}|j\rangle$.

$$\hat{\boldsymbol{H}} = \begin{pmatrix} E_1 & V_{12} & & V_{1n} \\ V_{21} & E_2 & & V_{2n} \\ & & \ddots & \\ V_{n1} & V_{n2} & & E_n \end{pmatrix} \quad , \quad |\psi\rangle = \begin{pmatrix} c_1(t) \\ c_2(t) \\ \vdots \\ c_n(t) \end{pmatrix} . \tag{2.32}$$

In the dipole-approximation in length gauge $\hat{\boldsymbol{V}} = \hat{\boldsymbol{d}}\boldsymbol{F}(t)$, the matrix elements V_{ij} evaluate to

$$V_{ij} = \langle i|\hat{\boldsymbol{V}}(t)|j\rangle = \langle i|\hat{\boldsymbol{d}}|j\rangle\, F(t) = d_{ij}F(t) \tag{2.33}$$

and are explicitly time-dependent, with the dipole operator $\hat{\boldsymbol{d}}$, the electric field $F(t)$ and the dipole matrix elements d_{ij}, which we already encountered in the context of Stark shifts (equation 2.27).

Numerical solution

Given the initial wave function $|\psi(t = 0)\rangle = |\psi_0\rangle$, the formal solution of the Schrödinger equation is

$$|\psi(t)\rangle = \mathrm{e}^{-\frac{\mathrm{i}}{\hbar}\hat{H}t}\,|\psi_0\rangle . \tag{2.34}$$

From linear algebra we know that for a diagonal operator the matrix exponential reduces to a diagonal matrix of exponentials of the matrix elements. Thus, for the field-free Hamiltonian alone equation 2.34 reduces to a trivial phase evolution of each eigenstate according to its energy. For the complete Hamiltonian including the interaction term, we can use this trick by transforming into the eigensystem of $\hat{\boldsymbol{H}}$, such that it is in diagonal form with its eigenvalues as entries. Transforming the wave function accordingly, the propagation is again trivial.

To determine the complete evolution of the coefficients $c_i(t)$, we perform the propagation in discrete time steps Δt. This is necessary, because the interaction operator is explicitly time-dependent such that the transformation and propagation in its eigensys-

[6] It should be noted that this treatment is restricted to the description of pure quantum states. For mixed states, a representation in terms of density matrices and their evolution is needed [35; 91]. We deliberately accept this limitation of our models for the sake of simplicity.

tem are only valid, if it can be assumed to be stationary during the time interval Δt. With $t_k = k\Delta t$ as the total propagation time, the following sequence of operations is performed in each of the k steps:

1. Field free evolution.
$$c_i(t + \Delta t) = \mathrm{e}^{-\frac{i}{\hbar} E_i \Delta t}\, c_i(t)$$

2. Transformation into the eigensystem of the interaction. T is the transformation matrix which has the eigenvectors of $\widetilde{\boldsymbol{V}}$ as columns.
$$\widetilde{\boldsymbol{V}} = \mathrm{diag}(\widetilde{V}_1 \ldots \widetilde{V}_n) = T^\dagger \hat{\boldsymbol{V}} T, \qquad |\widetilde{\psi}\rangle = T^\dagger |\psi\rangle$$

3. Propagation in the interaction basis.
$$\tilde{c}_i(t + \Delta t) = \mathrm{e}^{-\frac{i}{\hbar} \widetilde{V}_i \Delta t}\, \tilde{c}_i(t)$$

4. Back transformation into the energy basis.
$$|\psi\rangle = T\, |\widetilde{\psi}\rangle$$

To facilitate the calculations, atomic units (see appendix A.1) are used in these simulations.

Because the XUV pulses used in the experiment are so weak that they only present a small perturbation to the field-free Hamiltonian they can also be handeled within the framework of perturbation theory to be discussed below. In this case $\hat{\boldsymbol{V}}$ includes only the dressing through the NIR pulses.

As we will see in the next section 2.4, the quantity we are interested in is the atomic dipole. It can be computed in the simulation from the state coefficients c_i:

$$d(t) = \langle \psi | \hat{\boldsymbol{d}} | \psi \rangle = \sum_e c_g^*(t) c_e(t) d_{ge} + \text{c.c.}, \tag{2.35}$$

where c_g is the coefficient of the ground state, while the sum runs over all excited states.

Taking the ground state into account is crucial, since we want to model ion dynamics, which are initiated by ionization of the neutral target. The ionic ground state population is therefore zero before the pump pulse arrives. This is taken into account in the simulations by population of the ground state according to the ADK ionization rate from section 2.2.2 including depletion of the neutral atoms. Since we evolve the state coefficients c_i and not their population $|c_i|^2$ the square root of the fractional ionization at any given moment is added in each time step to the ground-state state-coefficients.

For more details on the implementation of such few-level systems, the reader is kindly referred to the more evolved accounts given in [61] and [58].

Time-dependent perturbation theory

Since the field strengths of pulses created through HHG are weak compared to the electronic binding potentials of atoms, they can be treated as a minor perturbation to the field-free atomic Hamiltonian $\hat{\boldsymbol{H}} = \hat{\boldsymbol{H}}_0 + \lambda\hat{\boldsymbol{V}}$. Here, the factor $\lambda \ll 1$ is the perturbation strength. With this in mind, time-dependent perturbation theory as covered in textbooks such as [92] and [93] can be used to express the wavefunction of the perturbed system in the eigenbasis of the field-free Hamiltonian $\hat{\boldsymbol{H}}_0$:

$$|\psi\rangle = \sum_k c_k(t)\, \mathrm{e}^{-\frac{\mathrm{i}E_k t}{\hbar}} \left|\psi_k^0\right\rangle, \tag{2.36}$$

The result for the state coefficients $c_m^{(1)}$ up to 1st order can be found to be:

$$c_m^{(1)}(t) = -\frac{\mathrm{i}}{\hbar}\sum_k c_k^{(0)} \int_0^t \mathrm{e}^{\mathrm{i}\omega_{mk}t'} \left\langle \psi_m^0 \middle| \hat{\boldsymbol{V}} \middle| \psi_k^0 \right\rangle \mathrm{d}t', \tag{2.37}$$

where $\omega_{mk} = \frac{E_m - E_k}{\hbar}$ and the $c_k^{(0)}$ are the stationary solution of the 0th order.

With this result, we can turn back to consider the case of excitation of an atom through a weak XUV pulse $F_{XUV}(t)$. In the dipole-approximation, the perturbation is $\hat{\boldsymbol{V}}(t) = \hat{\boldsymbol{d}}\boldsymbol{F}_{XUV}(t)$, with the dipole operator $\hat{\boldsymbol{d}}$. The HHG pulses with their attosecond durations usually present the shortest timescale in the observed dynamics, which justifies the simplification of treating them as Dirac-δ pulses i.e. $F_{XUV}(t) = F_0\delta(t - \tau)$. This way we can perform the integral in equation 2.37 analytically and obtain as a final result for the evolution of the state coefficients

$$c_m(t) = c_m^{(0)} + \frac{1}{\mathrm{i}\hbar}F_0 \sum_k c_k^{(0)}\, \mathrm{e}^{\mathrm{i}\omega_{mk}\tau} d_{mk}. \tag{2.38}$$

2.3.2. Fano's theory of autoionization

In atomic physics the theory of a discrete state embedded into a continuum is inextricably linked to the name of Ugo Fano, who first formulated it to explain the asymmetric shape of absorption lines seen in arc spectra of noble gases [94][7]. Even though it is developed purely time-independent, his theory is insofar indispensable for this thesis, as it sheds light onto the couplings that have to be considered when dealing with asymmetric line shapes. In-depth accounts of the complete formalism are given in [96; 97].

The whole treatment starts with a single discrete, bound state $|b\rangle$ and a set of continuum states $|c_E\rangle$, all of which are eigenstates of the atomic Hamiltonian $\hat{\boldsymbol{H}}_0$. The energy $E_b = \langle b|\hat{\boldsymbol{H}}_0|b\rangle$ of the discrete state lies above the ionization threshold and within the continuous range of energies of the continuum states $E\delta(E' - E) = \langle c_{E'}|\hat{\boldsymbol{H}}_0|c_E\rangle$. So far these configurations don't interact. Their coupling is introduced via the configuration

[7] Translation of the original Italian article: [95].

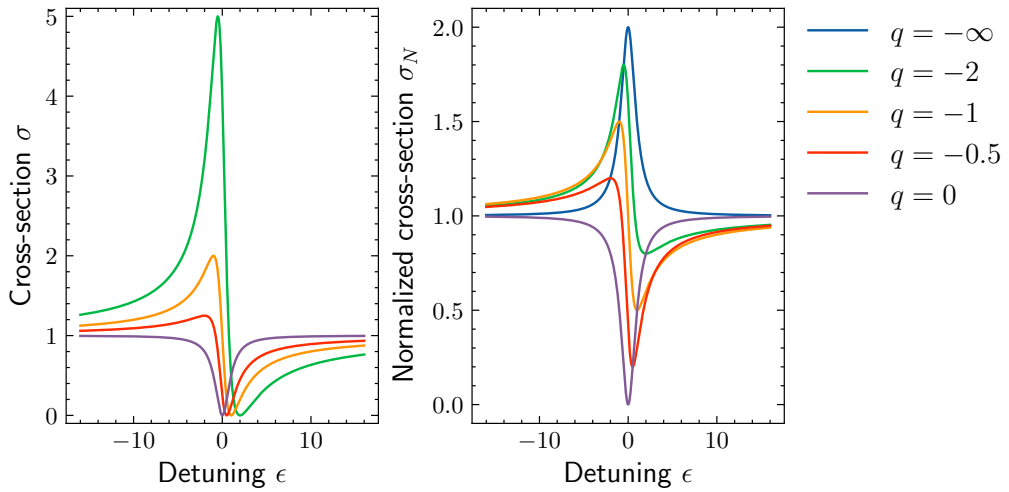

Figure 2.5.: Line shapes of autoionization resonances for different q-values. Note that on the left the curve for $q = -\infty$ is simply out of the plot window. On the right the resonant contribution as described in the text (eq.2.40) is normalized by a factor $(q^2 + 1)$.

interaction operator $\hat{\boldsymbol{V}}$, which leads to off-diagonal elements $V_E = \langle c_E|\hat{\boldsymbol{V}}|b\rangle$ in the Hamiltonian. This implies that by diagonalizing the coupled Hamiltonian we can obtain a new set of eigenstates, which can be represented as a linear combination of the uncoupled basis states. Finding the coefficients for this representation in the original basis is one of the main findings of Fano [96].

As a result, the bound state obtains an admixture of continuum states and thereby a finite lifetime $\tau \propto 1/\Gamma$; it becomes autoionizing due to the loss channel to the continuum. The new, autoionizing state $|a\rangle$ has a spectral linewidth $\Gamma = 2\pi|V_E|^2$, which we use to define the detuning from resonance $\epsilon = \frac{E-E_a}{\Gamma/2}$. In a spectroscopic context, a photon that excites the atom now has two pathways to the continuum: either the direct excitation to a continuum state $|c_E\rangle$ or through the autoionizing state $|a\rangle$. Because both paths are indistinguishable, they can be thought of as the two arms of a quantum interferometer, the configuration of which determines the absorption line shape. In terms of the asymmetry parameter

$$q = \frac{\langle a|\hat{\boldsymbol{d}}|g\rangle}{\pi V_E^* \langle c_E|\hat{\boldsymbol{d}}|g\rangle} = \frac{d_{ag}}{\pi V_E^* d_{cg}} \tag{2.39}$$

the absorption cross-section of the family of Fano profiles can be determined to be

$$\sigma \propto \frac{|q+\epsilon|^2}{1+\epsilon^2} = 1 + \frac{q^2 - 1 + 2q\epsilon}{1+\epsilon^2}. \tag{2.40}$$

Depending on the relative transition strength, the two paths can interfere constructive or deconstructive on either side of the resonance as is shown for different values of q in figure 2.5.

The line shape of the autoionizing state is formulated in terms of the background continuum absorption plus the resonance as can be seen from the last expansion in equation 2.40. The physical origins of the asymmetry of such line shapes can be understood from the parametrization of the q-parameter. Besides the strength of the configuration interaction V_E, the dipole matrix elements between the ground state and both the modified bound state and the pure continuum contribute. Without the configuration interaction or without the continuum $V_E = 0 = d_{cg}$, we recover a symmetric Lorentzian line shape as would be expected for any naturally decaying dipole. Another special case is the limit $q \longrightarrow 0$ (see figure 2.5): on resonance the atom becomes transparent, a scenario dubbed window resonance. The conclusion from these considerations is that an autoionizing state can be used as a quantum interferometer sensitive to the relative strength of the direct and indirect pathways to the continuum since the modification of any of the aforementioned quantities entails an observable change in the absorption line shape.

Numerical modeling

In light of the previous section, a particular convenient method to model a Fano line in a numerical few-level simulation is presented here. While the ground state and an excited bound state are naturally represented by discrete levels, the continuum is taken into account explicitly either through a large set of mutually overlapping resonances [60; 61] or a single, broad state as shown here:

$$\mathrm{i}\frac{\partial}{\partial t}\begin{pmatrix} c_g \\ c_e \\ c_c \end{pmatrix} = \begin{pmatrix} E_g & d_{ge}F_{XUV}(t) & d_{gc}F_{XUV}(t) \\ d_{ge}^{*}F_{XUV}(t) & E_e & V_{ci} \\ d_{gc}^{*}F_{XUV}(t) & V_{ci}^{*} & E_c - \mathrm{i}\,\Gamma_c/2 \end{pmatrix}\begin{pmatrix} c_g \\ c_e \\ c_c \end{pmatrix}. \tag{2.41}$$

The linewidth of the continuum Γ_c needs to be large enough to ensure an effective loss channel that surpresses unphysical continuum revivals. The model then takes into account the continuum and a single bound state, which can both be excited from the ground state via a XUV pulse and are coupled by the configuration interaction matrix element V_{ci}, which controls the linewidth of the autoionizing state. The desired asymmetry is tunable through the remaining transition matrix elements.

2.4. Transient absorption spectroscopy

The observables of interest in absorption spectroscopy are spectral intensities of light that previously interacted with some kind of target, possibly depending on various experimental control parameters. In order to relay these measured spectra to properties of the target, we need a concept of the measurement process. In our specific case, we are interested in the link between the absorption of a dilute gas and the microscopic dipole moment induced in the atoms and molecules that make up the target.

2.4.1. From microscopic to macroscopic

Because of the coherent excitation of all individual, non-interacting scatterers in a dilute target, we can restrict the description on the microscopic level to the treatment of a single quantum system obeying Schrödinger's equation. Thus, all relevant information of this particle are encoded in its wave function $|\psi\rangle$, although the density matrix formalism governed by the evolution of the von Neumann equation would be even more rigorous. The excitation through the radiation field generally leaves the quantum system in a superposition of states that form a wave packet which is non-stationary in time. This in turn leads to a non-vanishing dipole

$$\boldsymbol{d} = e\,\langle\psi|\hat{\boldsymbol{x}}|\psi\rangle\,, \tag{2.42}$$

that oscillates with frequencies corresponding to the energies of the excited states.

To derive the back-action of the atoms on the incoming field—the effect that ultimately leads to absorption—we connect the microscopic dipole to the propagation of electromagnetic waves via the macroscopic polarization:

$$\boldsymbol{P} = \varrho\,\boldsymbol{d}, \tag{2.43}$$

where ϱ is the density of the medium. From this point on, we take the wave equation 2.15 and simplify it using suitable approximations. First, we cast the fields into plane waves in z-direction, with envelopes $\mathcal{F}(t,\boldsymbol{r})$ and $\mathcal{P}(t,\boldsymbol{r})$ and since we deal with linearly polarized laser pulses and can assume the response of the target not to change the polarization, we also drop their vectorial character.

$$\begin{aligned}\boldsymbol{F}(t,\boldsymbol{r}) &\longrightarrow F(t,z) = \mathcal{F}(t,z)\mathrm{e}^{\mathrm{i}(kz-\omega t)},\\ \boldsymbol{P}(t,\boldsymbol{r}) &\longrightarrow P(t,z) = \mathcal{P}(t,z)\mathrm{e}^{\mathrm{i}(kz-\omega t)}.\end{aligned}$$

The time derivative in this simplified wave equation

$$\left(\frac{\partial^2}{\partial z^2} - \frac{1}{c^2}\frac{\partial^2}{\partial t^2}\right)\mathcal{F}(t,z)\mathrm{e}^{\mathrm{i}(kz-\omega t)} = \mu_0\frac{\partial^2}{\partial t^2}\mathcal{P}(t,z)\mathrm{e}^{\mathrm{i}(kz-\omega t)} \tag{2.44}$$

can be solved quite elegantly in the spectral domain by considering

$$\frac{\partial}{\partial t}\mathcal{F}(\omega) \propto \int \mathrm{d}t\,\mathrm{e}^{\mathrm{i}\omega t}\frac{\partial}{\partial t}\mathcal{F}(t) = \mathrm{i}\omega\int \mathrm{d}t\,\mathrm{e}^{\mathrm{i}\omega t}\mathcal{F}(t) = \mathrm{i}\omega\mathcal{F}(\omega). \tag{2.45}$$

Finally, the spatial derivative is performed in the *slowly varying envelope approximation*, which assumes the envelope $\mathcal{F}(z)$ to be weakly dependent on z such that $\partial^2/\partial z^2\ F(z)\to 0$:

$$\left(\cancel{\frac{\partial^2}{\partial z^2}} + 2\mathrm{i}k\frac{\partial}{\partial z} + \cancel{(\mathrm{i}k)^2 - \frac{(\mathrm{i}\omega)^2}{c^2}}\right)\mathcal{F}(\omega,z) = -\mu_0\omega^2\mathcal{P}(\omega,z) \tag{2.46}$$

Putting all this together with equation 2.43, we obtain the effect of the microscopic, induced dipoles on the macroscopic field

$$\frac{\partial}{\partial z}\mathcal{F}(\omega,z) = \mathrm{i}\frac{\varrho}{2\varepsilon_0 c}\omega\, d(\omega,z). \tag{2.47}$$

2.4.2. Optical densities

In order to access the atomic dipoles and their dynamics, we need an observable, which can be measured with a detector. Since only intensities are available to us and it is desirable to be independent of the incoming field, a suitable measure is the optical density (OD) defined as

$$\mathrm{OD} = -\log_{10}\left(\frac{I(\omega)}{I_0(\omega)}\right), \tag{2.48}$$

where $I(\omega)$ and $I_0(\omega)$ are the spectral intensities measured before and after the target. Linking the results above to the optical density, only takes a few more considerations. First we perform the integration assuming that the medium is homogeneous ($\varrho(z) = \varrho$, $d(\omega, z) = d(\omega)$)

$$\mathcal{F}(\omega, L) = \mathcal{F}(\omega, 0) + \mathrm{i}\frac{\omega}{2\varepsilon_0 c}\int_0^L \mathrm{d}z\, \varrho(z) d(\omega, z) = \mathcal{F}(\omega, 0) + \mathrm{i}\,\frac{\omega\varrho L}{2\varepsilon_0 c}\, d(\omega) = \mathcal{F}_{in} + \mathrm{i}\mathcal{F}_{gen} \tag{2.49}$$

which is valid as long as the generated field $\mathcal{F}_{gen}$ is small, i.e. the change of the incoming field $\mathcal{F}_{in}$ along the path propagation is negligible. We directly see that the generated field is phase shifted by $\pi/2$ and will interfere destructively with the incoming field. Second we calculate the intensity after the target. With the reasoning from above the term that corresponds to $|\mathcal{F}_{gen}|^2$ can be omitted.

$$I(\omega) = |\mathcal{F}(\omega)|^2 = |\mathcal{F}_{in}|^2 - \mathrm{i}\mathcal{F}_{in}\mathcal{F}^*_{gen} + \mathrm{i}\mathcal{F}^*_{in}\mathcal{F}_{gen} \tag{2.50}$$

Thus, the ratio of the outgoing and incoming intensities evaluates to

$$\frac{I(\omega)}{I_0(\omega)} = \frac{|\mathcal{F}_{in}|^2 - \mathrm{i}\mathcal{F}_{in}\mathcal{F}^*_{gen} + \mathrm{i}\mathcal{F}^*_{in}\mathcal{F}_{gen}}{|\mathcal{F}_{in}|^2} = 1 - \mathrm{i}\left(\frac{\mathcal{F}^*_{gen}}{\mathcal{F}^*_{in}} - \frac{\mathcal{F}_{gen}}{\mathcal{F}_{in}}\right) = 1 - 2\mathrm{Im}\left(\frac{\mathcal{F}_{gen}}{\mathcal{F}_{in}}\right). \tag{2.51}$$

To calculate the optical density, we approximate the logarithm by $\ln(1 - x) \approx -x$, which is valid since we required $\mathcal{F}_{gen} \ll \mathcal{F}_{in}$. The final result reads

$$\begin{aligned}\mathrm{OD}(\omega) &= -\log_{10}\left(\frac{I(\omega)}{I_0(\omega)}\right) = \frac{\varrho L}{\ln(10)}\frac{\omega}{\varepsilon_0 c}\,\mathrm{Im}\left(\frac{d(\omega)}{\mathcal{F}_{in}(\omega)}\right) \\ &= \frac{(\varrho L)_{\text{a.u.}}}{\ln(10)} 4\pi\alpha\omega\,\mathrm{Im}\left(\frac{d(\omega)}{\mathcal{F}_{in}(\omega)}\right),\end{aligned} \tag{2.52}$$

where the second line is the result in atomic units. This demonstrates that by measuring optical densities, we are directly susceptible to the imaginary part of the atomic dipole moment, without restrictions on the incoming field (which does not need to be in the weak field limit) and on the order of nonlinearities which generate the dipole. The main limiting factor being that the generated field has to remain weak compared to the incoming field, which can always be realized experimentally by lowering the path-length-density-product ϱL. We also see that from a time-domain perspective, we record the

whole dipole response in a time-integrated manner; temporal sampling of the dipole response is technically not possible. Therefore, the time resolution in ATAS measurement only depends on the time delay, while the 'real time' evolution is encoded in the spectrum, and both can be measured with arbitrary precision without violating any Fourier or Heisenberg uncertainty principle [34].

Differential optical density

Conceptually it is sometimes more meaningful and intuitive to have an optical density that reflects the changes induced through a perturbative/dressing field, which in our case are femtosecond NIR pulses. The formal way to do so, would be to measure absorption spectra with and without the NIR ($I_{ON}(\omega)$ and $I_{OFF}(\omega)$ respectively), plus references ($I_0(\omega)$) and computing the difference of the respective optical densities. Fortunately, as the following calculation shows, it is not necessary to record more spectra in this case, because the reference spectra drop out:

$$\begin{aligned}\Delta\mathrm{OD} &= \mathrm{OD}_{\mathrm{ON}} - \mathrm{OD}_{\mathrm{OFF}} = -\log_{10}\left(\frac{I_{\mathrm{ON}}(\omega)}{I_0(\omega)}\right) + \log_{10}\left(\frac{I_{\mathrm{OFF}}(\omega)}{I_0(\omega)}\right) \\ &= -\log_{10}\left(\frac{I_{\mathrm{ON}}(\omega)}{I_0(\omega)}\frac{I_0(\omega)}{I_{\mathrm{OFF}}(\omega)}\right) = -\log_{10}\left(\frac{I_{\mathrm{ON}}(\omega)}{I_{\mathrm{OFF}}(\omega)}\right).\end{aligned} \tag{2.53}$$

The resulting differential optical density, dubbed ΔOD, is particularly convenient for ATAS measurements of strong-field generated ions. Without the NIR pulses to induce strong-field ionization, there are no ions and hence no absorption other than of the neutral target. When the focus is on the ionic absorption, the ΔOD thus contains all the information of interest and even discards some background absorption from the neutrals. A further advantage is that the reference $I_{OFF}(\omega)$ is equivalent to shifting the NIR pulse in time to interact with the target long after the XUV pulse has passed. Experimentally this is easy to realize, since the time-delay is our main control parameter that is implemented by moving the a small mirror, which is extremely fast. Standard references are usually recorded by either moving the target cell out of the interaction region or turning off the gas, both of which are slower. Our new *in situ* reference method presented in section 3.2.3 circumvents this drawback, but requires longer integration times.

2.4.3. Beer-Lambert's law

While the above derivation of the optical density is valid for an arbitrary non-linear relationship between the incoming field and the generated dipoles, it can be further simplified in the weak-field limit, where the macroscopic polarization has a linear relationship with the electric field:

$$\mathcal{P}(\omega, z) = \varrho d(\omega, z) = \varepsilon_0 \chi(\omega)\mathcal{F}(\omega, z) \tag{2.54}$$

This way, we can integrate equation 2.46 directly:

$$\begin{aligned} &\frac{\partial}{\partial z}\mathcal{F}(\omega,z) = \mathrm{i}\frac{\omega}{2c}\chi(\omega)\mathcal{F}(\omega,z) \\ \longrightarrow\ &\mathcal{F}(\omega,z) = \mathcal{F}_{in}(\omega)\exp\left(\mathrm{i}\frac{\omega}{2c}\chi(\omega)z\right) \end{aligned} \tag{2.55}$$

Taking this result and calculating the intensity, we obtain the famous *Lambert-Beer law*:

$$\begin{aligned} I(\omega,z) &= \frac{1}{2}\varepsilon_0 c|\mathcal{F}(\omega,z)|^2 \\ &= I_0(\omega)\exp\left(-\frac{\omega\varrho}{\varepsilon_0 c}\,\mathrm{Im}\left(\frac{d(\omega)}{\mathcal{F}_{in}(\omega)}\right)z\right) \\ &= I_0(\omega)\exp(-\sigma\varrho z) \end{aligned} \tag{2.56}$$

From this result we obtain the very same equation for the optical density as above (equation 2.52), but with the restriction to weak fields. It is in this limit that common (XUV) absorption cross-section measurements are performed, as denoted in the last line. But in the case of a general ATAS experiment one has to be careful as to when it is appropriate to call the measured results proportional to a cross-section. As we have seen above, the lack of restrictions actually allows the access to much more (non-linear) processes.

2.4.4. Time-dependent dipole response

So far the goal of this section was to connect the microscopic properties of the target system to the observables. Equation 2.52 shows how measured optical densities relate to the Fourier transformation ($\mathcal{FT}$) of the time-dependent dipole of the system:

$$\mathrm{OD} \propto \omega\,\mathrm{Im}\left(\frac{d(\omega)}{F(\omega)}\right) = \omega\,\mathrm{Im}\left(\frac{\mathcal{FT}[d(t)]}{\mathcal{FT}[F(t)]}\right). \tag{2.57}$$

Now, the question arises, whether we can actually use the measurement to reconstruct the time-dependent dipole? The answer is yes, under the constraints that the XUV pulse $F(t)$ is sufficiently short in order to be described by a δ-function and that causality applies, meaning that there is no dipole emission prior to the excitation ($d(t < 0) = 0$). Under these conditions the solution was derived in [38] and [60] and holds even for the case where the dipole is explicitly time-dependent due to a perturbation $V(t)$ ($d(t) \longrightarrow d(t, V(t))$):

$$d(t) \propto \mathcal{FT}^{-1}[\mathrm{iOD}(\omega)]\,(t) = \frac{1}{\sqrt{2\pi}}\int \mathrm{iOD}(\omega)\,\mathrm{e}^{\mathrm{i}\omega t}\,\mathrm{d}\omega \quad \text{for } t > 0. \tag{2.58}$$

Thus, reconstruction of the temporal dipole from the measurement data is in principle feasible and will be used in chapter 6, as it provides intuitive insight into the real-time dynamics of the system. Other applications of the method are presented in [4; 98].

2.4.5. Dipole-control model

The dipole-control model (DCM) was developed in [37] and [59] in order to provide means for the interpretation of time-delay-dependent, spectroscopic datasets. Taking the time-dependent dipole moment of a quantum system as a starting point, it is used to analytically derive line shape functions, which in turn serve to fit the experimental data.

Considering an isolated quantum state $|e\rangle$, excited from the ground state $|g\rangle$ by an attosecond XUV pulse at time $t = 0$, we recall the result obtained in 1st order perturbation theory (see equation 2.38):

$$c_e(t) = \frac{1}{\mathrm{i}\hbar} F_0 \, d_{eg}. \tag{2.59}$$

Thus the full wave function of our model system is

$$|\psi(t)\rangle = |g\rangle + \frac{1}{\mathrm{i}\hbar} F_0 \, d_{eg} \, \mathrm{e}^{-\mathrm{i}\omega_{eg} t - \Gamma/2 \, t} \, |e\rangle \,, \tag{2.60}$$

where we have included a decay rate $\Gamma/2$ of the excited state. Evaluating the dipole moment of the system with this wave function and the relation $d_{eg} = d_{ge}^{*}$ yields

$$d(t) = \langle \psi | \hat{\boldsymbol{d}} | \psi \rangle = \frac{\mathrm{i}}{\hbar} F_0 |d_{eg}|^2 \, \mathrm{e}^{\mathrm{i}\omega_{eg} t - \Gamma/2 \, t} + \text{h.c.}, \tag{2.61}$$

where we discard the hermitian conjugate to simplify the analytical treatment, which is amounts to leaving unphysical negative frequencies out of the analysis. To compute an optical density, we need to determine the imaginary part of the dipole spectrum, divided by the incoming spectrum. Since our excitation pulse is a δ-function, the latter is constant with an amplitude F_0. Thus the essential part of the model, which we will call the line shape function $\tilde{d}(\omega)$, reduces to

$$\begin{gathered} \tilde{d}(\omega) = \mathrm{Im}\left(\frac{d(\omega)}{F(\omega)} \right) \propto \mathrm{Im}(\mathcal{FT}[f(t)]) \propto \mathrm{Im}\left(\int_0^\infty f(t) \, \mathrm{e}^{\mathrm{i}\omega t} \, \mathrm{d}t \right), \\ f(t) = \mathrm{i} \, \mathrm{e}^{\mathrm{i}\omega_{eg} t - \Gamma/2 \, t}. \end{gathered} \tag{2.62}$$

For this simple form of $f(t)$, i.e. the unperturbed decaying dipole, the line shape evaluates to

$$\tilde{d}(\omega) = \frac{\Gamma/2}{(\omega - \omega_{eg})^2 + \Gamma^2/4}, \tag{2.63}$$

the well-known Lorentzian line shape, which we previously encountered in discussion of the Fano formalism (section 2.3.2) for the case $q \longrightarrow 0$. Next, we turn to the more general case of a phase-shifted dipole and compute the resulting line shape function

$$\begin{aligned} f(t) &= \mathrm{i} \, \mathrm{e}^{\mathrm{i}\omega_{eg} t - \Gamma/2 \, t + \mathrm{i}\phi_0}, \\ \Longrightarrow \tilde{d}(\omega) &= \frac{(\omega - \omega_{eg}) \sin(\phi_0) + \Gamma/2 \cos(\phi_0)}{(\omega - \omega_{eg})^2 + \Gamma^2/4}. \end{aligned} \tag{2.64}$$

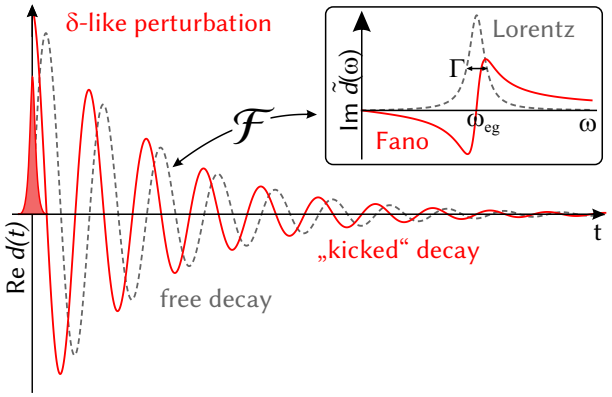

Figure 2.6.: Illustration of a free and a phase-kicked dipole (grey and red respectively). The inset shows the resulting Lorentzian/Fano line shapes. Graphic modified from [59].

We obtain an asymmetric resonance, similar to a Fano resonance (see figure 2.6). In fact, it was demonstrated in [99] that there is a direct relation between the phase-kick ϕ_0 and the Fano q-parameter

$$\phi_0 = 2\arg(q - \mathrm{i}) \leftrightarrow q = \cot\left(\phi_0/2\right), \tag{2.65}$$

which is plotted in figure 2.7. The major advantage of using equation 2.64 is in fitting quasi-Lorentzian line shapes with $\phi_0 \approx 0$. In this special case, it is hard to reach convergence with a Fano profile, because $q \longrightarrow \infty$ and the strong q-dependence of the amplitude parameter. So while strictly, we have not recovered the Fano-line shape, we have obtained a generalized Lorentzian line shape model, which accommodates an overall phase shift of the dipole response, which can be naturally present because of the interaction of a resonance state with a continuum or can be induced through a laser-driven Stark shift of the energy level during excitation [99].

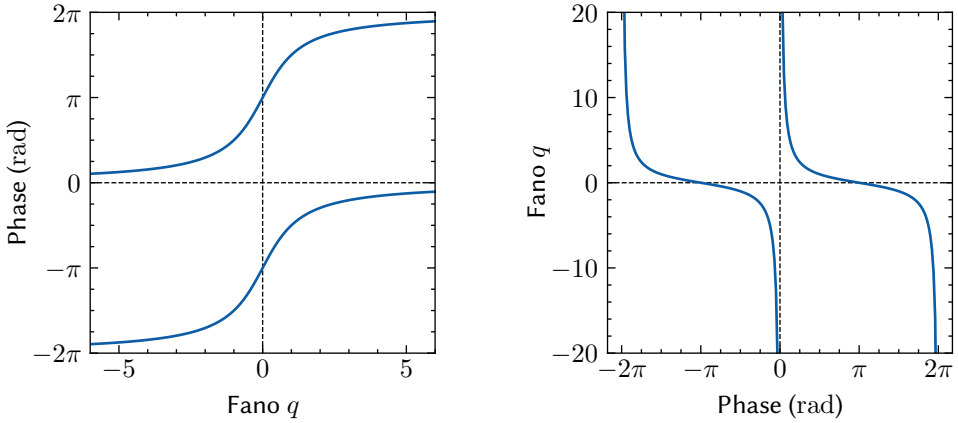

Figure 2.7.: Relationship between the instantaneous phase-kick ϕ_0 of the dipole moment in the DCM and the Fano asymmetry parameter q.

In the literature this model is also known as *oscillating dipole model* [57; 91]. For more than one transition, we can simply sum up their line shape functions (because of the linearity of the Fourier transform), which combining equation 2.52 and 2.64 amounts in its full form to:

$$\mathrm{OD}(\omega) = \frac{(\varrho L)_{\mathrm{a.u.}}}{\ln(10)} 4\pi\alpha\omega \sum_{\mathrm{T}} z_{\mathrm{T}} \frac{\Gamma_{\mathrm{T}}/2 \cos(\phi_{\mathrm{T}}) + (\omega - \omega_{\mathrm{T}}) \sin(\phi_{\mathrm{T}})}{(\omega - \omega_{\mathrm{T}})^2 + \Gamma_{\mathrm{T}}^2/4}, \tag{2.66}$$

where the z_T are a scaling parameter of the line strengths and α is the fine-structure constant.

It should be noted that this is only one possible variant of the DCM. Introducing a time-delay-dependent modification in the dipole response for example facilitates the *in situ* characterization of the dressing NIR pulses [73] and can be used to monitor the ultrafast buildup of a Rydberg series [4].

2.4.6. The xenon atom

The goal of this thesis is to explore possibilities to use strong-field generated ions as a target in attosecond transient absorption experiments. To this end, xenon was chosen for its low ionization potential of 12.13 eV (compared to the other rare gases, see table 4.1). The electronic configuration of xenon is $[\mathrm{Kr}]4d^{10}5s^25p^6$.

XUV cross-sections

While not suitable for measurements with femtosecond time resolution, synchrotrons, with their high photon flux and equipped with scanning monochromators, are of great importance in the measurement of XUV absorption cross-sections [100; 101], e.g. for the calculation of opacities of astrophysical objects [102]. Over the years neutral xenon and its ions have attracted attention as a benchmark system for machine science and theory [103–107]. Most of this interest in xenon is motivated through the study of the *giant dipole resonance*, which was discovered in 1964 [108] and is a phenomenon in the ionization through $4d \longrightarrow \epsilon f$ transitions. This prominent absorption feature (see figure 2.8) is a shape-resonance caused by the effective potential of the nf wave functions due to a strong centrifugal barrier in the $l = 3$ potential (for details see [109]). The collapse of the $4f$ wave function was studied extensively along the isonuclear series of Xe [110–114] and isoelectronic sequences that include xenon (e.g. I^-, Xe, Cs^+, Ba^{2+}, La^{3+}, Ce^{4+}) [101; 109].

In neutral xenon high-resolution measurements were performed on the discrete resonances of the $4d - np$ series above 65 eV [115; 116]. These resonances—high above the ionization threshold—are short lived with a lifetime of $\Gamma = 6$ fs after which they undergo Auger decay. They have been analyzed in terms of the Fano formalism and were found to be quasi-Lorentzian with $q \approx 200$. A time-resolved study of these resonances was performed within our group and first reported in [59]. A collaborative study that focuses on the theory of core-hole excited states has recently been published [7].

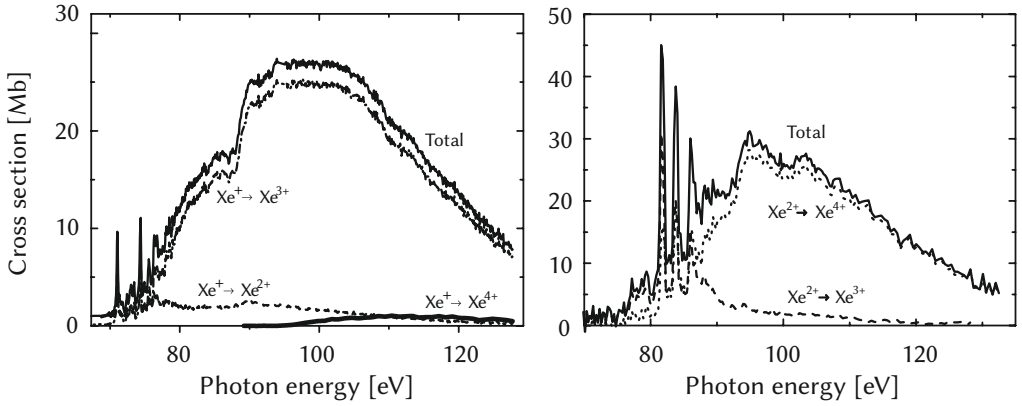

Figure 2.8.: Experimental absolute photoionization cross sections of Xe^+ (left) and Xe^{2+} (right). The broad, continuous absorption feature is the *giant dipole resonance*. The increase in the strengh and number of discrete resonances in Xe^{2+} is due to the increasing collapse of the $4f$-wave function for higher charge states. Figures adapted from [110].

The focus of this work lies in the investigation of the time-dependent buildup of resonances in strong-field ionized xenon. The transition of interest in Xe^+ belong to the $4d^{10}5s^25p^5 \longrightarrow 4d^95s^25p^6$ or short $5p^{-1} \longrightarrow 4d^{-1}$ series, while in Xe^{2+} the strongest lines of the $5p^{-2} \longrightarrow 4d^{-1}5p^{-1}$ series are observed. Both sets of transition lines have been measured in [110] and their experimental cross-sections are plotted in figure 2.9.

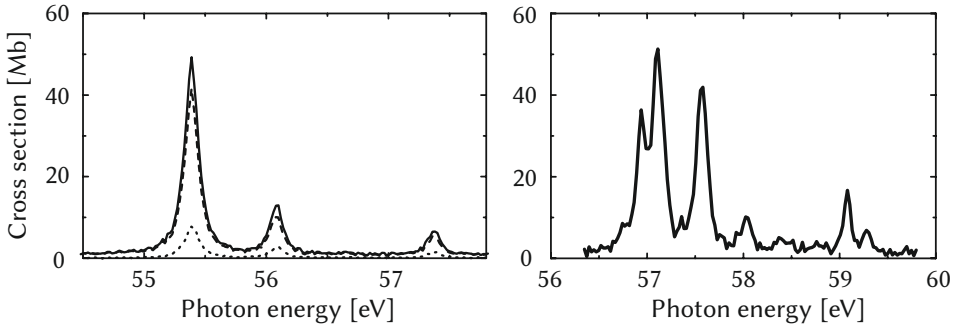

Figure 2.9.: Experimental absolute photoionization cross sections for the $4d \longrightarrow 5p$ resonance region in Xe^+ (left) and $Xe^{2+} \longrightarrow Xe^{3+}$ (right). Single ionization cross section (dashed curve), double ionization (dotted curve), sum of single- and double-ionization cross section (solid curve). Figures adapted from [110].

ATAS in xenon

In neutral xenon, the autoionizing states of the $5s - np$ series around 22 eV [117; 118] and the inner-shell excitations of the $4d - np$ series (> 65 eV) [119–121] have been studied extensively using ATAS. The first transient absorption experiments on xenon ions

were performed by Loh et al. [39] and investigated the ion state populations after SFI. References of more recent experiments are given within suitable context in chapters 4 to 6.

2.5. Electron spectroscopy

While we focus mostly on the transmitted photons to probe electron dynamics, a complementary approach aims to directly record the electrons themselves. This obviously requires an ionization event to eject an electron from the parent system, which can subsequently be detected by a microchannel plate (MCP). The field of electron spectroscopy as a whole is too wide and sublime to only scratch its surface in a general manner. Thus the scope of this section will be narrowly focused on the methods instrumental to this thesis. The technique of attosecond streaking spectroscopy—short streaking—is introduced, because the efforts undertaken within the scope of this thesis to combine it with absorption spectroscopy are presented in section 3.3. Furthermore, the reconstruction of attosecond beating by interference of two-photon transitions (RABBITT) is briefly mentioned as a technique that was very successful in the measurement of attosecond delays in photoionization over the course of the last decade. Both of these schemes were originally designed to characterize attosecond pulses or pulse trains, respectively.

The fundamental principle of both methods is the same: an XUV pulse (train) ionizes a sample and these free electrons are subjected to a time-delayed dressing pulse. Finally, the emitted electrons are collected by a time-of-flight detector and their kinetic energy spectrum is analysed as a function of time-delay. The exact shape of the XUV and dressing pulses marks the crucial difference between streaking and RABBITT as it entails different scopes of applications for which they are suited best.

2.5.1. Streaking

In attosecond streaking an isolated attosecond pulse (IAP) is used to ionize the target gas. The kinetic energy spectrum of the ejected electrons is essentially a copy if the IAP's spectrum subtracted by the ionization potential that had to be overcome to liberate the electrons. Once free, the electron probes the femtosecond laser pulse that is time-delayed with respect to the IAP and experiences the remainder of the passing electric field. As a consequence of classical electrodynamics this electric field exerts a force on the electron and imprints a shift onto the electrons momentum, which is proportional to the field's vector potential $A(\tau)$ at the delay that corresponds to the time of the ionization τ:

$$\Delta p(\tau) = e \int_{\tau}^{\infty} F(t)\mathrm{d}t = eA(\tau). \tag{2.67}$$

The electrons are said to be streaked by the laser field, which, via the relation $F(t) = \frac{\mathrm{d}}{\mathrm{d}t}A(t)$, is imprinted directly onto the electron spectra. By scanning the time delay, the complete streaking field can be sampled and reconstructed.

The electrons that fly along the polarization axis of the linearly polarized pulses are analyzed by a time-of-flight (TOF) spectrometer. In its most simple implementation such a spectrometer consists of a drift tube and a MCP detector as illustrated in figure 2.10. Often the drift tube is manufactured out of μ-metal with high permeability, to shield the electrons from stray magnetic fields that could influence their time-of-flight. Additional, potential features include retardation electrodes and electron optics to steer and manipulate the electrons to optimize the detection. It is standard procedure to capture only the electrons that are emitted within a small solid angle around the laser's axis of polarization to avoid smearing of the time-of-flight across different trajectories to the detector and to exclude effects contributed from angular variations in the photoemission.

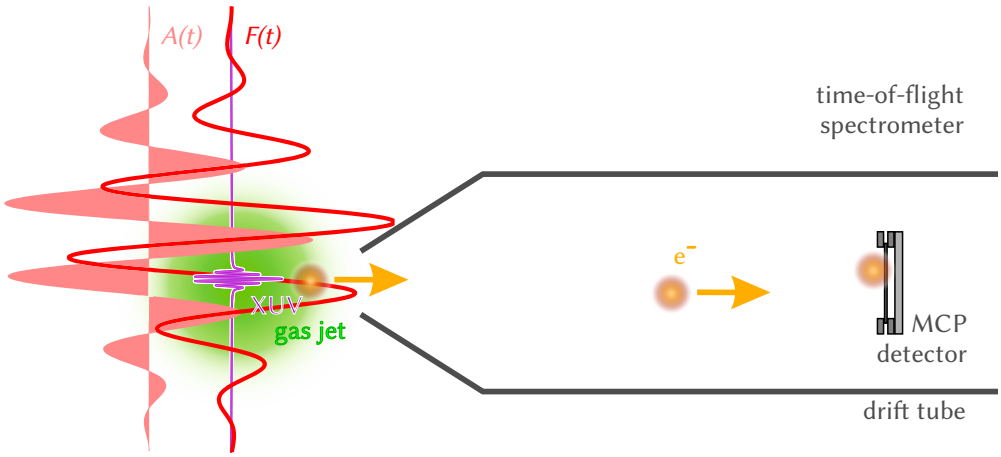

Figure 2.10.: Illustration of the measurement scheme of attosecond streaking. An XUV attosecond pulse ionizes electrons (yellow) from a gas target (green). A time-delayed pulse (red) imprints a shift onto the electrons' kinetic energy, which is analyzed by means of a time-of-flight-spectrometer. The latter consists of a drift tube and an MCP detector.

By tracking the shift of the electron spectra it is straightforward to characterize the streaking field with sub-fs resolution [122]. A much stronger incentive to implement a streaking setup, is its potential to characterize the XUV pulses that trigger the ionization as well. Through the ionization, the chirp of the XUV pulse is mapped onto a time-momentum distribution of the electrons, because the release times become energy-dependent and the initial momentum distribution probes the streaking field at different times. As a result, the recorded electron spectra are tomographic projections of this momentum distribution [32] and can be used to retrieve the chirp from a suitable set of spectra acquired at different time-delay positions. Different algorithms have been developed for this purpose [123–126]. We have implemented and tested such an algorithm [3] based on ptychographic phase reconstruction [127]. Streaking is typically used to reconstruct the shortest XUV pulses generated by state-of-the-art lasers and beamlines [128–130], where the current records are FWHM durations of (53 ± 6) as [63] and (43 ± 1) as [64].

2.5.2. Attosecond delays

When electrons are ionized from different subshells, several replicas of the IAP spectrum weighted by the respective bound-continuum dipole matrix elements appear in the electron spectrum. This can be used to track ionization delays between the subshells by extracting the shift between the respective streaking traces [131–133]. The development of RABBITT went along the same lines. Devised as a technique for the temporal characterization of attosecond pulse trains (APTs) [31], it evolved to a powerful method to measure photoemission time delays [134–137] i.a. in He [138], Ne [139] and Xe [140; 141].

The key takeaways from this excursion are twofold. First, XUV pulse characterization techniques exist and are vital to probe ultrafast dynamics. It is therefore unsurprising that we want to incorporate these features in our setup as will be presented in section 3.3. Second, the observation that a technique developed for one (primitive) purpose can evolve to be used at the spearpoint of fundamental research. This is the motivation to strive for a XUV pulse characterization method in a ATAS configuration to be addressed in chapter 5.

3. Experimental setup

Doing research at some point always amounts to innovating an existing topic and creating something new. As this is the account of experimental efforts to investigate the dynamics of strong-field generated ions, the tools for this research are presented in this chapter. These encompass a state-of-the-art laser system, optics for the manipulation and characterization of the ultrashort laser pulses and finally the vacuum beamline for attosecond transient absorption spectroscopy. As science demands and progresses, this setup has never been finalized to complete routine tasks, but is subject to continuous upgrades and fixing. After all, if it were easy to perform any given measurement, someone else would have performed it already! A coarse sketch of the overall setup and the changes introduced within the course of this thesis are presented here. Part of this is our ongoing effort to combine ATAS with electron streaking spectroscopy, which is recounted at the end of this chapter. A review of our experimental beamline and methods, including the newly developed *in situ* reference technique, have been published in [2] for detailed reference.

3.1. The laser system

Our experiments require ultrashort and strong laser pulses. The first step in their generation is the commercial laser system FEMTOPOWER^{TM} HE/HR CEP4 from the company Femtolasers[1]. This system consists of a laser oscillator and an amplifier and can deliver 20 fs pulses with 3 mJ pulse energy at a repetition rate of 3 kHz at a central wavelength of 790 nm in the near-infrared (NIR) spectral region. Both, oscillator and amplifier use titanium-doped sapphire (Ti:Sa) as gain medium, which is a standard technology for the production of ultrashort laser pulses.

The Rainbow oscillator is a dispersion-managed[2], Kerr-lens mode-locked laser [20; 21], which is internally pumped by a Spectra Physics Millenia diode-pumped solid-state (DPSS) pump laser with 3.5 W continuous power at 532 nm. It outputs pulses with 3.5 nJ pulse energy at a repetition rate of 75 MHz that are almost octave-spanning and have < 10 fs duration. Before these pulses are used to seed the amplifier, their carrier-envelope phase (CEP) is measured in the adjacent CEP4 module by means of an $f-2f$ interferometer, which uses a periodically poled lithium niobate (PPLN) crystal for SHG. To stabilize the CEP, the pulses subsequently pass an acousto-optic frequency shifter (AOFS), which can shift the hitherto fluctuating CEP from the pulse train, leading to a stable output [142]. This feed-forward scheme can be used to fix the CEP to any desired value and makes the entire setup passively CEP-stable. The AOFS that is currently installed, is not

[1] Bought by Spectra-Physics, bought by MKS and eventually partially discontinued.
[2] That is to say, it actively stabilizes the optical path-length of the cavity.

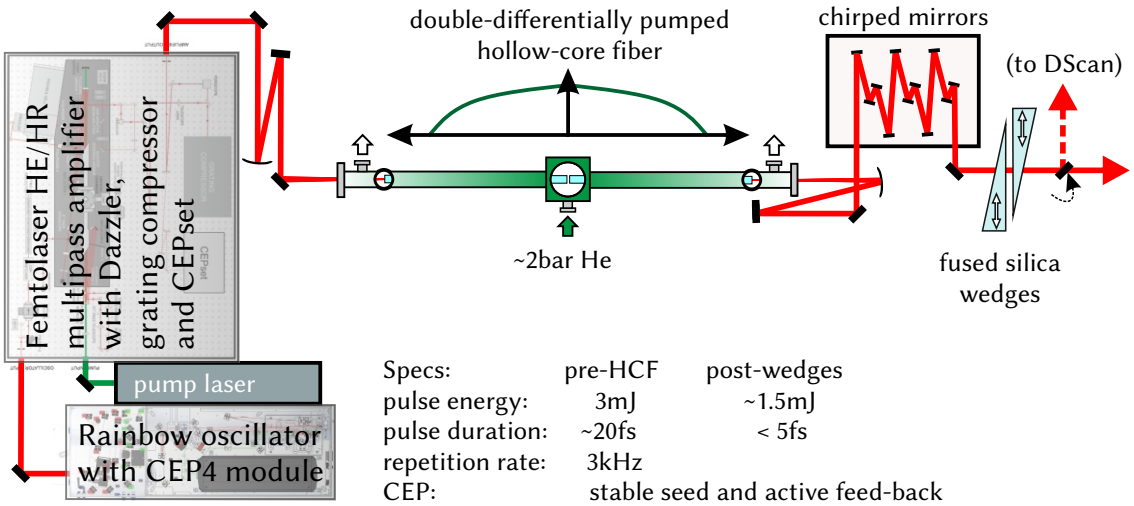

Figure 3.1.: Schematic of the essential elements of the laser system, followed by components that are used to compress the pulses temporally.

the first of its kind. The original piece did not reach enough power in the diffraction order that is used as a seed to the amplifier anymore and had to be replaced after extensive tests of the electronics. Due to imperfect coupling to the cooling system, the new crystal shows a drop in power, when the radio signal that produces the acoustic wave is turned on. This warm-up time until the transmitted power has stabilized has to be taken into account, when the system is switched on. For the case that the passive CEP stability that is achieved through the CEP4 module is unwanted, the system can be outsmarted, by providing a fake feed-back to the AOFS. Instead of the actually measured CEP from the $f - 2f$ interferometer, a constant frequency from a function generator can be supplied to the AOFS. Thus, the AOFS shifts all pulses in the same manner, which effectively leaves the CEP free-running, without having to introduce any changes to the optical beam path.

The weak oscillator pulses are thereafter used to seed the amplifier, which is based on the chirped-pulse amplification (CPA) [22] technology. After the pulses are stretched to the picosecond regime through dispersion in fused silica slabs, they are amplified in a 10-pass amplifier, which is pumped by an external, Q-switched DPSS pump laser (DM-50 Photonics Industries), which delivers nanosecond pulses at 50 W average power. The amplifier gain crystal is cryogenically cooled, which reduces thermal lensing in the crystal and together with the stretching of the seed pulses reduces the strain on the crystal to prevent its destruction during operation. To allow cooling without condensation (icing) onto the crystal, it is enclosed in a vacuum chamber operating at maximum at 10^{-5} mbar. Not all seed pulses are amplified all the way through the system. After 4 passes through the gain medium, the beam is directed through a Pockel's cell, which selects every 25000^{th} pulse. These are amplitude- and phase shaped by an acousto-optic

programmable filter called Dazzler (Fastlite). The Dazzler is used to reduce the gain-narrowing in the amplification process and to tailor the spectral phase of the pulses to some extent. As nicely illustrated by Silva et al. [143], iterative optimization of the Dazzler settings can help to compress the pulses. The last stage of the amplifier is the recompression of the amplified pulses with a grating compressor and chirped mirrors for the TOD. The output of the laser system is thereafter focused into a hollow-core fiber (HCF). Two sets of beam-align diagnostics with position sensitive diodes and motorized mirrors stabilize the pointing of the beam; one for the seed in front of the amplifier and another at the output of the amplifier to the entrance of the fiber. A very general setup of the laser system and the subsequent optics is shown in figure 3.1.

3.1.1. Pulse propagation

According to the Fourier relation between the time and frequency domain, the 20 fs pulses from the laser need to be spectrally broadened to reach shorter pulse durations. The standard solution to this problem is the use of a gas filled hollow-core fiber and the subsequent compression of the pulses in a chirped mirror compressor.

Double differentially pumped hollow-core fiber

The first use of self-phase modulation in gas-filled hollow-core fibers was reported in [144; 145]. The long established approach is to use a long glass capillary as an high-intensity beam guide, but newer developments also employ stretched, flexible telecommunication fibers [146]. Over time, the HCF in our setup was continually upgraded to meet the needs of the laser and the experiments. With the previous 1 mJ laser system, a static, neon-filled fiber was sufficient. Due to the higher pulse energy of the system presented here, the new laser was equipped with a differentially pumped HCF. Filling the fiber from the rear, while at the same time continuously pumping the front, helps to reduce plasma generation at the incoupling focus. These plasma effects are detrimental to the beam mode as well as to the fiber surface. The Femtolasers Kaleidoscope system consisting of this HCF and a specially designed chirped mirror compressor was for example used by Trabattoni et al. [147]. However, even such a system still suffers under plasma degradation at the rear, which lead us to design our own double differentially pumped hollow-core fiber. This fiber was inspired by work at the MPQ in Munich [148] and is operated with helium. It is schematically depicted in figure 3.1. A pressure scan, demonstrating, which FTL pulse durations can in principle be reached with this system is shown in figure 3.2. The capillary used as a fiber is 1.5 m long and has a hole diameter of 310 µm. The tricky part in the installation is that it needs to be broken in the middle in order to let the gas enter the central channel and then both sides need to be sealed off to allow the pumping of the exits. It was found that the best glue for sealing is the vacuum epoxy Torr Seal, in contrast with other two-component glues that are more difficult to handle when replacing an old fiber. To ensure proper operation of the fiber

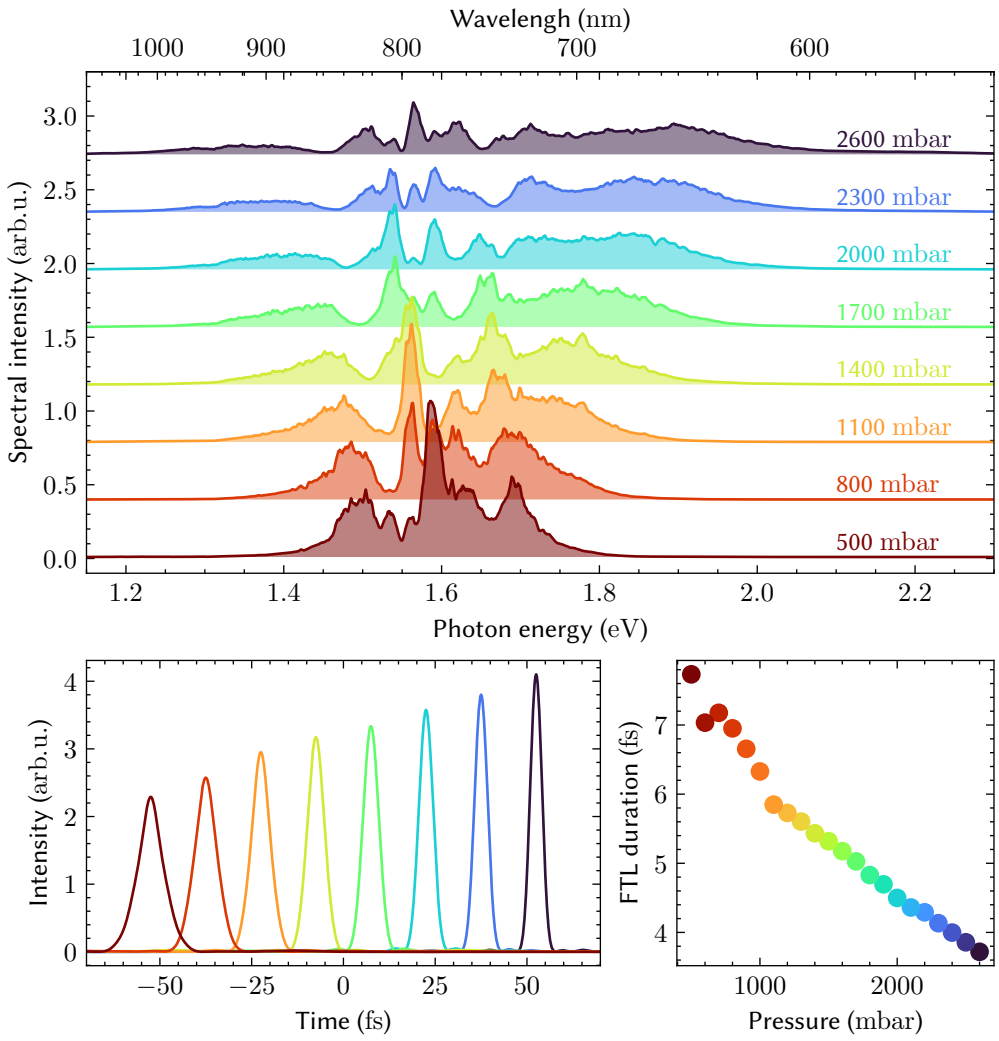

Figure 3.2.: Hollow-core fiber pressure-scan. (top) Spectra recorded for different helium input pressures. (bottom) Assuming a flat spectral phase yields the pulses on the left. On the right, the extracted FWHM duration of the Fourier transform limited pulses is shown as a function of helium pressure. Data from [61]. For the conversion of the spectra from the wavelength to the energy scale, the reader is referred to appendix A.2.

after it is broken it is further necessary to monitor the installation process by shining the attenuated laser through the HCF both before and during the sealing. This is crucial, since fibers that were installed by simply aligning the broken parts by eye did not last long under continuous operation. By optimizing and measuring the transmitted power through the intact fiber, one can obtain a good orientation as to what should be feasible after cutting the fiber in half. Additionally it can be advised that too much turning and rubbing both parts of the fiber is also detrimental to the coupling of the halves and can decrease the maximum available power. Monitoring the power during the whole sealing process was the crucial step to successfully commissioning this fiber. Optionally, a beam profiler can be used to check the spatial mode of the beam before and after the fiber is broken. With this procedure 60% transmission (5.4 W) through the fiber and a stable beam mode unhampered by plasma-induced fluctuations were achieved.

The latest development in the HCF sector is the control of the pressure gradients in the fiber [23]. With our pump, we achieve < 10 mbar at both ends of the fiber. Being able to independently set the pressure at both sides would be an additional control parameter to tune the spectral broadening and could constitute the next step in the improvement of our setup.

Pulse compression

Spectral broadening in the hollow-core fiber alone does not make the pulses shorter. Due to dispersion in the conversion medium and the SPM process itself, they are chirped and need to be compressed again. To achieve this, we employ a chirped mirror compressor which consists of either five or seven pairs of double-angle chirped mirrors (PC70, Ultrafast Innovations), which introduce negative GDD of $-40\,\mathrm{fs}^2$ per pair. To fine-tune the dispersion of the whole beam path, a pair of motorized glass wedges can be moved in and out of the beam to introduce more or less glass on the path of the pulses. This way, we can achieve pulses as short as 4.2 fs. Further compression is limited by higher order chirp. It is typically for setups like ours to produce pulses with negative TOD, which manifests as a pre-pulse (compare figure 2.1). To introduce more TOD, part of the fused silica from the wedges can be replaced by a material that has a higher TOD/GDD ratio than the glass. Materials that meet this requirement are e.g. water, ammonium dihydrogen phosphate (ADP) and potassium dihydrogen phosphate (KDP) [149]. Near perfect compression in this way has been demonstrated both with water [150] and ADP [151]. With the ADP crystals we bought, we can indeed achieve < 4 fs pulse durations and high contrast pulses by replacing 1 mm fused silica by ADP. Unfortunately the surface flatness of the commercially available crystals is only $\lambda/2$. The wave-front distortions caused by the transmission through the crystal therefore deteriorate the focus of the beam such that there is no net gain, only experimental complications through the use of the crystal.

3.1.2. Pulse characterization

The key challenge in the characterization of short laser pulses is that ideally one would use an even shorter event to sample the pulse directly in the time domain. In the case of fs-laser pulses, such a phenomenon would have to feature attosecond duration and is usually either not at hand, or too laborious to use just for characterization purposes. Therefore, most techniques developed over the last three decades rely on self-referencing schemes and encode the time-dependence through the use of a non-linear, optical process. On this route, the central goal is the retrieval of the spectral phase that cannot be measured through linear optics alone[3] and the subsequent calculation of the temporal field via Fourier transformation (see eq.equation 2.2). Therefore, the common principle of established techniques [152–154] is the acquisition of spectra from a non-linear process as a function of control parameter that encodes the spectral phase in a 2D map[4]. The phase is then reconstructed from the measurement data via iterative algorithms[157; 158].

In the dispersion scan or short D-Scan [159; 160] the pulses are manipulated as the name says through the controled variation of the dispersion that the pulses experience, which is realized through the addition of glass in the beam path. Since the dispersion management of the total beam path includes a pair of glass wedges for fine-tuning of the pulse duration anyways, this approach requires no additional optics. Recording spectra of some non-linear process (SHG [161], THG [162], XPW [163; 164]) or self-diffraction [165] as a function of the glass insertion z, yields a 2D trace $S(\omega, z)$. To invert this trace, different kinds of algorithms have been tested [166], such as Nelder-Mead [150], generalized-projections [167] and evolutionary algorithms [168]. Even deep neural networks (DNNs) [169] have successfully been applied to this fitting challenge. For more than octave-spanning spectra, the D-Scan can simultaneously retrieve the CEP[170]. In this work the SHG D-Scan set up in my Master's thesis[171] is used with a recently improved phase retrieval based on a conjugate gradient descent algorithm (Labview2013).

The calculation of a theoretical D-Scan trace requires an independent measurement of the pulses' fundamental spectrum $|F(\omega')|^2$:

$$S(\omega, z) \propto \left| \int_{-\infty}^{\infty} \left(\int_{-\infty}^{\infty} F(\omega') e^{izk(\omega')} e^{i\omega' t} \mathrm{d}\omega' \right)^2 e^{-i\omega t} \mathrm{d}t \right|^2 . \tag{3.1}$$

The retrieval now works by iteratively adapting the spectral phase until the experimental trace is reproduced sufficiently well. An example of the experimental trace and the subsequent phase retrieval is shown in figure 3.3. From a fit to the retrieved spectral

[3] Since the optical observables are intensities $|S(\omega, t)|^2 = \mathcal{S}^2$, not fields $S = \mathcal{S}e^{i\varphi}$, any phase φ drops out.

[4] Note that one-dimensional methods such as the intensity autocorrelation or interferometric autocorrelation are either ambiguous [155] or not sufficiently characterized [156] to retrieve the correct spectral phase with certainty.

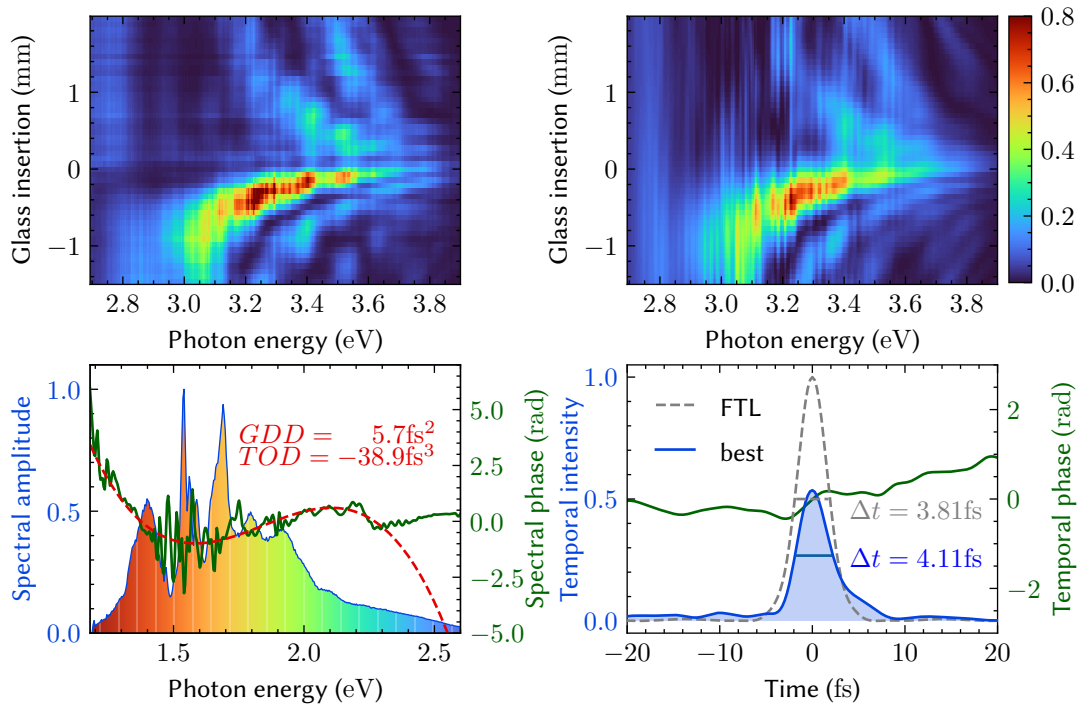

Figure 3.3.: Example of a D-Scan characterization measurement. (top) Recording the SHG spectrum as a function of the wedge insertion yields the experimental trace (left). By varying the spectral phase, the trace is fitted to the measurement, which yields the retrieved trace (right). (bottom) The measured fundamental spectrum is shown together with the retrieved spectral phase (left). The pulse in the time domain (right) is obtained via Fourier transformation.

phase, the uncompensated higher-order dispersion on the pulse can be extracted. The dominant contribution stems from uncompensated third-order dispersion as discussed above. It should be noted that the peak intensity of the retrieved pulse is only about half that of the transform-limited pulse, even though its duration ΔT_{FWHM} is only $\approx 8\%$ longer, since this affects the intensity calibration as well (see section 4.3.3).

3.1.3. Beam characterization

For the generation of high-harmonics and to optimize the on-target NIR intensities, the spatial characterization of the beam foci is indispensable. For the NIR beam, the characterization is straightforward, by measuring the beam profile with a CMOS camera. Moving the camera along the focus (e.g. on a translation stage) the beam profile is monitored and its evolution can be analyzed systematically to extract waists, astigmatism and Rayleigh range of the beam as has been nicely presented in [172]. Typical values for the beam waist in our setup range between $2W_0 = 77–130\,\mu m$, which corresponds to FWHMs of $45–80\,\mu m$.

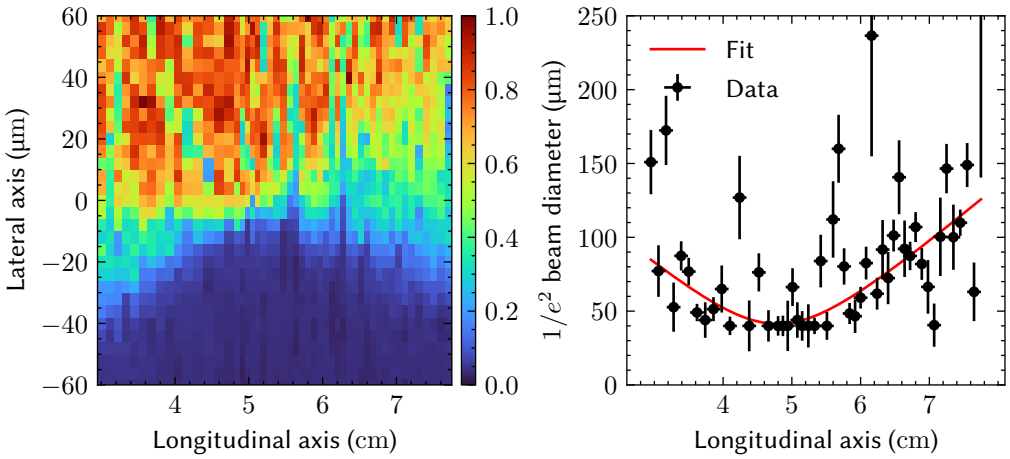

Figure 3.4.: Results (left) and analysis (right) of a knife-edge scan. The data is obtained by scanning a razor blade through the beam and recording the integrated intensity in the far-field. In the analysis, each lateral scan is fitted by an error function. Their widths are extracted and plotted on the right to be fitted by a Gaussian beam waist function. Data from [172].

For the XUV beam, the situation is a bit trickier. Although cameras and other position sensitive detectors exist for this spectral range, they are costly and the whole setup needs to be operated under vacuum conditions, because the absorption length of an XUV photon at ambient pressures is on the order of tens of micrometers [173]. By making use of the XUV spectrometer that will be introduced in more detail below, we have reimplemented an alternative method to measure some properties of the XUV beam. In the so-called knife-edge scan, the integrated intensity of the beam is measured after blocking it partially with a straight edge. In our implementation, we glued a razor blade to one of our target cells and scanned the cell position laterally and longitudinally along the focus. The results and analysis of such a scan are presented in figure 3.4. For each longitudinal position, the blade blocks the XUV light according to its overlap with the beam. In the focus the beam is smallest and thus the change in recorded intensity occurs over a small range of lateral translation steps. By fitting error functions to each of these lineouts a Gaussian width can be extracted for each position and can be used to extract the minimal beam waist and Rayleigh range along one spatial axis of the beam. In the measurement presented here, we obtain $2W_0 = (41 \pm 5)\,\mu\text{m}$ for the $1/e^2$ diameter and $z_R = (1.0 \pm 0.2)\,\text{cm}$ for the Rayleigh range of the beam, which shows that the XUV beam only probes a fraction of the NIR focus.

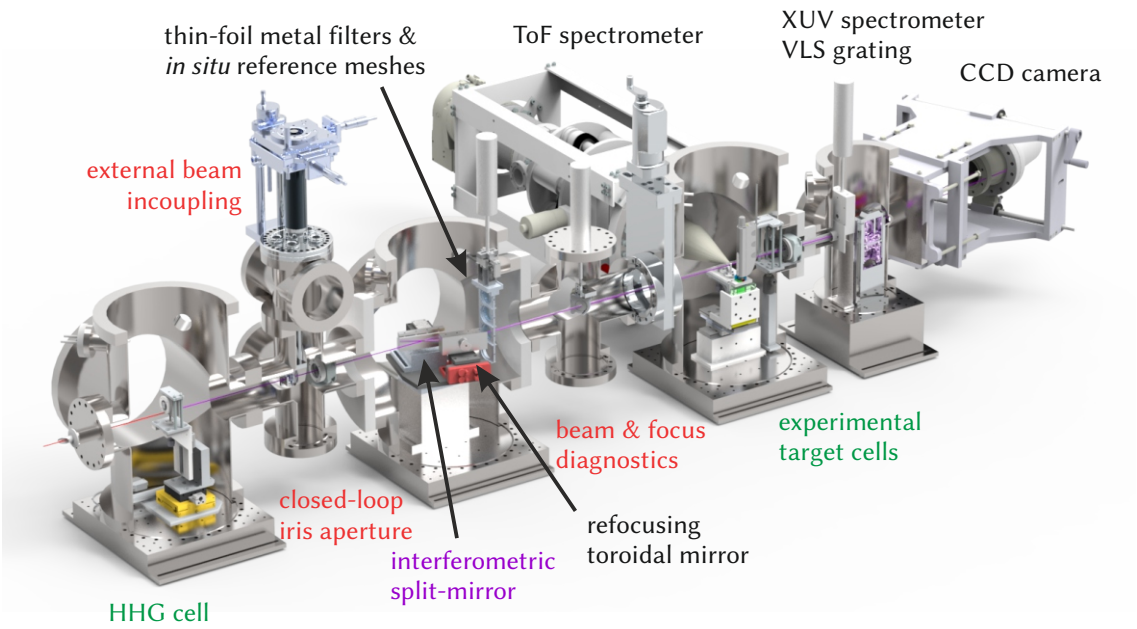

Figure 3.5.: CAD drawing of a cut through the vacuum beamline. Adapted from [2].

3.2. Experimental setup for attosecond absorption spectroscopy

As hinted at above, the main experiment has to be conducted under vacuum conditions, because XUV radiation with photon energies of tens of electronvolts easily ionizes any atoms and molecules and would therefore be absorbed within < 1 mm. A detailed review of our vacuum beamline is given in Stooß et al. [2]. Here, the features that are important for this thesis or those that I have contributed to are presented.

To get an impression of the beamline, a CAD model is depicted in figure 3.5, while the schematic in figure 3.6 helps to illustrate the function of the individual parts. The setup consists of three main chambers and a home-built flat-field XUV spectrometer. Roughly speaking, the XUV light is produced in the first, the manipulation of the pulses takes place in the second and the experiment is conducted in the third chamber. Last but not least, the XUV spectra are recorded. Missing from the sketches are the vacuum lines and pumps, most notably the two large 2050 L/s turbo molecular pumps (TMPs), (HiPace 2300, Pfeiffer Vacuum) above HHG and target cells, which serve to dispose of the gas load, while maintaining chamber pressures of $\approx 10^{-3}$ mbar. In the following the different sections of the beamline will be discussed individually.

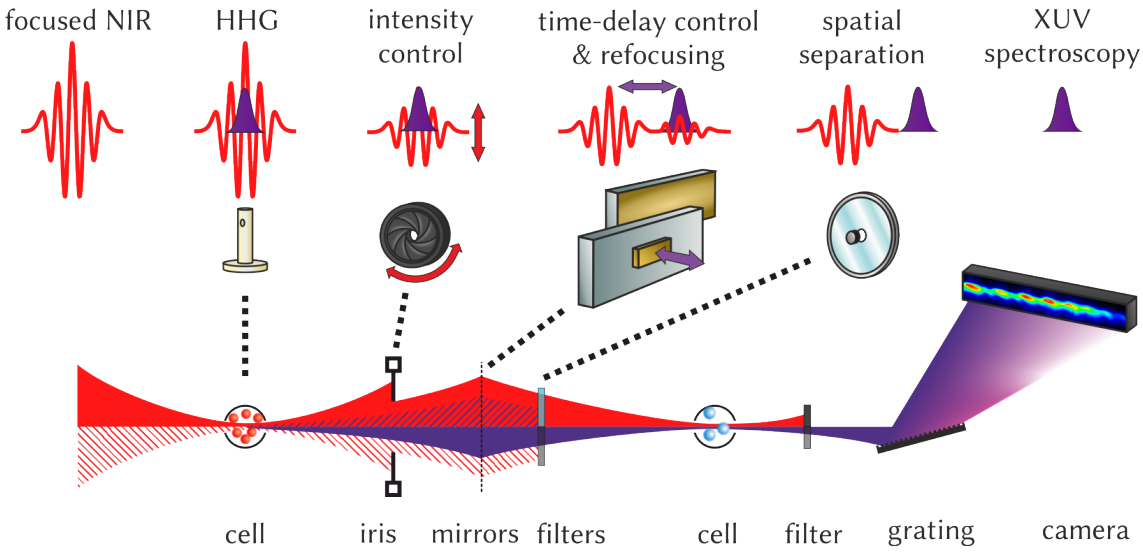

Figure 3.6.: Schematic beam path and pulse configurations along with sketches of the essential components in the vacuum beamline. The upper and lower halves of the beam path focus either primarily on path of the NIR or XUV beam, respectively.

3.2.1. High-harmonic generation

The first stage in the experiments is the generation of attosecond pulses in the first vacuum chamber via high-harmonic generation (HHG) (see section 2.2.3). From the outside of the chamber, the NIR laser pulses are focused into a gas cell at the center of the chamber. By adjusting the focal length and the beam diameter, the spot size and divergence can be tuned to obtain the best conversion efficiency for the desired HHG gas. Within this thesis, neon (at pressures of $\approx$ 110 mbar) was used almost exclusively as the HHG target, because of an interplay between the amount of ionization through the NIR pulses in the HHG gas and the focus quality in the target chamber. To reach high NIR intensities on target, the distortion of the beam can be minimized by choosing a HHG gas with high ionization potential, which gave neon the preference over e.g. argon. An example of a typical HHG spectrum is shown in figure 3.7, while a cell is depicted in figure 3.10. These cells are manufactured from the glass-ceramic Macor and feature a 3 mm long and 150 µm wide channel, through which the laser is focused. For alignment and phase matching optimization, the cell can be translated both longitudinally and laterally to the beam. In the standard configuration, the laser beam and the newly generated XUV beam co-propagate and are both used in our two-color experiments.

To achieve the generation of an isolated attosecond pulse (IAP), the emission of harmonic light has to be restricted to a single half-cycle of the driving field. This can be achieved by compressing the driver pulse to the single-cycle regime or by imposing a gating method on the XUV emission. An overview over a variety of gating mechanisms is given in [126]. Without taking any special measures, the scheme that we use is called

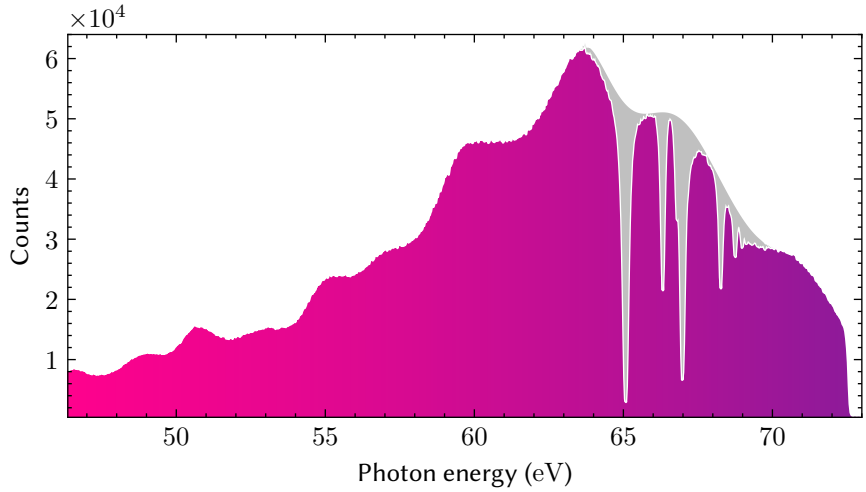

Figure 3.7.: Example HHG spectrum produced with a 4.5 fs pulse in neon. The neutral xenon absorption lines at photon energies > 65 eV are present, because no references without gas target were recorded. The gray filling illustrates how a reference spectrum can be obtained by means of low-pass filtering. Due to the short driving pulse duration, the spectrum is quasi-continuous with very little harmonic structure left. The sharp cut-off at 72 eV is the edge of the transmission window of the aluminum filters.

ionization gating, where emission of harmonics is suppressed in the tail of the driver pulse due to ionization and depletion of the neutral ground state in the leading edge. Because this scheme does not restrict the emission of weak attosecond pre-pulses, we are not strictly speaking in the IAP regime and record spectra with residual harmonic oscillation below the cut-off spectral region.

PASSAGE

To have true isolated attosecond pulses at our disposal, we implemented and tested [174] a gating technique called Polarization ASSisted AmplitudeGatE (PASSAGE) [175]. It uses the reduced efficiency in HHG in elliptically polarized beams to suppress the emission of harmonic light in all but a single half-cycle, which leads to a broadband attosecond pulse in the cut-off spectrum. The method is particularly easy to implement, because it uses just two optical elements. A thin quartz plate (85 µm) with its polarization axis at 45° with respect to that of the beam creates two orthogonally polarized copies of the NIR pulse, which are delayed by one optical cycle with respect to each other. After passing a zero-order $\lambda/4$-plate, the two copies are counterrotating, elliptically polarized and create a field that is linearly polarized at the peak of the pulse and increasingly elliptical towards the tails. While the linearly polarized cycle can efficiently produce XUV light, the gate already suppresses adjacent half-cycles by a factor ten, if the CEP is set properly. With our quartz plate ((83.2 ± 0.5) µm) and wave-plate (B-Halle GmbH) we could show that

the correct rotation of these plates with respect to the polarization axis of the beam can effectively suppress the harmonic modulation in the spectral cut-off. With the time-varying polarization of the NIR driver pulses, it can be desirable to use an undistorted part of the NIR as the dressing pulse. To this end we implemented an external incoupling to be discussed below. The PASSAGE method has been successfully applied in e.g. [120].

3.2.2. Experimental control and interferometry

From the HHG chamber, the co-propagating NIR and XUV pulses are steered and refocused into the target cell 1.4 m downstream. The two mirrors that perform this task are a split-mirror unit that serves to introduce a time delay between the pulses and a toroidal mirror that takes care of the refocusing. Both components are hit under gracing incidence at an angle of 15° to enhance the reflectivity in the XUV. The toroidal mirror is operated in a $4f$ geometry ($f = 35\,\mathrm{cm}$) to image the HHG focus $1:1$ into the target cell and can be adjusted using a motorized 5-axis aligner [176]. To introduce a time-delay between the pulses and separate them spatially, we make use of the lower divergence of the XUV beam[5]. The split-mirror assembly therefore consists of an outer and an inner mirror that primarily serve to reflect the NIR and XUV beam, respectively. The contamination from the respective other beam is blocked in a spatial filter unit further downstream. The time delay is controlled by moving the small (2 mm × 10 mm) inner mirror on a piezo stage, thereby introducing a path length difference to the NIR beam. The interferometric stability of this assembly can be measured by recording interference fringes of a reference laser and amounts to 26 as. Since the XUV pulses are phase locked to the NIR through the generation process, this stability determines the delay resolution. Just like the toroidal mirror, the inner mirror used to be gold coated. Recently, we switched to a mirror coated with boron carbide (B_4C), which boosts the XUV reflectivity for the whole spectral range of interest (see figure 3.8[6]). A nice side effect of this material is its lower reflectivity at optical wavelengths, which reduces the parasitic NIR that keeps on co-propagating with the XUV. To block the NIR light that is reflected off the inner mirror and the XUV from the outer mirror, a filter unit with concentric filters shown in figure 3.9 (a, d, e) is used. On the inside, metal foil filters block the NIR, but are—depending on the material—transparent in different bands in the XUV (see figure 3.8). Here, aluminum foils of 200 nm thickness are the standard work horse with a transmission window between 20–72 eV. Due to micrometer perforations, these filters let a fraction of the NIR pulses pass. This leakage can be a feature [13], but is mostly unwanted. The change to the B_4C coating drastically improved this. On the outside, organic films (nitrocellulose, Kapton) block the XUV light, but are (mostly) transparent to the NIR. In total, the filter unit can house up to 4 different sets of filters, which was made

[5]For a Gaussian beam in the paraxial regime the divergence is proportional to the wavelength (eq. 2.8).
[6]The figure shows that we would benefit considerably switching the beam polarization from p to s.

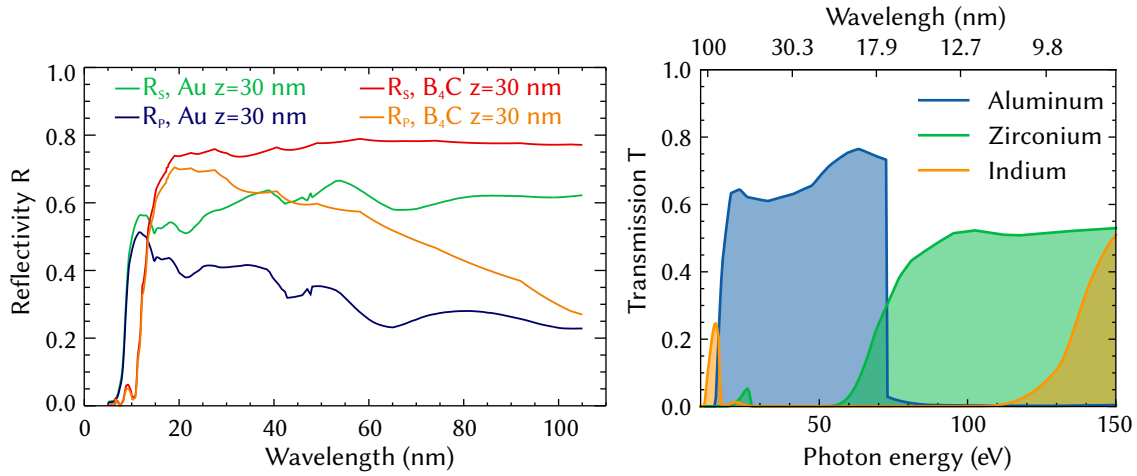

Figure 3.8.: Mirror reflectivity and filter transmission. (left) Reflectivities of 30 nm coatings of gold (Au) and boron carbide (B_4C) for *s* and *p* polarized beams at 15° gracing incidence. Courtesy from optiXfab GmbH. (right) Transmission curves for metal-foil filters of 200 nm thickness. Data from [173].

use of to introduce the dispersion in aluminum filters of different thickness as a control parameter (see chapter 5). An external XYZ manipulator is used to switch between the filters without breaking vacuum.

Besides the time delay, the other main control parameter of our setup is the intensity of the NIR pulses. It is adjusted by a motorized, closed-loop iris aperture, which cuts out parts of the NIR without affecting the smaller XUV beam. By coupling the beam out of the beamline and measuring power and focal spot size, the intensities in the target can be estimated as shown in section 4.3.3.

External incoupling

As mentioned above, it can be desirable to disentangle the NIR pulses that dress the target from those that were used to drive the HHG [7]. With the motivation to use PASSAGE for the use of attosecond streaking spectroscopy, I designed the external incoupling that was realized and used by Heldt [98]. Ultimately, it turned out that the interferometer that is spanned by splitting the NIR outside the beamline and recombining it with the XUV beam later on is too unstable to resolve sub-cycle effects without active delay-stabilization[7]. Apart from this, the external incoupling can cover a much wider time-delay range (1.7 ps opposed to the 50 fs of the inner mirror) due to the use of a retro-reflector, which is certainly beneficial for experiments on molecular targets that evolve on slower time scales and it allows to perform experiments with differently polarized dressing fields.

[7] A nice implementation of an active delay-stabilization is reported in [177].

CEP stabilization

While the oscillator provides CEP-stabilized pulses, the dispersion of the amplifier can be adjusted through active feedback to one of the fused silica slabs in the stretcher, thereby actively regulating the CEP of the whole laser system. We moved the $f-2f$ interferometer that provides this feedback (for every 4^{th} pulse) from the amplifier to the entrance of the experimental beamline to stabilize the CEP as close as possible to the point where it is actually needed. We use a parasitic reflection from the beamline's incoupling window as an input. For this purpose, we replaced the Brewster window (AOI of 57°) which minimized (maximized) the reflection (transmission) of the p-polarized light we use, with a window at 45°, which provides enough power for the CEP measurement and facilitates alignment at the same time. With this setup we can now stabilize the CEP down to 163 mrad [178]. With the stabilization in place, passive drifts of the CEP are migitated which facilitates the continuous production of IAPs over the course of a measurement, which is particularly important for attosecond streaking, where generation of attosecond double pulses results in overlapping traces [179].

3.2.3. Targets and detectors

After the spatially and temporally separated pulses have interacted with the gas in the target cell, the NIR pulses are attenuated by another motorized iris and blocked by another set of metal-foil filters at the entrance of the XUV spectrometer. The home-built spectrometer [58] consists of two interchangeable, aberration-corrected, concave gratings and a thermo-electrically cooled, back-illuminated CCD camera. Through the variable line spacing (VLS) of the gratings' grooves, the spectra are focused on a flat-field, which facilitates the capture with a flat chip without blurring. The only difference between the two gratings are the different grating constants, which make them suitable for either the spectral range of 10–56 eV or 20–112 eV. Between the gratings a stripe of silicon waver is installed to reflect and monitor the zeroth order of the beam, but the inexpert cutting of the waver seems to have introduced some aberrations into the imaging qualities of this makeshift mirror. The camera chip consists of 1340 × 400 pixels with a size of 20 µm × 20 µm. Arbitrary regions-of-interest (ROIs) on the chip can be selected for hardware binning, which speeds up data transmission and storage and reduces readout noise. The whole camera can be moved along the imaging plane on a custom-build mount to cover different spectral regions. The overall resolving power of the spectrometer is $E/\Delta E > 1500$.

XUV *in situ* reference

An important development that we engaged in over the last years, was the design, commissioning and application of the new *in situ* reference method [2]. Its principle is illustrated in figure 3.9. By installing a small transmission grating on the filter mount that

holds the concentric filters (a), the beam is diffracted into a 2D pattern (b). While the 0^{th} order is transmitted through the gas cell, the $+1^{\text{st}}$ order can pass above the specially designed cell (c), which blocks all the other diffraction orders. Finally the two diffraction orders can be spatially resolved on the camera. While the 0^{th} order can be binned to yield the absorption spectrum of the target, the 1^{st} order is undisturbed by the gas and serves as a reference. The method is valuable, because the input spectrum $I(\omega)$ can be strongly fluctuating due to the nonlinear generation process. Recording the absorption and reference spectra in the same shot yields a single-shot sensitivity down to 10 mOD and is robust against these fluctuations [60]. Since absolute optical densities can be reconstructed from this method, it is also susceptible to broad and sharp absorption structures such as continuum edges [5]. A complete time-delay scan using the *in situ* method in xenon is presented in figure 4.3, where it serves to reveal broad line deformations that would have been suppressed by conventional reference methods. Overall, the technique may very well be the tool to push ATAS further into the attosecond domain, because the sensitivity to record broad and weak spectral structures goes hand in hand with the retrieval of fast real-time events with high resolution.

Technically, the two central components of the method are the diffraction grating and the custom target cell. As a grating standard grids for sample preparation from transmission electron microscopy (TEM) are used. These come with different line spacings, which due to the limited size of the camera chip, are suitable for different spectral regions. For the photon energies considered in this thesis (40–72 eV) a stride of 12.5 µm is suited. Like our metal-foil filters, the grids were glued on makeshift wire mounts, which we have now replaced with thin steel mounts manufactured through wire-cut EDM (electrical discharge machining). Great care has to be taken that the glue is not absorbed by the capillaries of the mesh, because it is opaque in the XUV. Some pre-curing of the glue (superglue) is necessary. Further, the diffraction quality of the grids can be checked by looking at the 2D pattern of a laser pointer. Ideally, several grids can be compared against one another. The target cell is machined from Macor and was designed with the goal to minimize the material above the absorption channel which could block the reference beam. During the alignment of the cell it is vital that it does not clip either of the beams in any part of the scanned time-delay range, because artifacts would be created through such a disturbance of the one-to-one correspondence between acquired signal and reference. The same care has to be taken for the other optics (iris, filters) on the XUV beam path. A detailed account on the data massaging that is necessary to extract optical densities from the recorded full-chip images is given in [61].

3.3. Time-of-flight photoelectron spectrometer

In the course of my masters' thesis [171] we constructed our own time-of-flight (TOF) spectrometer to perform attosecond streaking spectroscopy for pulse characterization purposes. However, to achieve our ultimate goal of combining absorption and electron

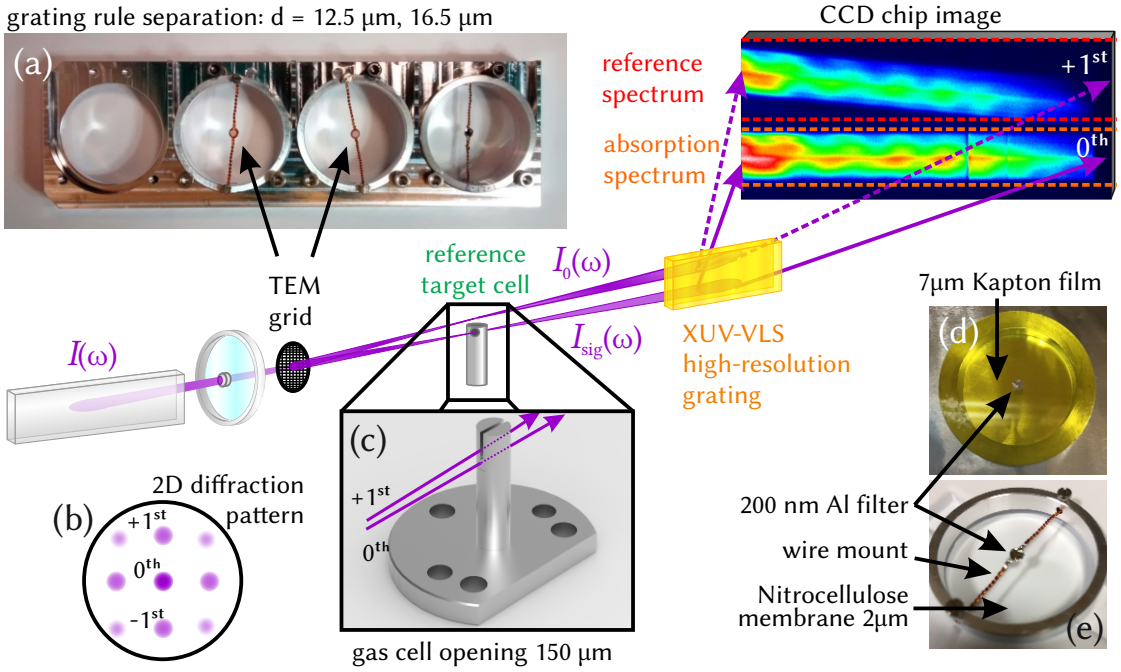

Figure 3.9.: The principle of the *in situ* reference method. The XUV beam $I(\omega)$ illuminates the filters (d,e) and TEM grids in the filter mount (a). Through diffraction in the grid, the XUV beam forms a 2D pattern (b) of which only the 0^{th} and 1^{st} order are transmitted all the way to the camera. The 0^{th} order passes the gas channel in the custom cell (c) and thereby carries the absorption signal $I_{sig}(\omega)$. The $+1^{st}$ order is transmitted above and serves as the reference $I_0(\omega)$. Both are recorded in the same shot on the camera, where $I_0(\omega)$ appears tilted due to the energy-dependent dispersion in the grid.

spectroscopy by recording spectra of both at the same time, some more development had to be undertaken. This section informs about the current state of the setup, the steps that were taken to perform ATAS and streaking measurements simultaneously and the motivation to actually do so.

To improve the streaking setup as such, the time-to-digital converter was upgraded from a system with 1 ns time resolution to one with 100 ps (TimeTagger, Swabian Instruments) and the home-build electron spectrometer was replaced by a commercial, bipolar electron and ion spectrometer (Kaesdorf GmbH). The former is crucial to achieve an energy resolution that is high enough to resolve interference between several attosecond XUV pulses, because the energy resolution is proportional to the timing resolution [180]. The next steps to improve here are the full temporal characterization of the detector electronics such as the fast amplifier and the constant fraction discriminator (CFD), as well as the commissioning of the Helmholz coils that we installed around the target chamber

to counter the earth's magnetic field. The advantage of the bipolar spectrometer is that it features an electrostatic lens [181] to focus the electrons onto the detector, which can increase the count rate for a selected range of kinetic energies of the electrons.

3.3.1. Implications of simultaneous absorption and electron spectroscopy[8]

As mentioned above, attosecond streaking allows to characterize XUV pulses (and the streaking field alongside, section 2.5.1). In the new implementation presented here, this characterization is performed simultaneously to the absorption measurements, which can benefit from the precise knowledge of the pulses. Plugging the retrieved fields into simulations of absorption measurements will help to interpret the experimental data by modeling in better agreement with the experimental conditions. For the XUV field, this includes the precise pulse structure and chirp, which have to be guessed or disregarded without proper characterization, as well as the duration of the (presumed) attosecond pulse, which limits the temporal resolution that can be traced in the measurement. For the streaking field which in our case are the NIR laser pulses that were previously used to drive the HHG, characterization is in principle possible by optical means, but an *in situ* measurement at the actual target is seldom performed. However, the latter would be desirable, because dispersion in the partially ionized HHG gas can lead to blue shifts in the pulses' spectra [182], which have to be considered since new spectral components may open up different coupling pathways than otherwise expected [7].

Furthermore, the dipole reconstruction method presented in section 2.4.4 can be improved by making the approximation that the XUV pulse is a delta function superfluous. As shown in the supplement of Stooß et al. [38], what can be reconstructed from absorption spectra alone is the temporal atomic dipole convoluted with the excitation pulse. Knowing the pulse will allow to reconstruct the true temporal evolution of the dipole with improved time resolution. With the spectral phase of the excitation pulse known, its absolute phase evolution can be extracted as well, which in turn can serve to actually measure the phases of dipole transition matrix elements.

The final selling point of our setup is that the simultaneous acquisition of both, electron and photon spectra, will enable a one-to-one correlation of these data sets. With this ability, the complementary information of both methods can be used to deepen our understanding of ultrafast electron dynamics.

[8] We would like to coin the term Broadband Attosecond Dual Absorption & Streaking Spectroscopy (BADASS) for this technique. It even works as a recursive acronym!

3.3.2. Target cell for combined absorption and photoelectron spectroscopy

The main reason, why absorption and electron spectroscopy are at the first glance mutually exclusive are the target gas pressure regimes in which they are usually operated. While in absorption spectroscopy tens of millibars are used as backing pressures in the interaction region, the microchannel plate (MCP) electron detector needs to be operated at pressures below 10^{-5} mbar. Using the entrance into the TOF spectrometer as a differential pumping stage with a 2 mm diameter is enough to lower the pressure in the experimental chamber from the usual operation level of 10^{-3} mbar to the regime that is safe for the high-voltage operation of the MCPs, but because of the close proximity of the drift tube opening and the cell, the local pressure needs to be taken into account as well. In order to capture any electrons, they need a free path from the interaction region, where they are generated through ionization, to the detector, which is at 90° to the beam path. Since this is not possible with absorption cells, it is common to use nozzles—glass capillaries with a small exit diameter—to produce a gas plume in which the ionization takes place. Testing different nozzles with diameters between 20 µm and 200 µm, it was found that streaking worked best in the range of 50–100 µm. At 200 µm the faintest signs of an absorption line could be made out with the photon spectrometer—below this the target was optically too thin—but the TMPs could not keep the chamber pressure sufficiently at bay to allow electron detection.

Thus the goal was to increase the target density for absorption without drastically increasing the chamber pressure. Conceptually this can be achieved by pulsing the target in sync with the laser. Thereby the continuous gas flow can be temporally restricted and be overall reduced. Unfortunately, these pulsed cells are either costly or require quite some expertise [183; 184]. Nonetheless, this approach could be interesting to keep in mind for experiments with extremely expensive or harmful targets, both cases in which the overall amount of gas used might be worth limiting.

The approach we chose, consisted in increasing the absorption path-length by implementing a linear gas jet array [172]. The first version was realized through nine holes with 50 µm diameter and 200 µm separation drilled into standard laboratory aluminum foil which was glued on top of a prototype cell (shown in figure 3.10). The foil could withstand backing pressures of 1 bar and the increased path-length-density-product compared to a single jet was enough to observe the first five resonances of the $2snp$ series of autoionizing states in helium. A characterization of the pressure in the different compartments showed that the TOF spectrometer could be operated at the same time. After these successful tests, the hybrid cell, as we named it, has been fully realized in steel by our mechanical workshop, because the aluminum foil is too easily cut when crossed with the laser focus. The first streaking results obtained with the prototype are presented in the following section, while the absorption results were reported in [172].

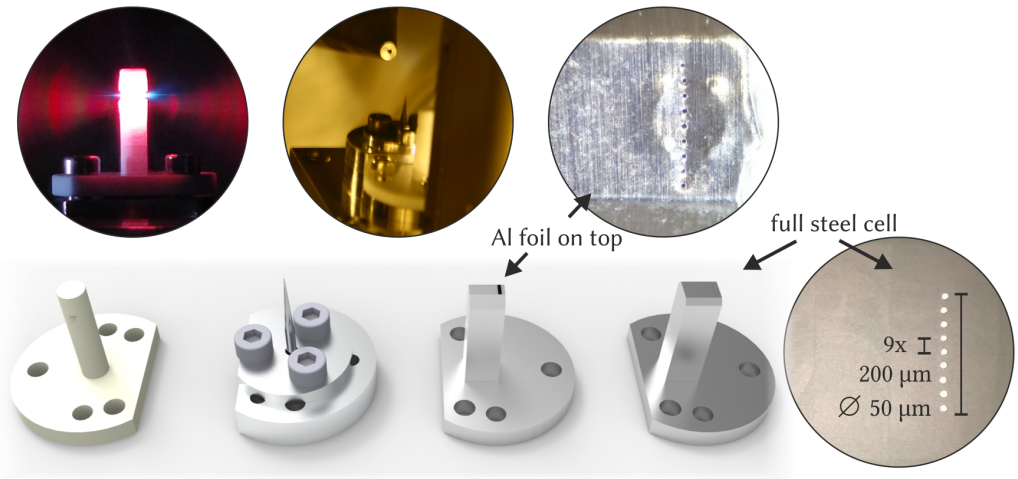

Figure 3.10.: The absorption cell evolution. From left to right: a standard Macor absorption cell, the glass nozzle used for the first streaking measurements, the prototype hybrid cell with a slit that is covered by punctured aluminum foil and the full-fledged hybrid cell machined by the workshop. The channel through the absorption cell is usually 150 µm or 200 µm, while different nozzle diameters between 20 µm and 200 µm were tested. Nine holes of 50 µm diameter and 200 µm separation were drilled into both hybrid cells. The pictures show the HHG cell in operation, a view from the nozzle to the entrance of the TOF spectrometer and the holes in both versions of the hybrid cell.

3.3.3. Attosecond streaking spectroscopy

With the hybrid cell we were able to record electron time-of-flight and XUV absorption spectra in a neon target simultaneously, which is to the best of my knowledge the first time this has been achieved. Setting the integration time of both detectors to 1000 ms the time-delay overlap region of the XUV and NIR pulses was scanned 19 times. This fast scanning mode is to be preferred over a single, slow scan (a TOF histogram can accumulate indefinitely), because the quality of the data can be accessed on scan to scan basis. E.g. the CEP stabilization loop can fail from time to time. During these times, we observed a strong drop in the electron count rate, which on average was visible in three consecutive spectra. With a whole set of time-delay scans we can mask these spectra in the data processing and obtain a clean trace free from these perturbations. As mentioned before, the CEP set value also needs to be chosen carefully to produce a single dominant attosecond pulse [179]. If a CEP value is suitable or not can be decided in less than a minute in the fast scanning mode.

While the absorption spectra that we obtained show nothing remarkable except for the fact that we were able to record them, the averaged streaking trace obtained by converting the TOF spectra to kinetic energy[9] is shown in figure 3.11. The next step is to retrieve the XUV pulse duration from this measurement using the algorithm we have

[9]How such a change in variables is implemented numerically is lined out in appendix A.2.

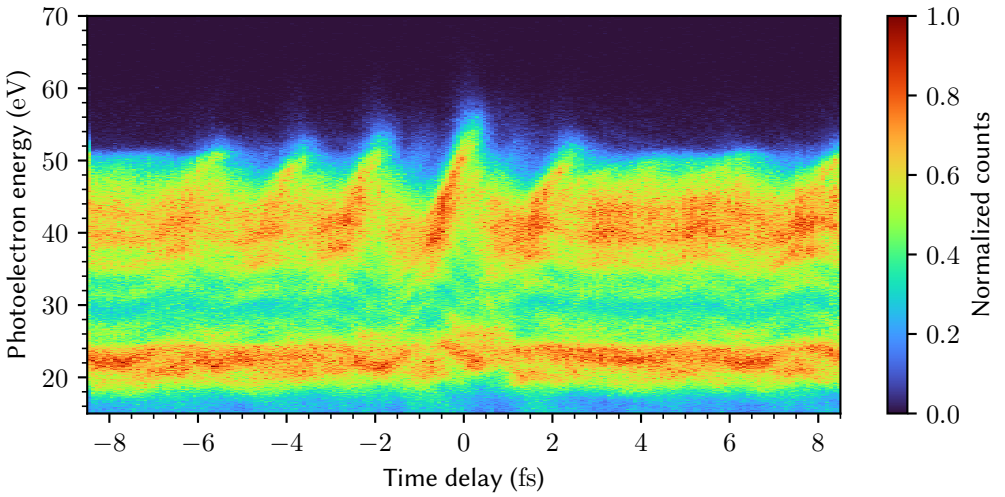

Figure 3.11.: First streaking trace recorded with the hybrid cell with HHG in argon and neon as a target gas. Electron spectra were acquired with 1 s integration time, the time delay was scanned in steps of 85 as. 19 complete scans were recorded and averaged after masking spectra with fluctuating CEP.

implemented and tested regarding its robustness to noise [3]. The NIR streaking field is arguably a few-cycle pulse with a post-pulse on the very right. (The XUV pulse is centered at zero and the time delay indicates the position of the NIR).

Even without retrieval algorithm, we can learn about the XUV pulse just from the shape of the trace. The more pronounced positive slopes of the streaked electrons tell us by comparing to calculated traces [123][10] that there is a positive chirp on the XUV pulses [185], which naturally arises in HHG for the short trajectories [179; 186].

The cut-off energy in the unstreaked spectra corresponds to the transmission edge of the aluminum filter minus the ionization potential of neon. The origin of the structure along the energy axis in the trace has yet to be determined in follow-up measurements. The dip between the two dominant traces around 42 eV and 22 eV likely reflects the structure of the harmonic spectrum with the Cooper-minimum in argon around 33 eV, but in addition one expects two traces that belong to electrons ionized from the $2p$ and $2s$ shells of neon, features that were the objects of scrutiny in the pioneering experiments performed by Schultze et al. [131]. Without additional information about the XUV spectrum which was not recorded here the two contributions can unfortunately not be separated in this data set.

[10] In case you look up the referenced figure, note that the definition of the time-delay axis is reversed.

4. Strong-field spectroscopy of xenon

While the following two chapters 5 and 6 will focus exclusively on the scientific results, this chapter serves to bundle the fundamentals that are common to the experiments presented later on. Apart from the technical point of view that the experiments were all performed with the same apparatus presented in section 3.2, the target under scrutiny was the same as well: xenon. More specifically, the objective and motivation for the research carried out in this thesis were to explore the use of strong-field generated ions as a probe for attosecond science. With the additional constraint that the target should be an easily available gas, without entailing the complexity of dealing with molecular structure, xenon becomes the prime target, as the non-radioactive noble gas with the lowest ionization potential[1] (I_p = 12.13 eV, see table 4.1).

	ΔE(eV)	T (fs)	I_p(eV)	I_p^+(eV)
Ne	0.097	42.30	21.56	40.96
Ar	0.177	23.18	15.76	27.63
Kr	0.666	6.16	14.00	24.36
Xe	1.306	3.14	12.13	20.96
Rn	3.831	1.07	10.75	21.4

Table 4.1.: Fine-structure splitting of the ground state of the singly ionized rare gas atoms and time constant of the corresponding wave-packet. Ionization potential of the neutral and the singly charged ion. Data from NIST[187].

The starting point for any investigation of ions is their production. To be able to detect them in absorption spectroscopy, requires the ionization of a sizable portion of the target gas. Because strong-field ionization depends exponentially on the field strength of the input pulses, a minimum intensity below which no ionization occurs, has to be overcome. For the case of xenon the lower limit is estimated to be $0.7 \cdot 10^{14}$ W/cm^2 (section 2.2.2), while with our pulses the ionization is saturated at just trice this value due to ground state depletion. To reach these intensities, two prerequisites have to be fulfilled: the pulses need to be optimally temporally compressed and their focus in the target has to be as small as possible. While 10^{15} W/cm^2 are easily achieved in the HHG chamber, the split-and-delay optics and filters for the temporal and spatial separation of the NIR from the XUV pulses cut away the center of the NIR beam mode, making ion spectroscopy a laborious challenge. In the experiments reported in this work, the range of $\approx 1\text{–}2.5 \cdot 10^{14}$ W/cm^2 was covered as will be discussed below. Thus, Xe^+ and with about $2 \cdot 10^{14}$ W/cm^2 also Xe^{2+} can be probed by the attosecond XUV pulses.

[1] The same reasoning applied in the measurements that lead to the discovery of non-sequential double-ionization (NSDI)[53] and above-threshold ionization (ATI) [49].

In this pulse geometry—a strong laser pulse starts the dynamics and a weak probe pulse is used to retrieve information—it makes sense to think in terms of a classical pump-probe scheme, where the pump is fixed at time zero while the XUV probe follows at a time delay $\tau > 0$. I will hang on to this notion for most of the following discussions, because it makes sense to discuss ion dynamics only when ions are present. Nonetheless, it is worth to keep in mind that a different line of thought, where the XUV triggers the dynamics and an additional laser perturbs the induced dipole afterwards, is justified as well—especially in pulse overlap. Ultimately, with the latter picture in mind, we were keen to look into the strong line-shape deformations observed in the pulse overlap, which are discussed in chapter 6. This picture is more complex since the perturbed and decaying dipole, which we measure in absorption spectroscopy, is *inherently non-local in time* [57], but precisely for this reason it leaves room for rich manipulation and physical interpretation [37; 38].

4.1. Xenon structure and transitions

In figure 4.1 a level diagram of xenon with the relevant states and transitions is shown. Through SFI xenon can be ionized to valence-hole states. In Xe^+ the two fine-structure configurations $^2P_{3/2}$ and $^2P_{1/2}$ of the $5p^{-1}$ valence-hole state exhibit a large splitting of 1.3 eV. The common term symbols $^{2S+1}L_J^m$ are used. Above 55 eV an electron from the $4d$-shell can be excited to fill the $5p$ hole, leaving the $4d^{-1}$ core-hole state either in a $^2D_{5/2}$ and $^2D_{3/2}$ configuration. Due to the dipole selection rule $\Delta J = 0, \pm 1$, three dipole transitions between the valence- and core-hole configurations are possible. These are the main probe transitions investigated throughout this thesis. For simplicity they are denoted as $T_n, n \in (1, 2, 3)$ instead of referring to the configurations involved in the transitions every time.

In Xe^{2+} the structure is similar, although more complex with more fine-structure excited configurations not all of which are displayed for clarity. From the analysis in [42] it is known that the triplet P configurations $^3P_2$, $^3P_0$ and $^3P_1$ of the $5p^{-2}$ state are predominantly populated by SFI. The transitions labeled by $T_m, m \in (a, b, c)$ are the strongest absorption lines in Xe^{2+} and were included in the analysis.

It can also be noted that both in Xe^+ and Xe^{2+} there are closed quantum pathways leading to the same final state after XUV excitation. In Xe^+ the transitions T_2 and T_3 and in Xe^{2+} T_a and T_d form such a quantum interferometer. If the SFI excitation of the fine-structure components is coherent, the beating of the spin-orbit wave-packet in the ionic ground state can be probed in ATAS. Experimental realizations of spin-orbit dynamics accessed by ATAS have been carried out for krypton [40] and neon [188].

To give a first impression of absorption spectra in xenon ions, figure 4.2 shows static spectra at different intensities of the NIR pump pulse with the XUV excitation occurring long after the SFI. The relevant transitions are labeled according to figure 4.1. The Xe^+ transitions saturate at about $2 \cdot 10^{14}\,\mathrm{W/cm^2}$ because of depletion of neutral xenon

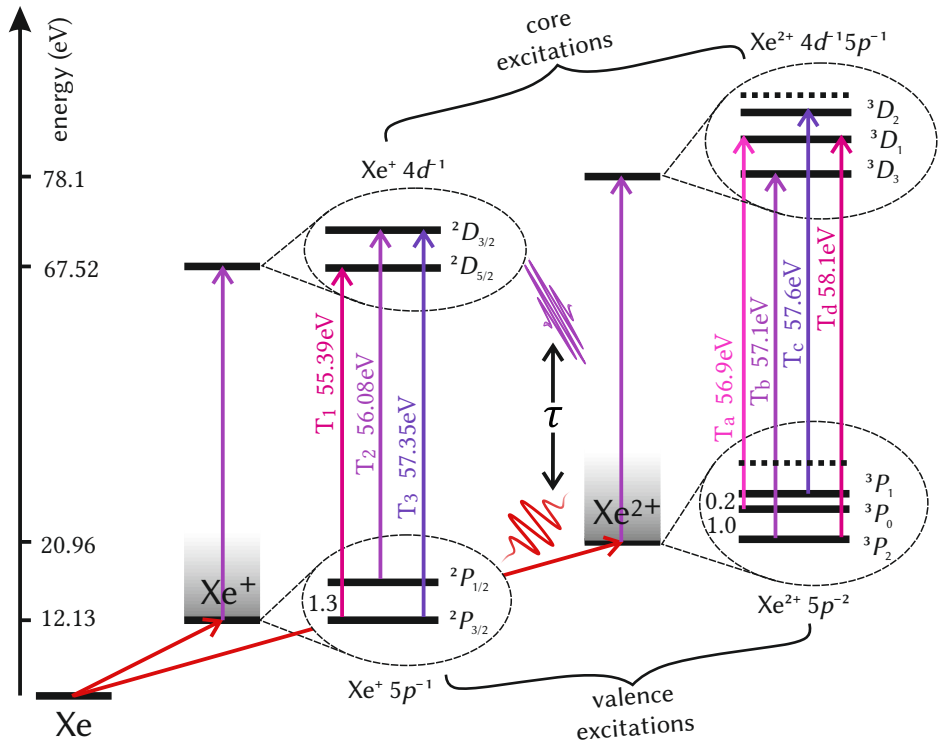

Figure 4.1.: Energy-level scheme and relevant transitions in xenon. Neutral xenon is ionized through SFI by the NIR laser pulses (red arrows) to Xe^+ and Xe^{2+} and can subsequently be excited through core-to-valence transitions by the XUV pulses. The fine-structure splittings are shown in the dashed ellipses, although for Xe^{2+} only the relevant levels are shown. The ground state splittings are indicated in units of eV. Energies are not to scale. Data compiled from [41; 42; 110].

atoms in the focal interaction volume, while this intensity is necessary to even start the production of Xe^{2+}. At the highest intensity, which is also the highest recorded in our experimental setup with the current laser to date, a number of weaker Xe^{2+} transitions appear that have not been analyzed yet.

4.2. ATAS with xenon

When the time-delay between the NIR-pump and the XUV-probe pulses is scanned over the pulse-overlap region ATAS can monitor the time-dependent buildup of the ion transition lines. Such a time-delay scan is shown in figure 4.3. On the left, the ion lines depicted above in figure 4.2 emerge from the background continuum absorption of the neutral, while on the right around 65 eV a resonance line of the neutral species is strongly perturbed. This broadening can be explained either by the suppression of the dipole emission through SFI [37; 45] or as breakdown of the rotating wave-approximation [120].

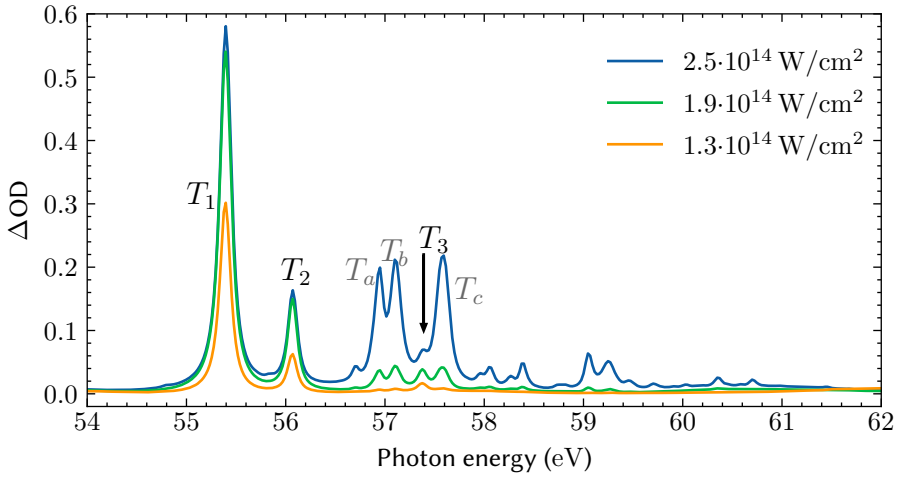

Figure 4.2.: Spectra of the xenon ion lines from ΔOD measurements at different NIR intensities.

In this measurement the *in situ* reference introduced in section 3.2.3 was used to yield spectra with low noise and to capture the absolute optical density of the target. The pulse duration was not short enough to induce coherent wave-packet dynamics in the ion as was planned for this measurement. Nevertheless, we can observe quasi-horizontal rippling across the whole spectral range between the ion and the neutral absorption lines with a period of twice the laser frequency. While part of this non-resonant, rippling structure is certainly contributed by the perturbation of the neutral lines, it is evident that the buildup of the ion lines and the asymmetry of the absorption line shapes during the buildup are a feature by themselves and not only an optical interference with the aforementioned effect. This claim can be further substantiated by considering the shape of the ion buildup in the time domain: since the time scale on which the ionization takes place is restricted to a short interval in each half-cycle, the time-dependent dipole-moment undergoes sudden changes. The spectra that are measured are in turn related to the dipole moment via a Fourier transform. Thus a sudden change in ionic dipole necessarily leads to broad spectral features. This is crucial to note, as part of this broadband feature is filtered out in the calculation of ΔODs in the following experimental sections. In the line-shape fit routines it is accounted for by a constant offset parameter for each spectrum along the time-delay axis.

It can also be noted that the buildup in ion population is not monotonically increasing as expected from standard SFI theory. Instead it is governed by peaks and valleys. These overshoots are caused by reversible polarization dynamics introduced in detail in section 2.2.2. They were first reported in [57] and underline the importance to revise even well-known phenomena as such as strong-field ionization every time higher temporal resolution is achieved in experiments or numerical treatment.

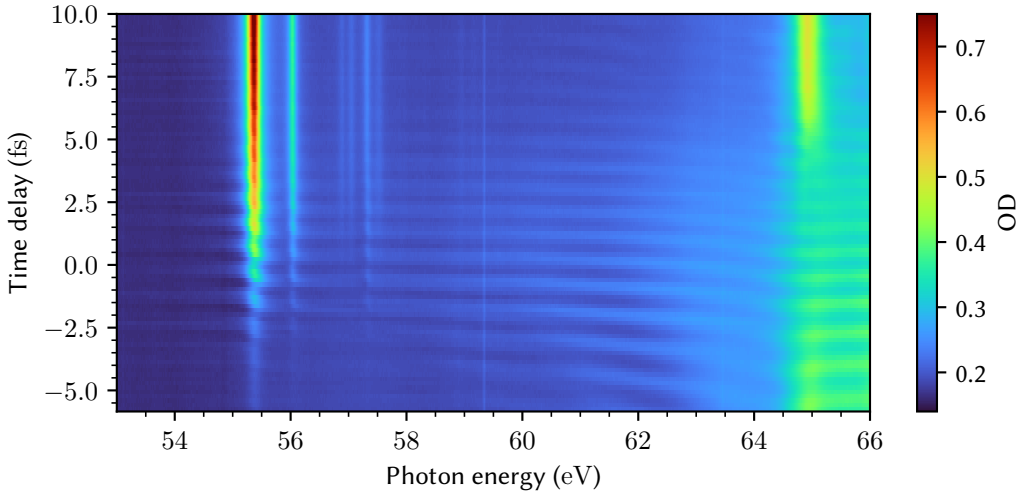

Figure 4.3.: Time-delay dependent optical density of xenon using the new *in situ* reference. For positive time delays, the XUV pulse arrives after the strong NIR laser pulse. The faint line at 59.4 eV is an artifact of a dead pixel. On its left, the buildup of the ion lines can be observed. On its right, the neutral line corresponding to the transition $4d^{-1}(^2\mathrm{D}_{5/2})6p(^2\mathrm{P}_{3/2})$ at 65.1 eV is strongly perturbed in the time-overlap region. The delay resolution is 170 as.

4.3. Data evaluation

Although the *in situ* reference has become a standard instrument in our toolbox and produces optical densities with minimal noise, it has the disadvantage of attenuating the XUV flux by an order of magnitude and therefore requires long integration times. For measuring schemes, where a large number of time-delay scans is desirable to provide a set of measurements for statistical analysis, other options to obtain optical densities are available. Besides measuring references without the gas target, the measurement of ΔODs was outlined in section 2.4.2. This approach was utilized in this work along with Fourier low-pass references, a common technique in detail explained in e.g. [2; 58]. In the latter, the references are reconstructed from the absorption spectra by low-pass filtering (see figure 3.7), which is only feasible with the broad (100 meV) xenon resonances, when the XUV spectra are very flat and contain very little harmonic structure.

True ΔOD spectra are measured by switching the dressing laser on and off between acquisitions, which is typically done by setting up a beam chopper in the corresponding interferometer arm. This is not possible in our collinear geometry, but an equivalent approach can be realized by shifting the time delay between the NIR and the XUV pulses. When the NIR pulse arrives long after the XUV pulse interacted with the sample, the perturbation of the atom is not probed anymore. Since moving the time-delay mirror with its piezo actuator is fast and readily implemented, jumping to a time-delay reference position can be used to acquire reference spectra. Care has to be taken that this reference position is still within spatial pulse overlap, because the walk-off of the XUV

beam in our geometry can lead to clipping at the absorption cell. This is not a problem in the studies presented here, since the time-delay range of interest is small (only temporal pulse overlap) and the dipole of the broad probe transitions decays in a matter of femtoseconds. Here, the time-delay reference position was set 10 fs before the first position of the scanned delay range.

4.3.1. Linear combination of references

The trouble with recording absorption and reference spectra subsequently are fluctuations in the high-harmonic spectra due to the imperfect stabilization of the HHG driving pulses [189]. Even when a reference is recorded directly after every single absorption spectrum, these lead to noise structures in the measured ΔODs. Here, a new method to improve the reference based on acquired spectra is presented.

The core idea of the method is that for any given absorption spectrum, there is a true reference which we can expand in the basis of the recorded references:

$$R_{true} = \sum_i c_i R_i. \tag{4.1}$$

If the basis set is large enough, such a superposition can recreate any spectrum. Since the XUV spectra are correlated to the driving pulses [189] through the generation process, similar driving pulses lead to similar structures over the whole spectrum. Thus, a complete spectrum can be reconstructed from segments by choosing the right coefficients c_i based on the part that is available. Mathematically, this corresponds to finding the vector of the coefficients $\boldsymbol{c}$ that solves $\boldsymbol{Rc} = \boldsymbol{s}$ for any spectrum $\boldsymbol{s}$ given the matrix of references $\boldsymbol{R}$ with the individual measured references as columns. This problem can be solved numerically for every spectrum, even when sections of the spectra and the corresponding parts in the references are omitted in the calculation.

Now the main assumption of the method is that far away from resonances the absorption spectra carry no imprint of the light-atom interaction and that these parts can be used to reconstruct the reference over the whole spectrum as outlined above. While this is certainly not valid for the general case, in singly charged xenon, the off-resonant cross-section is close to zero below the giant dipole resonance at photon energies > 79 eV. The reconstruction regions were therefore set to 45.5–51.9 eV and 61.3–64.0 eV as indicated in figure 4.4. In comparison with the directly measured ΔOD, residual harmonic-structure-noise is greatly suppressed while the shape of the absorption lines is preserved.

A similar method dubbed 'edge referencing' has recently been published [190] and is included in the further analysis for comparison. Here, the same reference spectra and reconstruction regions (edges) are used to calibrate a correlation matrix that can be used to correct the harmonic fluctuations.

Both methods are tested for their effectiveness as illustrated and quantified in figure 4.5. Focusing on time-delay lineouts at off-resonant energy pixels, where no absorption signal is expected, the fluctuations in the ΔOD around 0 mOD are presented as his-

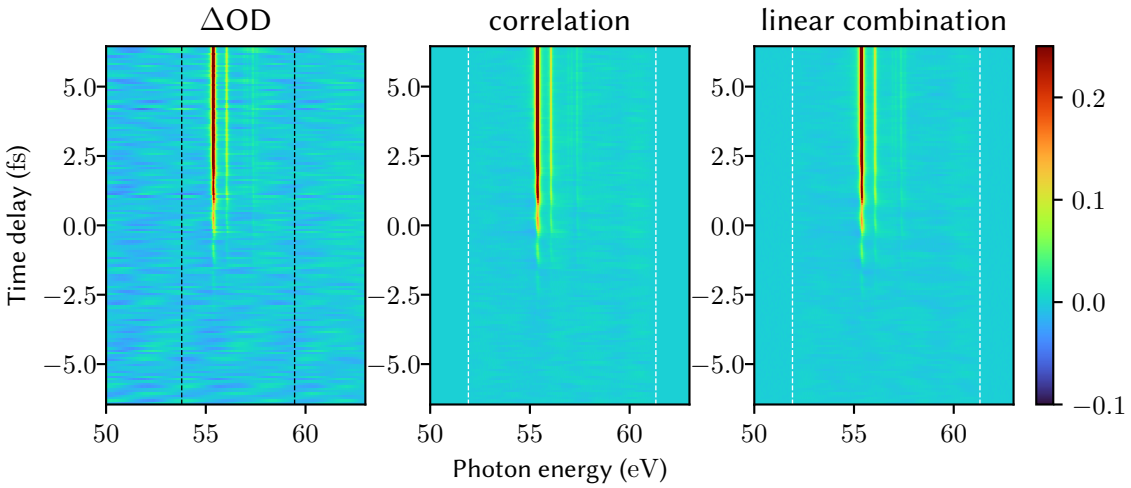

Figure 4.4.: Comparison between the ΔOD of a directly measured time-delay scan (left) and the improved versions using either the correlation matrix as published in [190] (middle) or a linear combination of references as devised within the work of this thesis (right). The borders of the off-resonant edge regions are marked by the white, dashed lines. The black, dashed lines mark the pixels used for qualitative analysis as described in the text and figure 4.5. The color scale is cropped such that weak structures are emphasized.

tograms and correlation plots. Through Gaussian fits to the distributions we can assess that both the fluctuations on a single pixel as well as on the correlation between different pixels is improved four-fold by either method relative to the direct ΔOD calculation. At the same time, the isotropy of the correlation plot shows that no systematic shifts are present in the experimental data to begin with. The final noise level of our measurements is determined in figure 4.6. The standard deviation in the signal-free time-delay region at $\tau < -5.2$ fs is extracted and fitted by a Gaussian to obtain the average noise level accross the spectral region of interest. While the noise in the directly measured ΔOD exhibits residual harmonic structure and amounts to an error of 8 mOD, the method presented above is mostly flat at a level of 2 mOD. Two parameters that affect the noise level are examined more closely in figure 4.7. Here, the noise at negative time delays is plotted as function of the width of the edge regions and the number of spectra available as references. It demonstrates that especially when the number of reference spectra is low, the edge regions need to be sufficiently large, though beyond a certain size there is no further improvement. The number of spectra need not be infinitely large to reach the lowest possible noise level since it seems that an asymptotic limit is reached for each edge region. This is good to have in mind for the acquisition of the data, because it means more spectra won't necessarily improve the outcome. Of course all the available spectra and the largest edge region were used for the data presented in chapter 6 to achieve the lowest noise, although this analysis shows that the constrains could have been more relaxed without putting the venture at jeopardy.

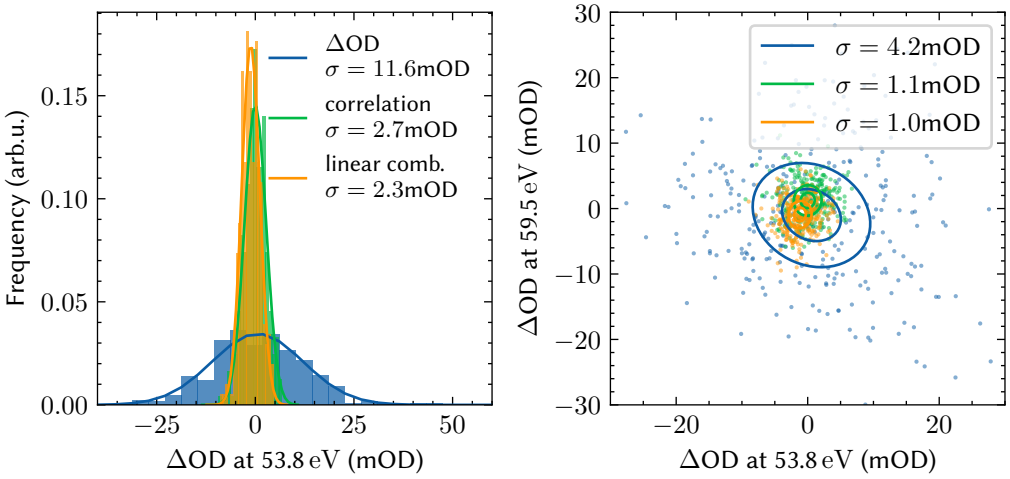

Figure 4.5.: Noise reduction on pixels without signal. (left) Histogram of the ΔODvalues on a single pixel along a time-delay scan. (right) Correlation between two pixels. Gaussian fits to the distributions highlight how both methods applied to the data mitigate the fluctuations and reduce the noise roughly by a factor of four.

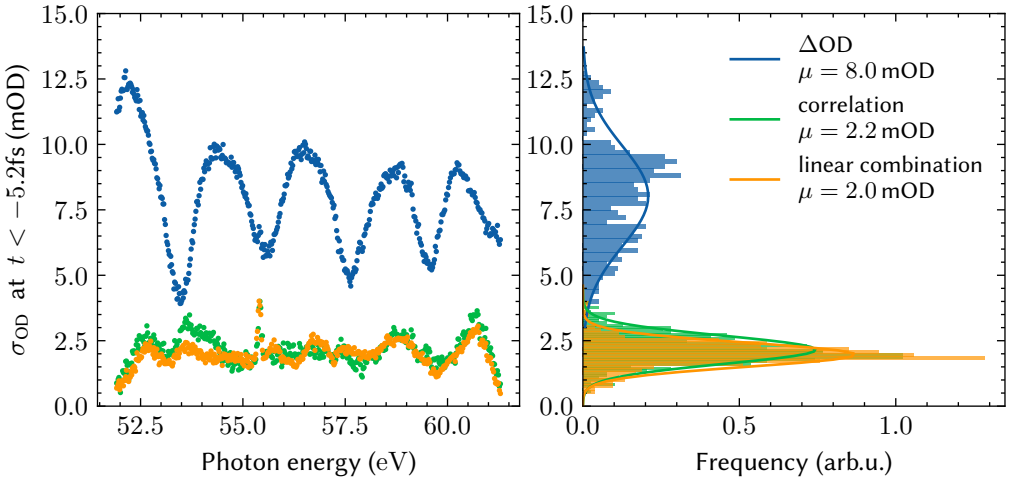

Figure 4.6.: Estimation of the measurement noise level. (left) Standard deviation of the ΔODs in the time-delay region $\tau < 5.2$ fs, before the buildup of the ion absorption lines and (right) the corresponding histograms. Residual harmonic structure in the noise is greatly suppressed and the overall measurement noise is improved by a factor of four.

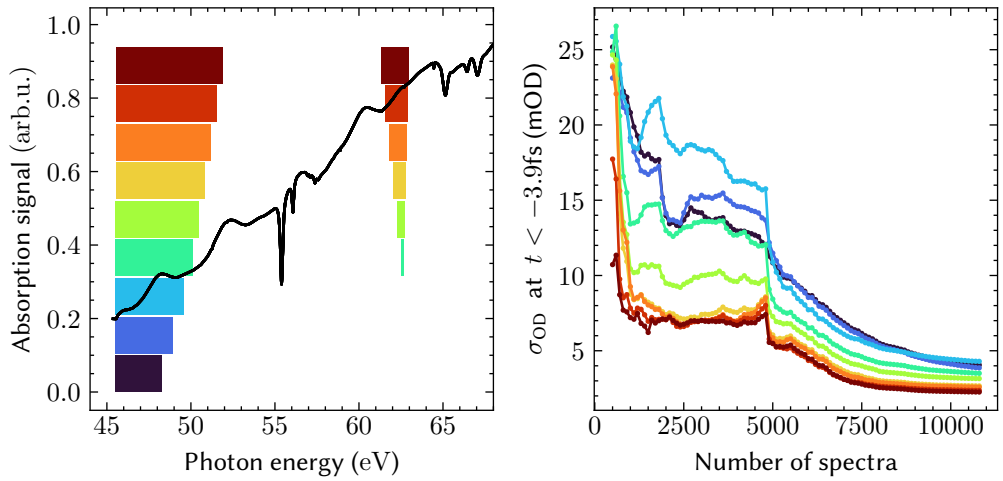

Figure 4.7.: Influence of the edge region and the number of spectra used to calculate the references. (left) Different edge regions around the resonances of interest. (right) For each color-coded edge region, the noise level at negative time delays is plotted as a function of the number of spectra used in the reconstruction.

To conclude, a new reference method, using a linear combination of all measured references was devised that can reduce the measurement error and stands up to the performance of a similar technique based on extracting correlations in the harmonic structure [190].

4.3.2. Energy calibration

For the calibration of the spectral camera axis, the xenon ion lines discussed earlier and the neutral absorption lines of the $4d \longrightarrow np$ series were used. Literature values for these transitions were taken from [110; 115]. Since the q-value of the neutral lines is known to be 200 and the width of the lines is $\approx$ 100 meV, they can safely be fitted by Lorentzian line shapes to yield a pixel to energy correspondence. This relation can be fitted either by a low-order polynomial or the grating equation (see [174]). An example of such a curve is shown in figure 4.8. Since the pixel-energy relationship is nonlinear, the photon energy is not sampled in evenly distributed bins. This can either be fixed through resampling of all spectra or by simply using the calibration curve as the photon energy axis.

The true energy resolution of the apparatus on the other hand is best determined by adding it as a parameter δE to the fit routine. To mimic the apparatus, transmission spectra are imitated to apply the convolution with δE instead of the direct application on the optical densities:

$$\mathrm{OD}_{\mathrm{fit}}(\omega) = -\log\left(10^{-\mathrm{OD}_{\mathrm{model}}(\omega)} \ast G_{\delta E}(\omega)\right), \tag{4.2}$$

where the $\ast$ symbolizes the convolution with a Gaussian function $G_{\delta E}(\omega)$. The standard deviation δE was found to be 22 meV through fitting the ion spectra out of time-delay overlap. This corresponds to a FWHM of 50 meV and is in agreement with previous characterizations[2].

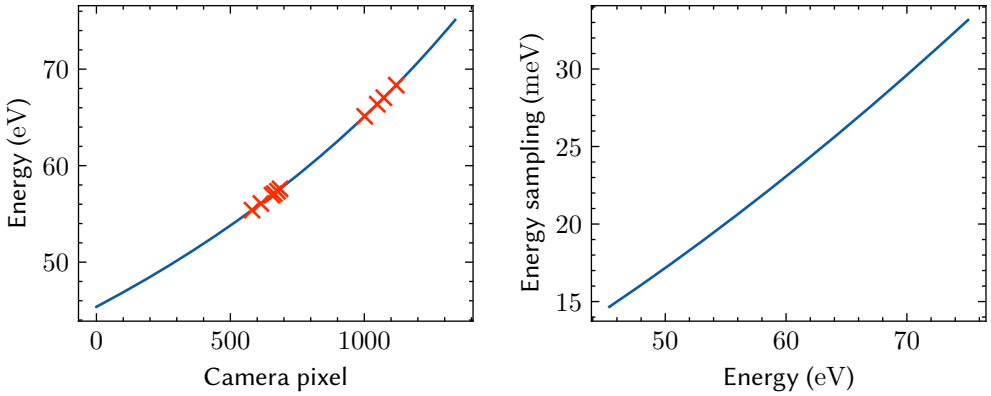

Figure 4.8.: (left) Energy calibration curve obtained by fitting the inverted grating equation to the resonance positions of xenon resonances (red). (right) The sampling is highest at low photon energies. At 55 eV it is 20 meV.

4.3.3. Intensity calibration

Since the intensity of the NIR pulses was used as a control parameter in the study presented in chapter 6, calibration measurements were performed in between of two blocks of experimental runs. Alongside with power measurements, beam profiles were recorded for every iris position, since cutting the beam does not only attenuate it but changes its diameter and therefore the focus size as well. The 2D images of the focus were fitted with a Gaussian beam profile (see equation 2.9, [172]) to extract the waists W_a, W_b along the semi-major and semi-minor axes. With this, the on-axis peak intensity is evaluated as

$$I_0 = \frac{2P}{\pi W_a W_b} \frac{1}{T_{NIR} f_{rep}}, \tag{4.3}$$

with the measured power P, the pulse duration T_{NIR} and the laser repetition rate f_{rep}. The average intensity, which due to alignment imperfections and focal volume averaging is a better estimate of the experimental conditions is simply half this value and is presented in figure 4.9. The largest uncertainty in the final result stems from the pulse duration T_{NIR}. Even though it was measured using the D-Scan described in section 3.1.2 to be 4.1 fs, this measurement was performed in front of the beamline and not *in situ* in the target chamber. In addition the retrieved pulse shape is not a perfect Gaussian and as a concequence a large part of the pulses power is not contained within the ΔT_{FWHM} duration of

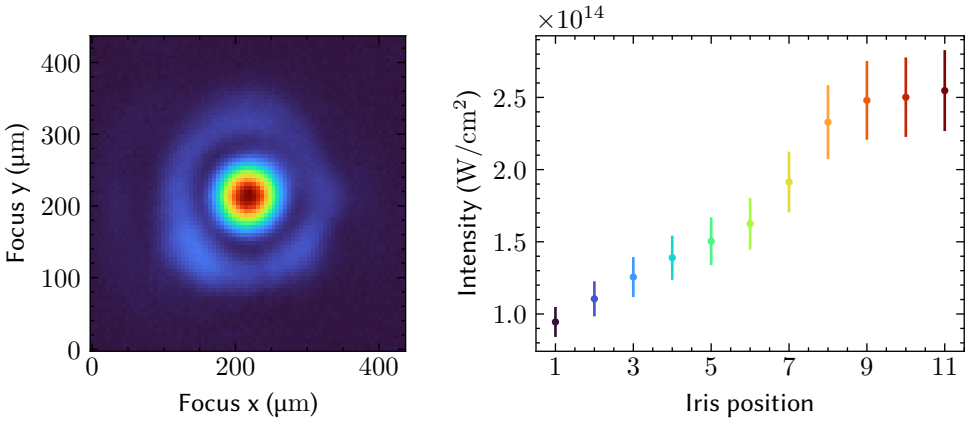

Figure 4.9.: Intensity calibration measurements. (left) Beam profile at iris position 8. Average intensities as a function of the iris opening calculated from the fits to the beam profiles and corresponding power measurements.

the pulse. As the D-Scan results show, the peak power of the retrieved pulses is a factor of two lower than the corresponding Fourier limited pulse. Thus the measured intensity is scaled down by this factor. The results show that a range of $1\text{–}2.5 \cdot 10^{14}\,\mathrm{W/cm^2}$ is scanned. These estimates are further evaluated by comparing the experimental buildup of the ionic absorption lines with the theoretical ion yields of ADK ionization rates of xenon (see section 2.2.2) and found to be agreement with these calculations.

4.3.4. Path-length-density estimation

Because the ions are generated from the neutrals the portion of the target that is ionized can be determined. To do so, we estimate the path-length-density-product ϱL, which relates the optical density of the target to the absorption cross section σ. From Beer-Lambert's law (section 2.4.3) we obtain:

$$\mathrm{OD}(\omega) = \frac{\varrho L}{\ln(10)}\sigma(\omega). \tag{4.4}$$

Now ϱL can be estimated by considering individual transitions of the neutral and ionic species. At the highest intensity (see figure 4.2) we get OD $\approx$ 0.6 and an XUV photoionization cross-section of 50 Mb for T_1 in Xe^+, while for T_c in Xe^{2+} the numbers are OD $\approx$ 0.22 and σ = 40 Mb. Without the pump pulse we similarly obtain OD $\approx$ 0.26 and σ = 14.2 Mb for the neutral $4d^{-1}6p(^2D_{5/2})$ transition at 65.1 eV [115]. As a result we get

$$\varrho L_{Xe+} = \frac{0.6\ln(10)}{50\,\mathrm{Mb}} = 2.7 \cdot 10^{16}\,\mathrm{cm^{-2}} = 0.77\,\mathrm{a.u.}$$

$$\varrho L_{Xe2+} = \frac{0.22\ln(10)}{40\,\mathrm{Mb}} = 1.3\cdot 10^{16}\,\mathrm{cm}^{-2} = 0.36\,\mathrm{a.u.}$$
$$\varrho L_{Xe} = \frac{0.26\ln(10)}{14.2\,\mathrm{Mb}} = 4.2\cdot 10^{16}\,\mathrm{cm}^{-2} = 1.20\,\mathrm{a.u.}$$

The ratio $\varrho L_{Xe+}/\varrho L_{Xe2+}$ and the sum of the path-length-density-products of the ionic species $\varrho L_{Xe+} + \varrho L_{Xe2+} \approx \varrho L_{Xe}$ demonstrate that we manage to completely deplete neutral xenon and can obtain an ion ratio of $Xe^+/Xe^{2+} \approx 2/1$.

4.3.5. Pressure correction

Because the optical density of a target depends linearly on the density of the target gas, fluctuations in the gas pressure of the absorption target lead to fluctuations in the OD as well. When the applied pressures are recorded, they can be used to correct the experimental results. With the measured pressures p and their mean $\langle p\rangle$, the optical densities can be rescaled to yield less noisy scans:

$$\mathrm{OD}_{\mathrm{corr}} = \mathrm{OD}\,\frac{\langle p\rangle}{p}. \tag{4.5}$$

An example of this method is given in figure 4.10 for the neutral $4d \longrightarrow 6p$ line in a reference time-delay scan with closed iris (no NIR). The lineout of the raw absorption data at the resonance energy of the absorption line and the backing pressure of the target cell show a clear anti-correlation. Unfortunately, the pressure was only saved up to the first decimal digit, otherwise the correction could have performed even better.

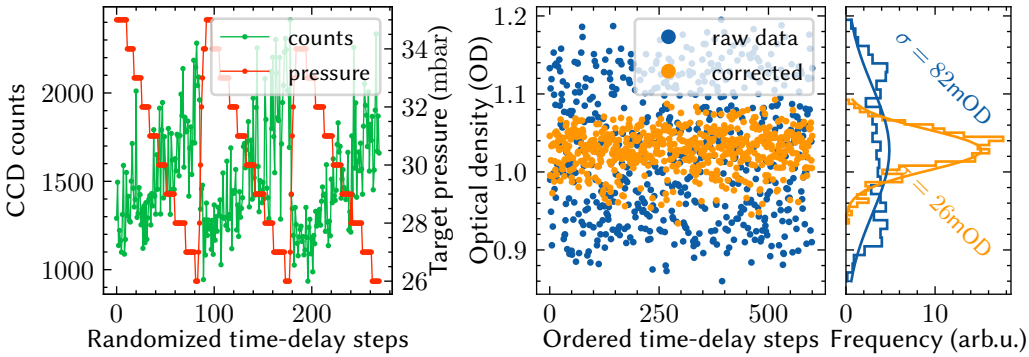

Figure 4.10.: Demonstration of the pressure correction. (left) The lineout through the raw absorption data (green) and the target pressure (red) are anti-proportional. (right) The optical density before (blue) and after (orange) the correction. Fits to the histogram show a threefold improvement in stability.

5. Attosecond precision in delay measurements

The very heart of the field of quantum dynamics is to resolve ultrafast processes directly in the time domain. Different implementations of photoelectron spectroscopy have been able to trace electron dynamics down to the atomic unit of time (1 a.u. $\approx$ 24 as); see section 2.5.2. While these techniques differ in the configurations of light fields they use to stimulate non-equilibrium electron dynamics, their joint objective is the extraction of attosecond delays between electrons released from bound and continuum states. So far attosecond transient absorption spectroscopy (ATAS) has mainly been used to probe attosecond dynamics and couplings among states [13; 40; 191], but is left out in the investigation of delays, for which access to the XUV spectral phase or the phase of dipole-transition matrix-elements is necessary. Consequently, no XUV pulse characterization scheme in an absorption geometry exists to this day.

This chapter presents an approach towards direct, quantitative attosecond delay measurements based on ATAS. Using the phase-sensitivity of the oscillating, sub-cycle buildup of ion population, it employs the resonant photoexcitation of three XUV transitions to quantify deliberately induced delays between photons at different XUV energies. The central achievement is the finding that this method reaches a precision of less than 5 as in quantitative delay measurements, which meets the demands of possible envisioned applications presented in the outlook in section 5.5. Most of this chapter's content is based on [1] and will adhere to this publication.

5.1. Experimental methods

The near-infrared (NIR) laser pulses used in this study have a duration of 4.5 fs, as characterized by the D-Scan method (section 3.1.2). They were used to drive HHG in neon, which results in quasi-continuous XUV spectra with very little harmonic structure (figure 3.7). Next, the co-propagating XUV and NIR pulses are spatially separated by concentric filters before they are refocused into the target gas cell (figure 5.1). The key control parameter of this experiment is the thickness of the metal-foil filters that remove the residual NIR light from the central XUV beam. Three individual sets of these filter assemblies can be selected via our filter unit. By mounting aluminum filters of varying thickness, the dispersion in the XUV beam path before the target can be altered. The peak intensity of the NIR pulses at the location of the target is estimated to be $\approx 1 \cdot 10^{14}$ W/cm^2 and was adjusted such that xenon is predominantly singly ionized. No independent char-

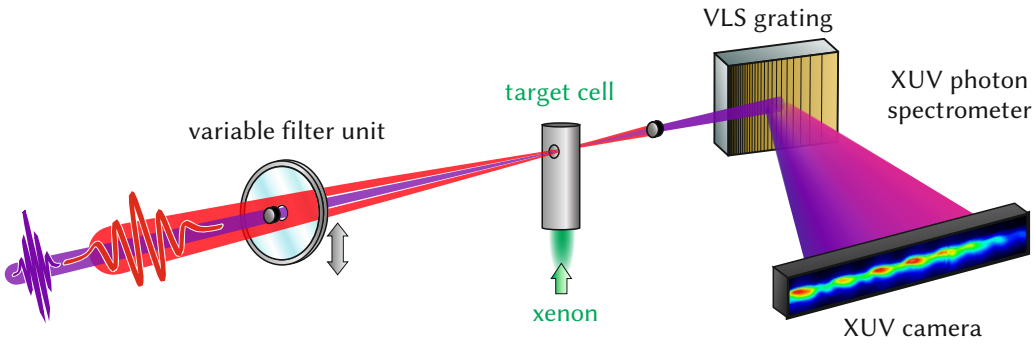

Figure 5.1.: Experimental setup. The co-propagating XUV and NIR pulses are focused into the target gas cell. The XUV beam is monitored in a home-built spectrometer, consisting of a variable-line-space (VLS) grating and an XUV camera, with an aluminum filter to block the NIR light behind the target cell. The GDD of the XUV pulse can be controlled by switching between assemblies of metal-foil filters of different thickness in a variable filter unit before the target cell.

acterization of the intensity was performed for this experiment, but the ratio of Xe^{+} to Xe^{2+} lines and the consistent comparison with the independent studies [119] confirms this estimate.

By scanning the time delay between the XUV and NIR pulses, the time-dependent buildup of xenon ion population through the XUV absorption of the $4d$-core to $5p$-valence transitions (see section 4.1) is observed. The attosecond time-dependent buildup of ionic population is governed by reversible and irreversible ionization dynamics, which have been investigated in detail by Sabbar et al. [57] (see section 2.2.2). Here, this oscillatory signature is used to clock the excitation by the XUV pulses across three different core-to-valence transitions (T_1, T_2, T_3). The dispersion in the XUV beam path is varied by inserting aluminum filters of different thickness, and hence manipulate the group-delay dispersion (GDD) on the XUV pulse in a controlled manner. This has for instance been used for the temporal compression of attosecond pulse trains with photon energies below 45 eV [185]. The analysis is tested thoroughly using a statistical, numerical model and one finds that relative delays induced by the metal-foil filters can be accurately retrieved with a precision better than 5 as.

The aluminum filters supplied by the company Lebow are mounted on home-built wire mounts to achieve total filter thicknesses of 200 nm, 400 nm or 600 nm. The 400 nm and 600 nm filters each consist of two individual filters mounted in pairs ($400 = 200 + 200; 600 = 500 + 100$) to obtain the desired thickness with the filters available. For each filter 36 individual time-delay scans are recorded with an incremental delay step size of 170 as. A switch between different filters is performed every nine scans to decrease the influence of long-term drifts in the setup. The absorption spectra are extracted from the measured transmission spectra by using Fourier low-pass references which yields the optical density defined as $\mathrm{OD} = -\log(I/I_{\mathrm{ref}})$ and which is directly proportional to changes in the resonant absorption cross-section. The optical density averaged over all

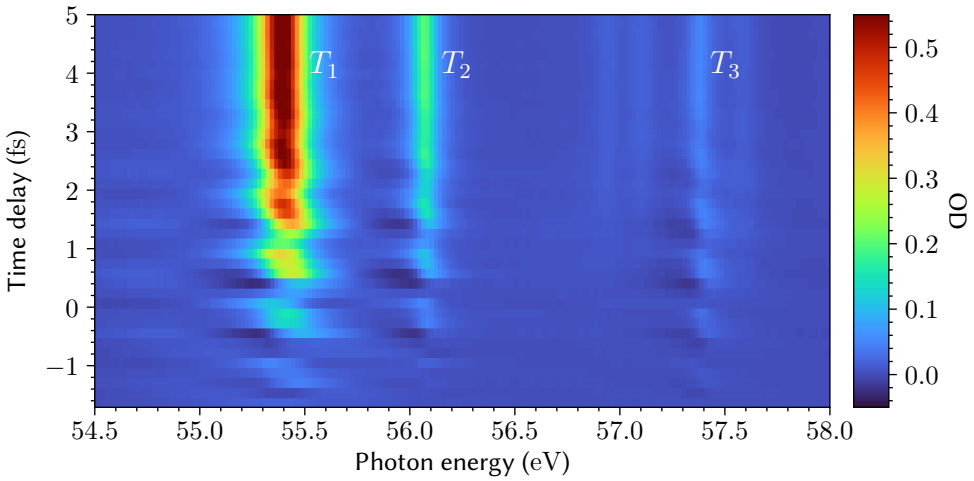

Figure 5.2.: Time-delay dependent optical density averaged over all 108 scans. For positive time delays the NIR pulse precedes the XUV.

108 time-delay scans is shown in figure 5.2. Since the detector integration time needs to be scaled in order to compensate for the varying attenuation of the XUV photon flux by the different Al filters, each single spectrum was averaged over 750, 1800 or 3600 laser shots, respectively, aiming for a constant photon count on the detector for all filters.

5.2. Results

As the ionic population is probed in temporal overlap with the femtosecond NIR laser pulse, strong-field-induced line-shape modifications [91; 99] are observed on the naturally Lorentzian-shaped resonances [110; 115]. The focus of the analysis lies on delay-dependent lineouts of the OD at the resonance energies of T_1, T_2 and T_3, respectively (see figure 4.1). A representative lineout at T_2 is shown in figure 5.4. In order to extract attosecond timing information, the lineouts are Fourier transformed along the time-delay axis and the phase is read out at the Fourier peak that corresponds to the sub-cycle oscillation in the ionic buildup (figure 5.4). The phase φ of each oscillation is related to the delay τ of the buildup via $\varphi = f_{osc}\tau$, where f_{osc} is the oscillation period of the NIR laser cycle of $\approx 2\pi \cdot 1.07\,\mathrm{fs}^{-1}$. No such oscillation is expected and observed for positive delays later than 3.5 fs, i.e., when the NIR with its 4.5 fs FWHM duration fully precedes the XUV. Therefore, a smooth cosine-squared taper function is applied for time delays greater than 3.5 fs. This avoids artifacts in the Fourier analysis that originate from discontinuities at the edges of the data array as illustrated in figure 5.4. In the absence of an absolute timing reference the relative shift of the oscillation phase are evaluated between adjacent resonances in dependence on the thickness of the aluminum filter, the

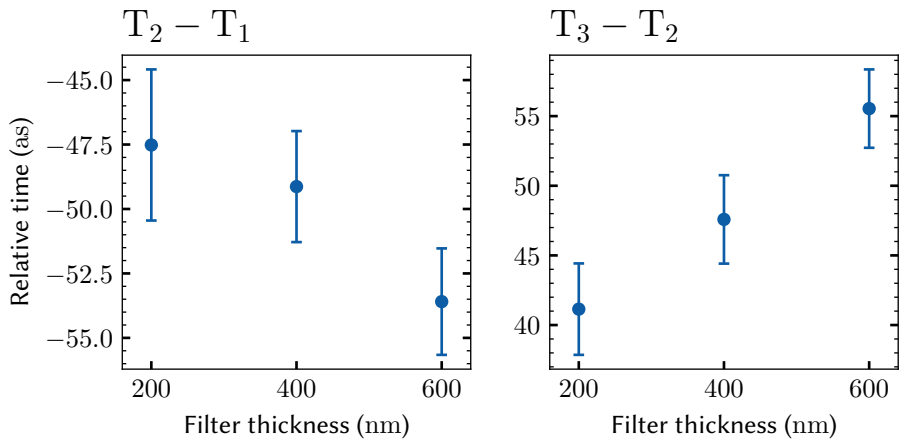

Figure 5.3.: Results for the relative time delay between the buildup of consecutive resonances in dependence of the aluminum filter thickness. The error bars correspond to the standard error of the mean computed from the set of 36 time-delay scans per filter.

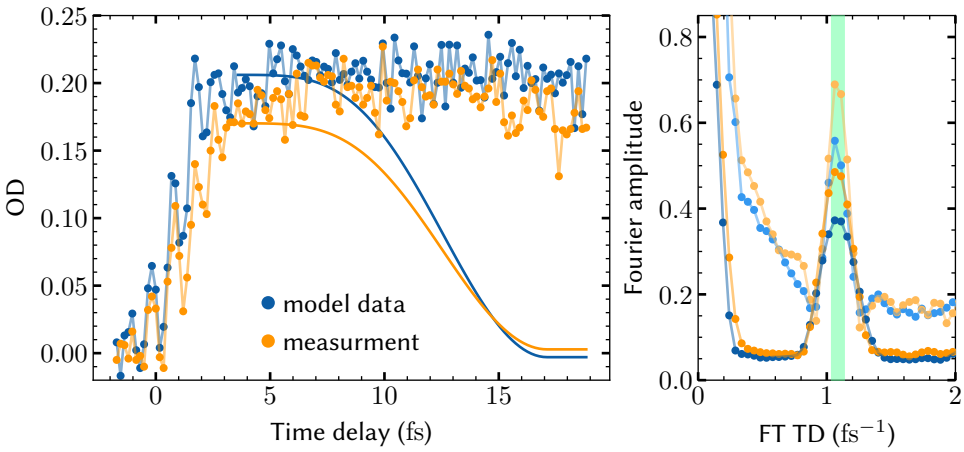

Figure 5.4.: Illustration of the delay reconstruction method. (left) Single time-delay lineouts of T_2 from measurement (orange) and model data (blue) with (lines) and without (data points) tapering in the time-delay region between 3.5 fs and 18.8 fs. (right) Fourier transformation of lineouts on the left with (bold) and without (faint) applying the taper function. The oscillation phase φ and thus the delays are read out in the green shaded area.

results of which are presented in figure 5.3. A clear, systematic linear trend in the relative timing of the different spectral components on the order of a few attoseconds is observed as the thickness of the metal-foil filters is increased.

The observed trend can be explained as follows: while the SFI of the neutral xenon is governed by the NIR laser field (independent of the Al filter thickness), the measured transition strength in the ionic species depends on the relative timing of the different spectral components of the XUV pulse which probes the ion population. By changing

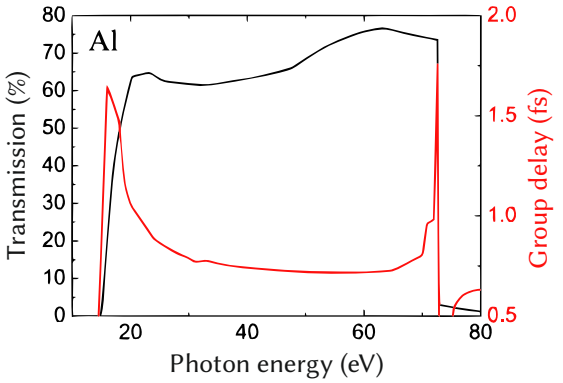

Figure 5.5.: Transmission (black) and group delay (red) of a 200 nm thin-foil aluminum filter. Around 55 eV the group delay is practically constant, leading to a group-delay dispersion close to zero. Modified from [186].

the aluminum filters, the XUV dispersion is modified and thereby changes the relative group delay of the attosecond XUV pulse across the different resonant transition energies. Our measurement reveals a change in group delay of only few attoseconds per 200 nm aluminum material. As far as the precision of tabulated data is suitable for this assessment, this change is in agreement with literature [185; 186], with reported values of the GDD close to zero for our photon energy range. Figure 5.5 shows the general trend of the group delay of a 200 nm aluminum filter, which is flat in our region of interest, with only a coarse sampling of the energy axis. The absolute delay that can be obtained by extrapolating the slope to zero filter thickness consists of contributions from the spectral phase of the XUV pulses and the atomic transition phases. These contributions from both quantities can in principle be disentangled via theoretical calculations (of the atomic transition phases) or established XUV pulse characterization techniques [135].

5.3. Statistical analysis

In order to quantify the sensitivity of our measurement and to rule out systematic shifts of the Fourier delay-extraction method, a statistical model is employed for validation. This is done by modeling the oscillatory signal in the likeness of the measurement (see figure 5.4) while controlling the input phases φ. The ion buildup signal is modeled by a sigmoidal step function with an additive sinusoidal oscillation:

$$f_{model}(t) = A_{step} \cdot \frac{1}{2}\left[1 + \mathrm{erf}\left(\frac{t+\tau}{\sigma}\right)\right] + A_{osc} \cdot \sin\left[(t-\tau)f_{osc}\right] \cdot \exp\left[-\frac{(t-\tau)^2}{2\sigma^2}\right] \tag{5.1}$$

where A_{step} and A_{osc} are the amplitudes of the step and the oscillation, τ and σ are the absolute timing and the width of the step and f_{osc} is the frequency of the oscillation. All parameters except τ were estimated by fits to the combined data set. The phase of the oscillation $\varphi = f_{osc}\tau$ is varied for the models of the individual lineouts of the three transitions T_1, T_2, T_3 in order to investigate the reconstruction of the relative delays $\Delta\tau = \tau_{(T_i)} - \tau_{(T_j)}$, where $i = 2, 3$ and $j = i - 1$.

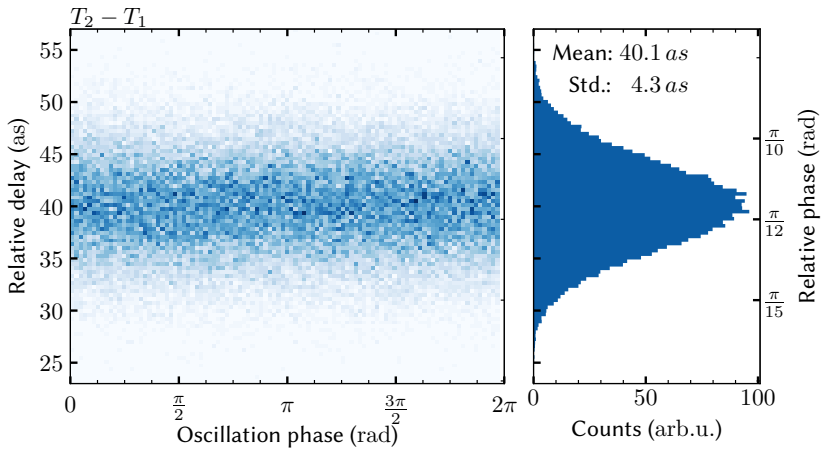

Figure 5.6.: Analysis of the delay reconstruction method. (left) 2D histogram of the reconstruction of the relative delay between T_1 and T_2 from model data. The input delay here was set to 40 as and the result does not change as the overall input phase is scanned over a complete cycle. (right) Phase-integrated histogram of the reconstructed delay under the influence of noise. The method is accurate in that it reconstructs the correct input delays of 40 as and its precision is better than 5 as. Both plots have the same ordinates, where the left axis shows the relative delay and the right axis shows the relative phase, respectively.

Applying the Fourier method mentioned above to data generated using the model function in equation 5.1, we find that the delay retrieval has no bias in the absence of noise and accurately reconstructs the relative delay differences $\Delta\tau$ between the ion buildup of consecutive resonances. To examine the influence of noise on the delay reconstruction, the width of the noise distribution is estimated from the experimental data and accounted for as additive Gaussian noise to the model. Using the same sample size of $n = 36$ as the experimental data, this randomly generated noise is applied to each modeled lineout from which the input delays are subsequently reconstructed. A single delay is computed from these as the average of the 36 reconstructions and this process is repeated 10000 times in order to sample the distribution of delays upon application of noise to the model. The retrieval for different input delays $\Delta\tau$ was tested from zero to several 100 as and it is found to be both accurate in the sense of reconstructing the correct input value, as well as it is precise with a standard deviation below 5 as. Figure 5.6 shows the reconstruction for a delay difference $\Delta\tau = 40$ as between lineouts of the transitions T_2 and T_1, where in addition the overall phase is varied in 100 steps over a complete cycle of the signal oscillation and each of these histograms is sampled by 500 individual reconstructions. It also displays the data integrated over the phase variation, thus representing a collection of 50000 reconstructed delay differences. The analysis shows that the width of the densely sampled distribution of reconstructed delays was correctly estimated for the measurement results by the standard error of the mean of each individual experimental result, which justifies the error bars presented in figure 5.3.

5.4. Discussion

The central finding of the measurement and analysis presented here is that the sub-cycle oscillations in the ionization dynamics can be exploited to reconstruct attosecond delays of the XUV probing accurately and with a precision better than 5 as by using attosecond transient absorption spectroscopy. The clear experimental evidence is the change in relative delay between the excitation of three probe transitions which scales linearly with the change in filter thickness as can be expected. The analysis and numerical model of the delay reconstruction confirms the validity and precision of the method. Figure 5.7 demonstrates that this precision is sufficient to resolve an XUV field cycle over the whole range of photon energies that typical tabletop HHG setups can deliver. Thus changes in the reconstructed phases can be sampled fine enough for, e.g., attosecond pulse characterization purposes. The next step is to utilize the ability to access energy-specific group delays imprinted onto the XUV pulses to develop an all-optical attosecond pulse characterization within ATAS or to use it to access the phases of the transition dipole, i.e., delays in excitation.

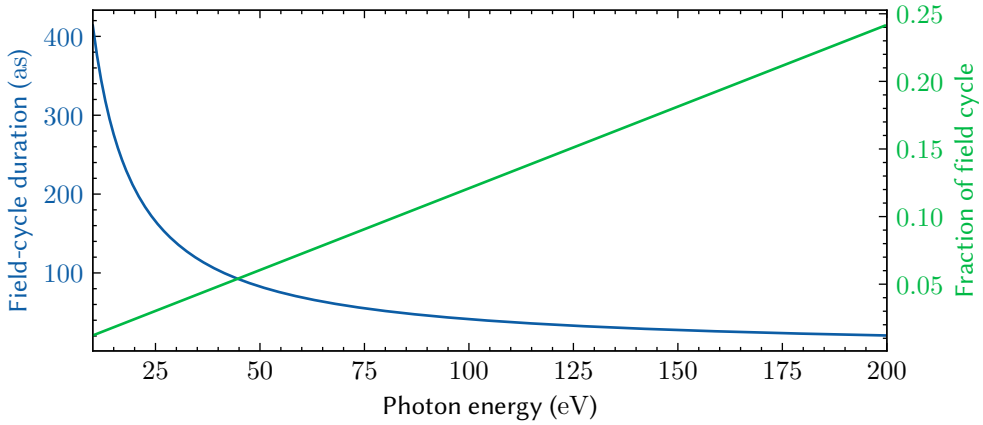

Figure 5.7.: Importance of attosecond precision. The blue curve plots the duration of a single field cycle as a function of XUV photon energy and the green curve shows what fraction of a field cycle 5 as correspond to.

5.5. Outlook

To substantiate the claims made in the discussion above, this outlook turns to two theoretical scenarios depicted in figure 5.8 which have not been experimentally realized yet. The goal here is to theorize the outcome of experimental schemes, where the buildup of ions through strong-field ionization and its sub-cycle modulation can be used to extract dynamics of the system.

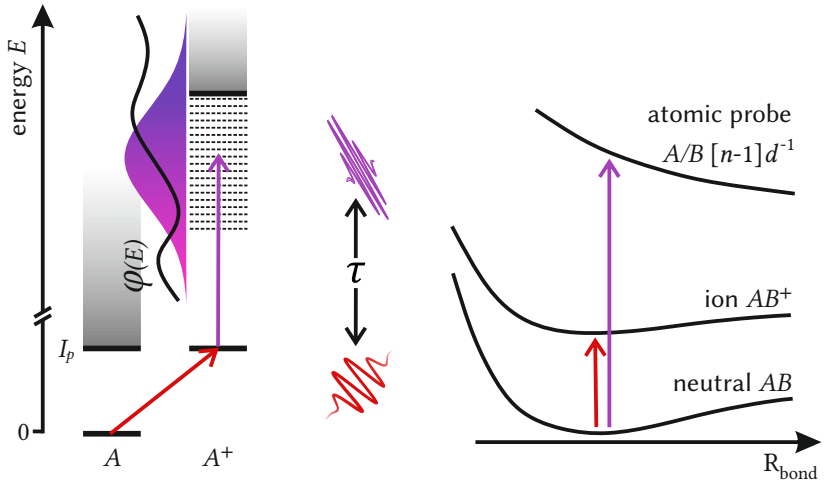

Figure 5.8.: Proposed measurement schemes. (left) Temporal buildup of SFI-induced transparency: ionization of the neutral species $A \longrightarrow A^+$ can lead to a sudden reduction in continuum absorption. The temporal structure of this change might be used to retrieve the spectral and dipole phases. (right) Molecular buildup dynamics: in the strong-field ionization of molecules the site-specificity of atomic core-to-valence transitions could be used to probe ultrafast charge-distribution dynamics.

Strong-field-ionization-induced transparency

The first idea builds on the sudden change in the XUV absorption cross section of atoms upon ionization. With one electron removed, the remaining ones become more strongly bound to the core and as a result the threshold for the next ionization step moves to higher energy. In helium the scenario is most extreme: after the ionization of the first electron, the ionization potential moves from 24.59 eV to 54.42 eV. Probing this ionization event by a time-delayed XUV pulse in this spectral region would lead to an increased transparency of the target, because the continuum absorption of the neutral target above the threshold is no longer present. Scanning the delay, the decrease in absorbance should be inversely-proportional to the buildup in ion population and lead to temporally modulated structures which in this case span across the whole spectral range of the continuum absorption. While the observation of a broadly modulated continuum alone would be a large success, we take the gedankenexperiment further by applying the method presented in this chapter. By examining the energy-dependent phase $\varphi(E)$ of the time-delay-resolved modulation, the sum of the spectral phase of the XUV probe pulse and the bound-continuum dipole phase could be read out over a wide spectral range. Disentangling both could be achieved by either measuring the spectral phase of the XUV pulses by using an established photoelectron method such as the streaking setup presented in section 3.3 or by calculating the phases of the dipole-matrix elements from *ab initio* theory as is routinely done in the photoelectron community.

For two reasons helium would be an ideal target for such an experiment. Firstly, the increase in ionization potential that can be reached via the ionization of a single valence electron is largest for helium. Secondly, helium is the best studied multi-electron system, which would facilitate the theoretical treatment. For other systems, such as neon and argon, the same rationale applies. Furthermore, the next ionization step from the singly- to the doubly-charged ion can be chosen for the same effect [12]. With even larger atoms, the change becomes more subtle and thus more challenging in the detection. Between Xe^{+} and Xe^{2+} there is virtually no difference in the continuum cross-section and for Xe^{3+} it is only a few megabarn (Mb) lower. A good collection of continuum cross-sections of atoms and their isonuclear sequences is compiled in [102].

The experimental challenge lies in the trade-off between the feasibility of the SFI step and the sensitivity in absorbance. Otherwise, the measurement consists of scanning only a small time-delay range around the temporal pulse overlap as often as possible. Due to its great single-shot sensitivity, the *in situ* reference method (section 3.2.3) is expected to prove useful although it is not strictly a prerequisite. In the first trials of precursor experiments in our laboratory, strong-field ionization of anything but xenon has not succeeded to produce sufficient yield to observe ionic transition lines, while generating XUV emission in the spectral region of interest at the same time. With the co-linear beam geometry of the setup, high target intensities needed for SFI are only possible when the intensity of the HHG driving pulses is high as well. As a consequence, the harmonics needed to be generated in neon, which in turn leads to insufficient HHG yield at lower ($< 40\,\mathrm{eV}$) photon energies. Using another generation medium results in significant ionization of the HHG gas, which in turn deteriorates the laser focus via plasma defocusing and thus the intensity in the target cell. Using the external incoupling (section 3.2.2), the HHG and target foci are independent, but it is questionable whether the required on-target intensities can be reached[1]. On top, without active stabilization the temporal resolution of the external interferometer is currently insufficient to resolve half-cycle oscillations.

Molecular ionization dynamics

A second idea, would be to extend the investigation of SFI dynamics to molecules. The halogens are promising targets for ATAS due to suitable XUV probe transitions from a core-d to the unfilled valence-p shell ($[n-1]d \longrightarrow np$). Interesting studies on coherent vibrational dynamics and valence-electron dynamics have been performed e.g. on the bromine molecule (Br_2)[193], iodomethane (CH_3I)[194] and iodine monobromide (IBr)[43]. The key feature of ATAS in this kind of studies is the site-specificity of the probe transitions. While chemical bonds are dominated by delocalized valence electrons, site-selective excitation can be used to track ultrafast charge migration. The SFI of a molecule is visible in the typical signals such as *excited state absorption* and *ground state*

[1] I might have to leave it to my colleagues Magunia et al. [192] and their 20 mJ laser system to experimentally pursue this idea.

bleach. In the former, non-adiabatic distortion of the electron binding potentials involves couplings to excited states, while in the latter the depletion of the ground state is a direct consequence of the ionization.

As was discussed in the results section, tracking the phase of just one signal transition would be meaningless without a reference. Therefore, heteronuclear molecules like IBr, where different transitions on both sites can be captured within the same HHG spectrum, could be a perfect target in the investigation of attosecond delays between the ion buildup signals of the two species. In addition strong-field ionization is known to be able to prepare wave packets in atomic [24; 40; 188] and molecular [195] ions by populating not only the ionic ground state, but excited states as well. Thus, a possible application of the method developed in this chapter would be to monitor charge migration due to the dynamics of the valence electrons by studying the delays in XUV excitation from the different sites in the molecule.

6. Strong-field ionization dynamics of a multi-electron system

Symmetric Lorentzian and asymmetric Fano absorption line shapes can both be observed in nature outside the context of time-resolved spectroscopy. Nevertheless, they are intrinsically linked to the time domain as the spectral signature from the decaying dipole radiation that can be emitted when a quantum system is excited by light. With ultrashort and strong laser pulses both amplitude and phase of the dipole radiation can be modified by controlling the quantum system at scrutiny, which results in spectral lineshape changes experimentally observed by attosecond transient absorption spectroscopy (ATAS). Phenomena such as resonant couplings between states [13; 196], quantum beats [40; 188], light induced states (LIS) [191], Autler-Townes splitting [197–199], ionization [45] and Stark shifts [99] all leave distinct imprints on the dipole radiation and result in a variety of line shapes that do not necessarily classify as either Lorentzian or Fano.

Since the dipole moment we measure by assessing the absorption line shape is basically an overlap integral between the wave functions of the excited states with the ground state, the signal is susceptible to changes directly within the atom/molecule and unaffected by long-range effects that disturb potentially outgoing electrons. At the same time the method is not restricted to weak perturbations of the system of study (see section 2.4.2). Here, we explore these possibilities to the extreme by studying the line shapes of resonant transitions in xenon ions amid their formation through strong-field ionization. The findings are analyzed in the light of the Fano picture (section 2.3.2) and model simulations hint at the transient, sub-cycle modulation of the configuration interaction between the fine-structure components of the excited states.

The number of studies that use ATAS to investigate ion dynamics is relatively limited. This might be attributed to the need of a state-of-the-art, high-power, few-cycle laser system that can both generate high-harmonics and use the remaining laser light to strong-field ionize atoms in the target. The investigations that exist are mostly focused around the extraction of ion populations and coherences [24; 39–42; 57; 188; 200]. Since only one theoretical study [91] and no experimental study performing a line-shape analysis of ions exists and because we have the chance to use intensity as a complementary control parameter our experimental undertaking is clearly needed and justified.

6.1. Experimental methods

In the experiments presented in this chapter, the intensity of the near-infrared (NIR) pump pulses was the main control parameter. The range that could be scanned before ionization in a pre-pulse started to become significant was $1–2.5 \cdot 10^{14}$ W/cm^2 as the eval-

uation presented in figure 4.9 shows. The *in situ* reference could not be used in this measurement as the pellicle filters mounted on the same stack as the TEM grids burned after a few hours. Needless to say that this never happened before, but then again, we had not performed experiments at these intensities. To overcome this challenge a Kapton filter that had been mounted as well was switched in and withstood the high intensities. It should be noted that the relatively new, doubly differentially pumped hollow-core fiber presented in section 3.1.1 was essential to deliver the full power of the laser amplifier to the beamline while maintaining a stable beam mode. The measurement consists of 36 time-delay scans for each of the 11 iris positions that set the NIR intensity, which were averaged to obtain a high signal-to-noise ratio for the line-shape analysis. A range of −7.2 to 18.5 fs around the temporal overlap of the XUV and NIR pulses was covered with a delay resolution of 85 as which allows to fully trace the buildup of the xenon ion population. To compute ΔODs, the acquisition of absorption spectra alternated between the time-delay position of interest and a reference position at $\tau = -17$ fs as described in section 4.3.

6.2. Line-shape fits

In order to extract information from the measurement data, the line-shape model introduced in section 2.4.5 is used to perform a fit to the absorption lines. It was derived on the basis of the dipole-control model for a decaying dipole subjected to an impulsive phase kick and yields a line shape that corresponds to a generalized absorption profile parametrized as a function of the phase shift ϕ:

$$\mathrm{OD}(\omega,\tau) = \frac{(\varrho L)_{\mathrm{a.u.}}}{\ln(10)}\, 4\pi\alpha\omega \sum_{\mathrm{T}} z_0(\tau) \frac{\Gamma(\tau)/2\cos(\phi(\tau)) + (\omega-\omega_{\mathrm{T}})\sin(\phi(\tau))}{(\omega-\omega_{\mathrm{T}})^2 + \Gamma(\tau)^2/4} + C(\tau). \tag{6.1}$$

This model was first presented by Pabst et al. [91] and used in the analysis of Sabbar et al. [57]. It is used to directly fit the experimentally observed optical density as a function of the photon energy $\hbar\omega$ for every time delay τ. The sum runs over all transitions T, which are added up incoherently in this model. The model can be used to describe asymmetric line shapes and the phase shift ϕ is connected to the Fano asymmetry parameter q via $\phi = 2\arg q$. For $\phi = 0$ it describes a symmetric Lorentzian profile. There are three possible, time-delay dependent fit parameters for each absorption line; the amplitude/line strength z_0, phase ϕ and linewidth Γ. Due to different signal-to-noise ratios (SNRs) of the different lines, not all parameters were taken into account for every absorption line. Table 6.1 shows, which parameters were used for each resonance. This way, the fit results for each spectrum at a time-delay position τ could be optimized without overfitting. Wherever the phase is not ticked off it was set to zero, which corresponds to a Lorentzian line shape. Where the linewidth is left unchecked, the literature value of $\Gamma = 122$ meV and 92 meV [110] is used for the transitions in Xe^+ and Xe^{2+}, respectively. Additionally, a constant time-delay-dependent offset $C(\tau)$ is used to account for background absorption.

An example of an experimental time-delay scan and its reconstruction from the fit of the model are shown in figure 6.1 and demonstrates the good agreement between the data and the model fit. The prefactor in equation 6.1 serves to scale the overall amplitude.

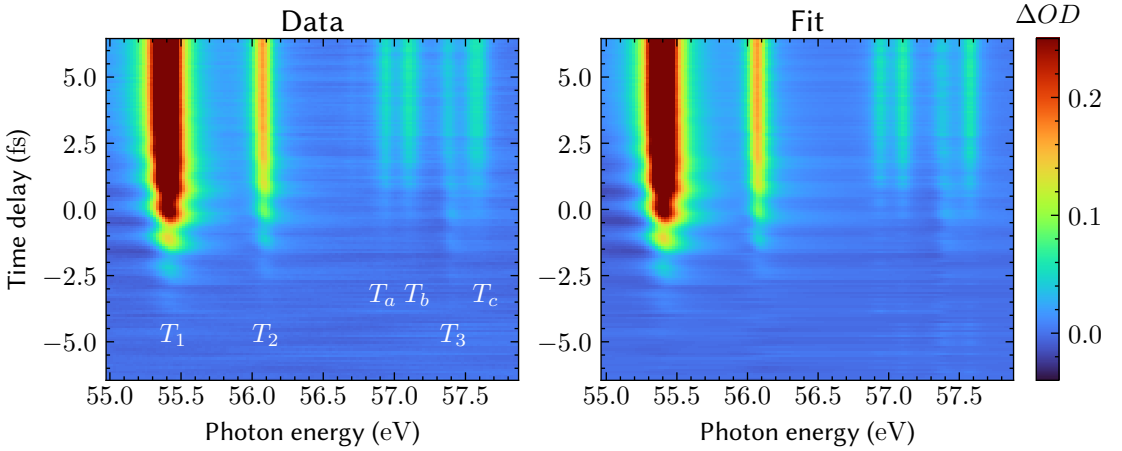

Figure 6.1.: Experimental data (left) and reconstructed spectra from line-shape fits (right). This scan was recorded at an NIR intensity of $2.3 \cdot 10^{14}\,\mathrm{W/cm^2}$. The color scale was set to focus on the weak details such that the strongest absorption line T_1 appears saturated.

transition		1	2	3	a	b	c
energy (eV)	$\hbar\omega_T$	55.39	56.08	57.37	56.94	57.11	57.57
amplitude	z_0	✓	✓	✓	✓	✓	✓
phase	ϕ	✓	✓	✓			
linewidth	Γ	✓	✓				

Table 6.1.: Overview of the fit parameters for each individual absorption line. The labels correspond to the transitions $T_i, i \in \{1, 2, 3, a, b, c\}$ according to figure 4.1, where the number or letters indicate transitions in Xe^+ and Xe^{2+}, respectively. A time-delay-dependent offset was included as an additional fit parameter. The resonance energies are fixed and were taken from synchrotron measurements [110].

Here, $\alpha \approx 1/137$ is the fine-structure constant and ϱL is the path-length-density-product estimated in section 4.3.4. In the fits, ϱL is held constant at the value obtained at positive time delays for the highest NIR intensity such that amplitude modifications are fully captured by the parameter z_0. The line strength captured by this parameter is proportional to the effective valence-hole population P_{eff} and the dipole transition matrix element d_{T_i} of every transition:

$$z_0 \propto P_{\mathrm{eff}} |d_{T_i}|^2. \tag{6.2}$$

It can therefore be used to extract direct information of the ion population, which shows overshoots due to reversible polarization dynamics during the buildup (section 2.2.2, [57]). The fit results for the Xe^+ transitions T_1, T_2 and T_3 are shown in figure 6.2. In each

panel, the color coded plots indicate the fit result for a certain intensity as a function of the time delay τ. The intensity of the pump pulse increases quasi-linearly from the blue to the red curve and covers a range of $1–2.5 \cdot 10^{14}\,\mathrm{W/cm^2}$ (compare section 4.3.3). Due to the vanishing amplitude of the absorption lines when the probe pulse precedes the pump, the fits become increasingly unreliable for negative time delays. To enhance the presentation of the results this characteristic is encoded as an increased transparency of the curves which is inversely proportional to the amplitude parameter, instead of overcrowding the figure with additional error bars.

While figure 6.2 contains a lot of information, some observations can be made directly. Just from the line strengths we note the following:

- The overshoots in the buildup of the ion population are reproduced and in agreement with a related study Sabbar et al. [57].
- The ionization moves towards the leading edge of the pulse at increasingly negative time delays for higher intensities as expected (compare with figure 2.3).
- The single ionization of xenon saturates. For the highest intensity, the population even decreases again, as double ionization starts to set in.
- A pre-pulse out of the time-delay range covered by the experiment is strong enough to contribute to the ionization at the highest intensity.

The linewidth was introduced as a fit parameter, because the strongest absorption line T_1 showed noticeable broadening and a poor reconstruction of the aforementioned overshoots of the line strength without the variable linewidth. It was in the fitting of T_1 and T_2 to trace the physical origin of the line broadening and because the SNR of both lines allowed it. The fit results show a clear intensity dependent broadening of T_1, but no influence (above the noise level) on T_2. The delay-dependent increase towards negative time delays means that the broadening is a result of the suppression of the dipole emission through the NIR acting after the XUV excitation. Because T_2 remains unaffected a tentative interpretation of the observed broadening is the exclusive ionization of the excited state configuration of T_1, which is $4d^{-1}\,{}^2D_{5/2}$. The corresponding configuration of T_2, $4d^{-1}\,{}^2D_{3/2}$ lies 1.96 eV higher in energy but is seemingly unaffected, which suggest that not purely field-driven tunneling but resonant enhanced multi-photon ionization plays a role here.

The most remarkable observation from the line-shape fits is the course of the phase evolution, which similarly to the line strength shows half-cycle oscillations on top of a general trend. In addition, the oscillation amplitude is intensity-dependent and decreases for higher intensities. The latter is unexpected, because most effects scale proportionally and not inversely with intensity. The greater part of the remainder of this chapter is devoted to uncover the origin of the observed phase evolution.

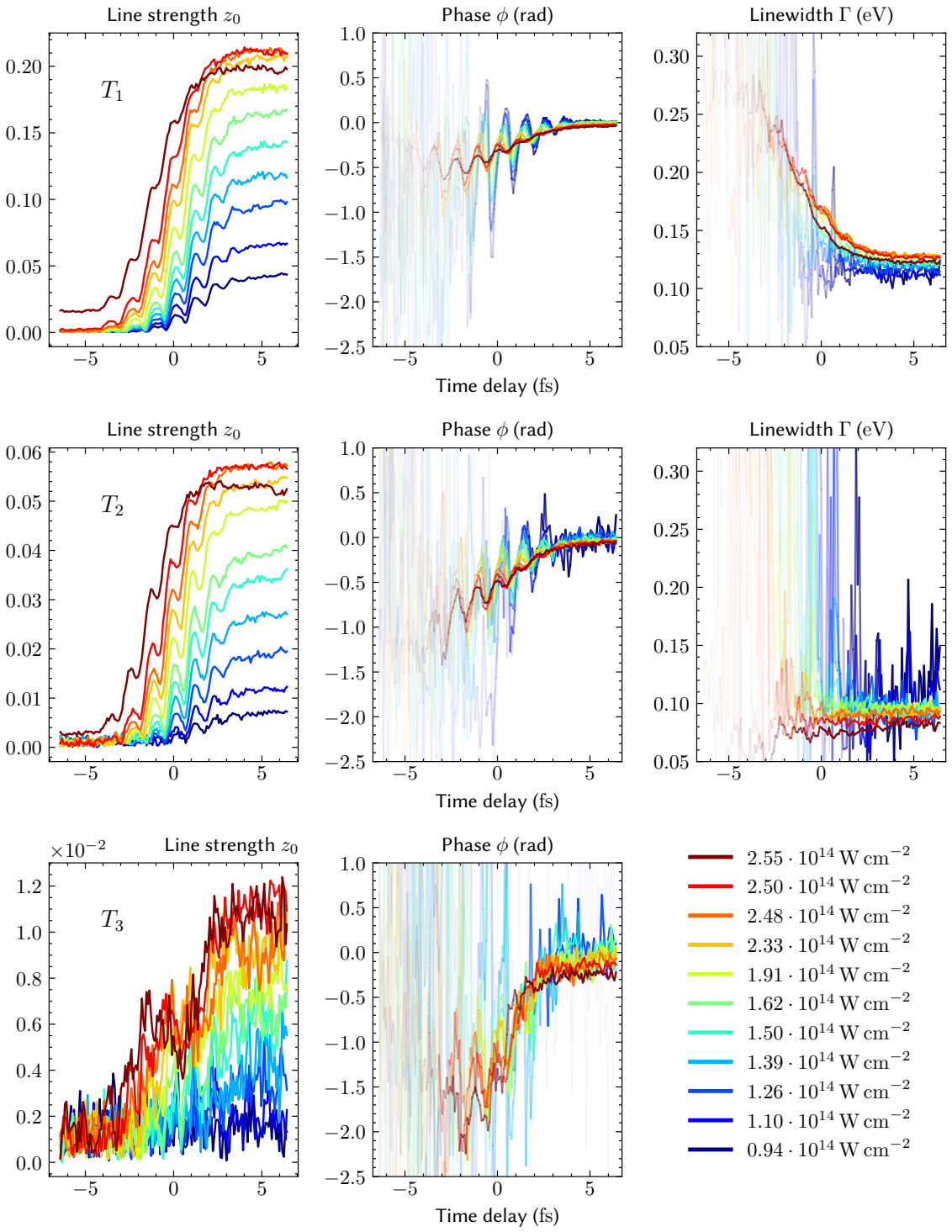

Figure 6.2.: Fit results for the resonance lines T_1, T_2 and T_3 (top to bottom) as a function of time delay. The intensity of the NIR pump pulse is encoded in the color of the different lines and increases from blue to red. For negative time delays the signal is weak and thus the results for the phase and linewidth become unreliable. This is reflected in an increased transparency of these parameters.

6.3. The time-dependent dipole

Extracting information from the experimental data by fitting has advantages and disadvantages. The main benefit is the direct access to physically comprehensible parameters, while relying on a specific fit model can be a major drawback. Together with experimental noise and possible artifacts from the ΔOD reconstruction, the limits of the model lead to small discrepancies that can be observed by comparing OD spectra with their corresponding fits as shown in figure 6.3.

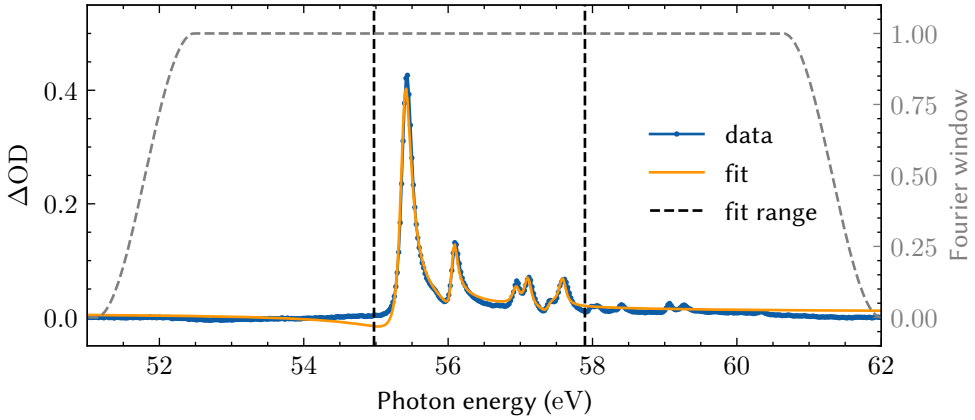

Figure 6.3.: Discrepancy between the fit and the experimental data illustrated by an exemplary spectrum from the time-overlap region. The vertical lines indicate the spectral range used for the fit. The grey cosine window is used in the reconstruction of the time-dependent dipole moment.

To validate the findings obtained through the fit results, a complementary analysis based on the investigation of the time-dependent dipole moment (TDDM) is conducted in the following. Through this technique, presented in section 2.4.4, the measured optical densities can be inverted to obtain the TDDM as a function of its real time of evolution via Fourier transformation. The cosine window used to filter the spectral range subjected to the Fourier transformation is shown in figure 6.3 and was chosen broad enough to sample the dipole moment with a resolution better than 0.5 fs. Direct application on the measurement results yields figure 6.4, where the amplitudes of the decaying dipoles are shown as a function of time delay. The two time axes are shown with equal aspect ratio, to highlight the changes imprinted by the NIR pulse. Because the source of the dipole emission is the excitation through the attosecond XUV pulse, in the conventional representation of the time-delay axis the NIR would arrive after the XUV pulse for positive delays, such that the center of the NIR can be traced as diagonal with slope one. Here, the NIR pulse defines delay zero instead and the delay indicates the relative timing of the XUV pulse, since this is a better representation of the common pump-probe picture, where the NIR is critical to create the ion population. As a result the excitation by the XUV pulse follows a diagonal with slope minus one, which is indicated by the dashed

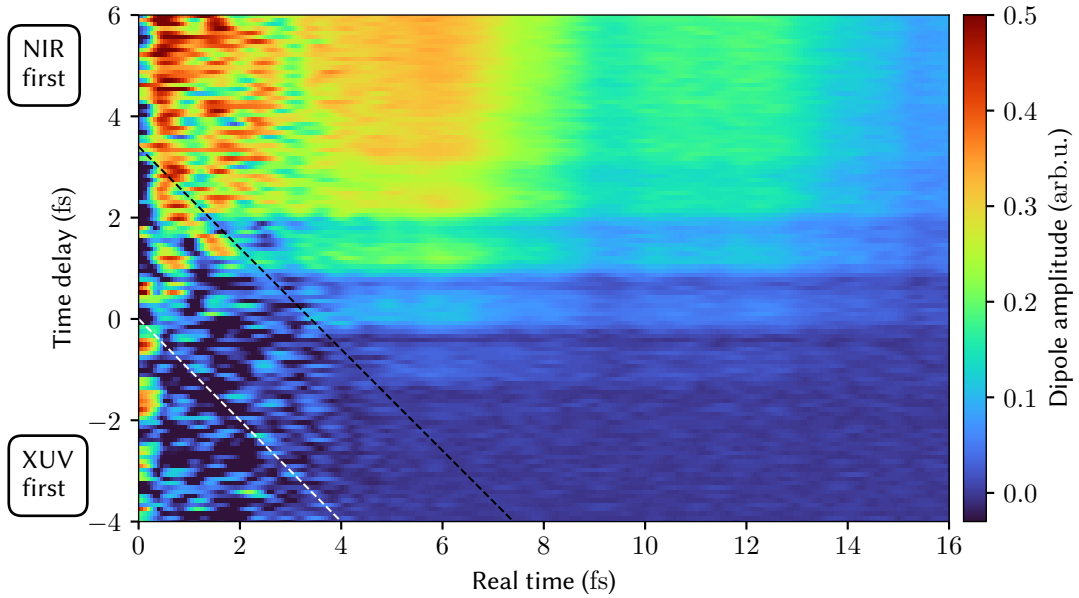

Figure 6.4.: Amplitude of the time-dependent dipole moment retrieved from the experimental data recorded at $10^{14}\,\mathrm{W/cm^2}$ as a function of the 'real time' of evolution and time delay. The dashed lines are guides to the eye to highlight the effect of the NIR pulses.

lines in figure 6.4. The probing of the ions after their generation clearly follows the black dashed line, which is offset from the white line at $\tau = 0$ because the absolute setting of the delay was fixed for a scan at a higher intensity. There the buildup amplitude is larger but shifted towards negative delays because saturation effects lead to ionization earlier in the NIR pulse. Tracking the dipole buildup becomes increasingly difficult at negative delays, because there is not yet any ion population to be probed by the XUV pulses once the pulses leave temporal overlap. Unfortunately, it is hard to track the evolution of the dipole moment right after the excitation, because of the noise for 'real times' < 5 fs which stems from slow background oscillations on the spectra that remain from the calculation of the ΔOD with imperfect references. Still, an imprint of the interplay between the two pulses can be distinguished from the noise due to its characteristic slope.

6.3.1. The laser controlled dipole

With the dipole reconstruction method, we can access the dipole moment and its real-time evolution. But how can we get a hold on the perturbation through the NIR pulses? Using suitable references that are free from the perturbation of the laser pulses, the modification of the dipole amplitudes and phases can be isolated. Here, the reference dipole responses for the scans at different intensities are calculated by averaging over the time-delay region 5.7–18.5 fs, where the two pulses are out of overlap, meaning that the ions are probed long after the SFI. Dividing each TDDM by this reference, we can

separate the modification caused by the NIR pulses on both amplitudes and phases at each intensity as shown exemplarily in figure 6.5. The amplitude modifications show

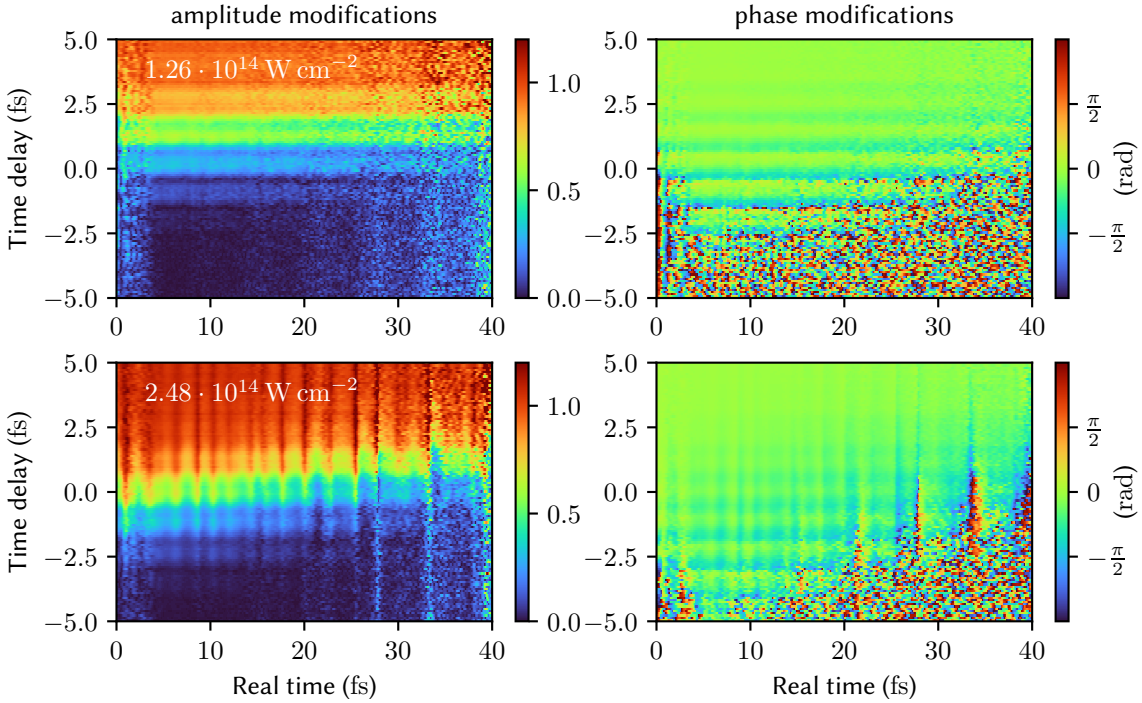

Figure 6.5.: NIR controlled modifications of the dipole amplitudes (left) and phases (right) at low (top) and high (bottom) intensity. At low intensities the real-time evolution is flat because only Xe^+ absorption lines are visible. At higher intensities, the TDDM reference averaged over late delays contains also the Xe^{2+} resonances, which generates a beating of the dipole amplitude in the time overlap, where the Xe^+ lines dominate.

the NIR-induced buildup along the time delay in a complementary picture. When the buildup of all resonances is synchronous, no modification along the real-time axis is observed. At higher intensities, where the Xe^{2+} ions are produced with a delay with respect to Xe^+ , this manifests as a real-time beating of the amplitude modifications, because the reference encompasses all resonances, whereas the spectra may only contain contributions from the singly-ionized species. Noise dominates the reconstructed dipoles both for real times $t \lesssim 4\,\mathrm{fs}$ and delays $\tau \lesssim -4\,\mathrm{fs}$, because of residual broad spectral fluctuations in the spectra and low amplitudes of the absorption lines, respectively.

For the phase modifications the general trend is similar. All features apart from noise are flat for all real times and for the high intensities, some modulation is present due to the presence of the Xe^{2+} lines. A flat phase means that the NIR imprints an initial phase onto the transitions, which does not change after the excitation. This is exactly the assumption that the fit model makes, which explains its success and serves as a retrospective justification. Motivated through this observation, we focus on small 'real times'

$t < 26\,\mathrm{fs}$, which is the time span that contains > 90% of the dipole amplitude and contains the least amount of noise. Averaging over this time span yields the equivalent to the impulsive phase kick from the fit model, both of which are compared in figure 6.6. The similarity is remarkable and both, the phase oscillations with their intensity dependence and the general trend of the curves are reproduced. The difference between the two methods is that while the fits can assume a different phase for every transition, here, one phase is extracted for the whole dipole response. In principle the phase of each transition could be extracted by using a spectral window around each resonance. Since the phase oscillations found in the fits are synchronous, this approach is not necessary. In addition it was checked that the Xe^{2+} lines make no significant contribution to the phase. The bottom line of this investigation is that the line-shape modifications in the time overlap region are well described by an instantaneous phase shift ϕ occurring at the time of the dipoles' excitation. Next we turn to explain the physical origin of this phase shift.

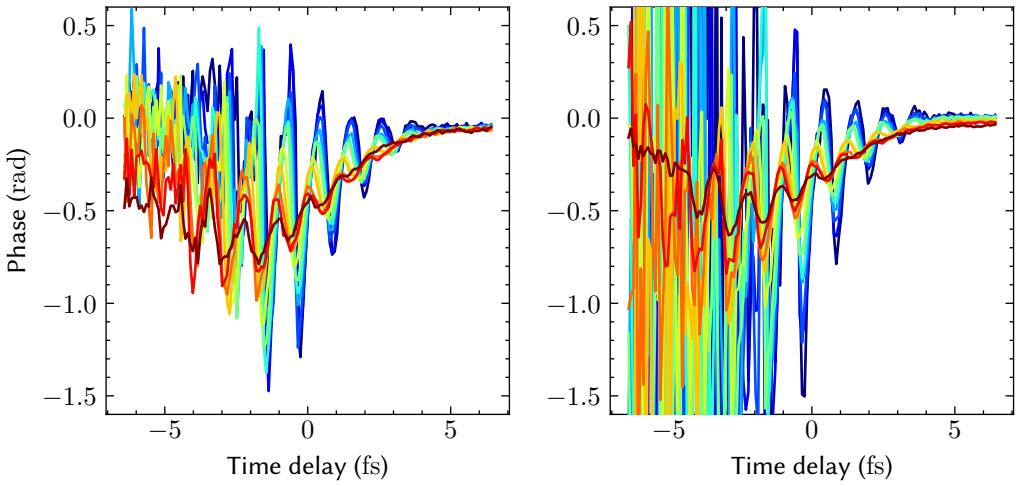

Figure 6.6.: Extraction of impulsive phases. The real-time-averaged phases of the temporal dipole moment (left) next to the impulsive phases extracted from the fits to T_1 using model function 6.1 (right).

6.4. Initial Fano phases

With the XUV excitation energies considered here, xenon—with even its 4^{th} ionization threshold at just $I_p^{4+} = 42.2\,\mathrm{eV}$—is highly excited. Consequently, the transitions that we observe are autoionizing (via Auger decay). At the same time, the target is irradiated with pulses that strongly modify the atomic potential, which is clear since the xenon atoms are ionized not only once, but even twice at the higher intensities. It is thus reasonable to expect that the eigenstates that would define the evolution of the system in the field-free scenario are perturbed in the process. After all, the overshoots in the

buildup of the ion population are a result of the laser-induced polarization [57] of the atoms. In a first attempt to shed light onto the dynamics in this non-equilibrium system that lead to the oscillations in the phase evolution, this section starts by discussing the impact of the Stark effect on absorption line shapes. It then turns to the investigation of a time-dependent Fano model, which was solved numerically in few-level simulations[1] to develop an intuitive understanding of the process that leads to the phase shifts/ line-shape asymmetries.

6.4.1. Stark shifts

Among strong-field phenomena, a prominent candidate that is known to affect the phase of quantum states is the Stark effect (section 2.2.1). While the pulse is present, it leads to an energy shift ΔE_{Stark} and thereby to a modification in the natural phase evolution $e^{(-iEt)}$ of any state. In general it can be assumed that both the ground and excited state of a transition are shifted and contribute to the phase shift according to their polarizability α, such that only the difference $\Delta\alpha = \alpha_g - \alpha_e$ in their polarizabilities matters. The phase shift can be calculated analytically by scanning the time delay of a δ-like XUV pulse and integrating over the remainder of the NIR pulse, since shifts before the excitation do not contribute:

$$\Delta\phi(\tau) = -\frac{\Delta\alpha}{4}\int_{\tau}^{\infty} \mathrm{d}t\mathcal{F}_{NIR}(t)^2, \tag{6.3}$$

with the pulse envelope $\mathcal{F}_{NIR}(t)$. Thus, $\Delta\phi(\tau)$ is large for negative delays τ and decreases as the XUV pulse passes to the front of the NIR pulse. The central observation is that a phase shift due to the Stark effect can only increase monotonically, because the squared envelope is positive at all times. The same is true when the envelope of the pulse is replaced with the electric field itself, i.e., in the case of an sub-cycle AC-Stark effect [71]. Although the phase shift is made up of half-cycle steps in this case, it remains strictly increasing. An illustration of the phase shift as a function of time delay is shown in figure 6.7. So even though the polarizability of xenon is relatively large with $\approx$ 27 a.u. [75], the Stark effect cannot account for the observed phase oscillations, at the most for a general trend of the phase.

6.4.2. Time-dependent Fano coupling

In the static picture, the asymmetry of a resonance is a characteristic of a bound state degenerate with and coupled to a continuum of free states. Its theoretical explanation was pioneered by Ugo Fano [94; 96] and boils down to the parametrization of the asymmetry

[1] The effect of transient Stark shifts of the energy levels in a model system was simulated as well, but the analytical approach offers the same results in a more intuitive picture.

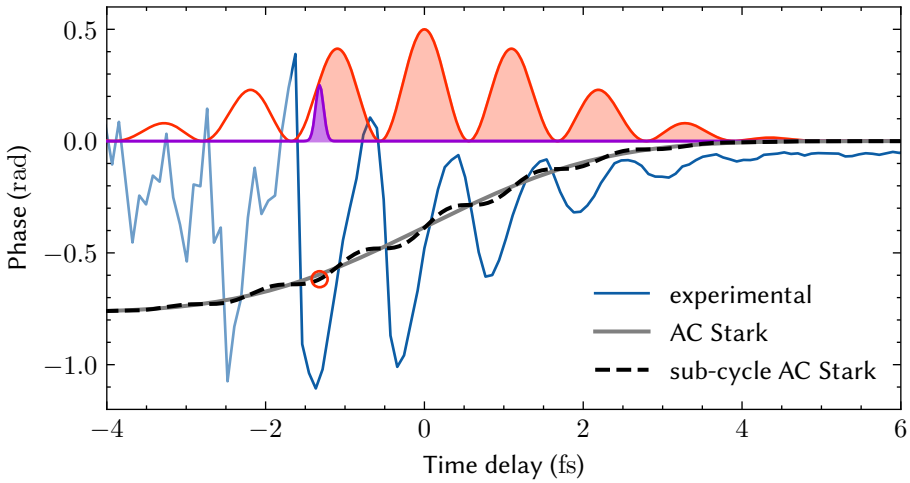

Figure 6.7.: Illustration of the phase shifts induced by an AC or sub-cycle AC Stark effect side-by-side with an exemplary phase evolution extracted from the measurement. The red circle demonstrates how the phase is obtained by integrating over the shaded area under the squared electric-field as a function of the delay of the XUV pulse.

through the q-parameter (section 2.3.2):

$$q = \frac{\langle e|\hat{\boldsymbol{d}}|g\rangle}{\pi V_{ci}^{*}\langle c_E|\hat{\boldsymbol{d}}|g\rangle} = \frac{d_{ge}}{\pi V_{ci}^{*} d_{gc}} \tag{6.4}$$

where $|e\rangle$ is a bound, excited state degenerate and coupled to the continuum states $|c_E\rangle$ via the configuration interaction matrix element V_{ci}; d_{ge} and d_{gc} are the respective dipole matrix elements between these states and the ground state $|g\rangle$.

This formulation of the asymmetry motivates to account for the strong dressing of the system by imposing a modulation of the matrix elements that define the couplings in equation 6.4 as functions of the NIR electric field $F_{NIR}(t)$:

$$\begin{aligned} d_{ge} &\longrightarrow d_{ge}(t) = d_{ge}(1 \pm (\tilde{d}_{ge}|F_{\mathrm{NIR}}(t)|)^n), \\ d_{gc} &\longrightarrow d_{gc}(t) = d_{gc}(1 \pm (\tilde{d}_{ce}|F_{\mathrm{NIR}}(t)|)^n), \\ V_{ci} &\longrightarrow V_{ci}(t) = V_{ci}(1 \pm (\widetilde{V}_{ci}|F_{\mathrm{NIR}}(t)|)^n), \end{aligned} \tag{6.5}$$

where the nonlinearity parameter n can be used to shape the impact of the field. It is set to $n = 2$ and has no influence on the generality of the results. Assuming the modulation of the dipole matrix elements is a valid representation of the dynamics of the system, it can be expected to translate into a NIR-dependent Fano-q-parameter and thus to a variation of the initial phase kick ϕ of the dipole moment.

The modulation of each coupling can be motivated on an individual basis. For the dipole matrix element from the ground to the excited state, the polarization of the neutral ground state can be expected to play an important role. Since the transitions of

interest are resonances in singly ionized xenon, the ionic ground state has to be prepared by the NIR pulses through SFI. While this happens, neutral excited states can be transiently populated as well which opens up the excitation channel for a $4d$-core electron to be excited into the valence-hole only while the NIR perturbs the system. The continuum absorption is enhanced through the lowering of the potential barrier every half-cycle of the field, which makes direct ionization possible with XUV photons with lower photon energies and leads to a net increase in the continuum channels that are accessible with a given XUV pulse. Finally, a temporal variation of the configuration interaction is conceivable as an opening of additional decay channels of the excited state. Such laser-enabled Auger decays (LEAD) [201; 202] can open ionization channels that would be energetically forbidden without the presence of the NIR field [203], which is the same effect as enhancing the coupling between the excited state and the continuum states.

From the ideas formulated so far, a few-level model of a prototypical Fano system consisting of a ground state $|g\rangle$, an excited state $|e\rangle$ and a continuum state $|c\rangle$, which is degenerate with the latter, is set up. Without the time-dependent couplings, the time-dependent Schrödinger equation for the state coefficients $c(t)$ of the model reads:

$$\mathrm{i}\frac{\partial}{\partial t}\begin{pmatrix} c_g \\ c_e \\ c_c \end{pmatrix} = \begin{pmatrix} E_g & d_{ge}F_{XUV}(t) & d_{gc}F_{XUV}(t) \\ d_{ge}^{*}F_{XUV}(t) & E_e & V_{ci} \\ d_{gc}^{*}F_{XUV}(t) & V_{ci} & E_e - \mathrm{i}\,\Gamma_c/2 \end{pmatrix}\begin{pmatrix} c_g \\ c_e \\ c_c \end{pmatrix}. \tag{6.6}$$

The diagonal elements of the Hamiltonian above are the energies of the respective states, where the energy of the continuum state features a complex contribution in the form of the linewidth Γ_c. By means of this linewidth the continuum state is adjusted to decay rapidly such that it effectively acts as a loss channel. The excited states are excited from the ground state via the bound-bound and bound-continuum dipole matrix elements d_{ge} and d_{gc}, while the excited states themselves are coupled via configuration interaction in terms of the matrix element V_{ci}. The whole coupling scheme is depicted in figure 6.8. To gain insight into the dynamics of this model a few-level simulation following the split-step time-propagation algorithm introduced in section 2.3.1 was implemented. In the simulation the ionic ground state is populated according to ADK ionization rates, which takes into account depletion of the neutral population as described in section 2.2.2.

6.4.3. Few-level simulation

The few-level simulations we can solve ourselves cannot account for the distortion of the atomic potential directly, because they lack a spatial representation of the system. The approach taken here, to include the field-dependence as an aspect of the couplings among the atomic states, stems from the concept of the interaction picture, where in contrast to the Schrödinger picture part of the dynamics of the system is transferred from the wave function to the operators. The goal of these numerical studies is thus to learn about the model system by varying the free model parameters $\tilde{d}_{ge}$, $\tilde{d}_{gc}$ and $\tilde{V}_{ci}$.

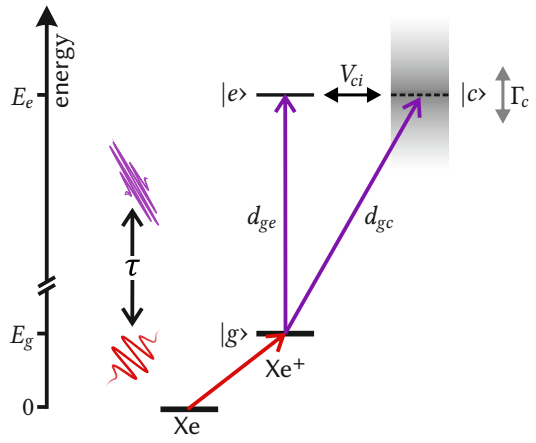

Figure 6.8.: Illustration of the levels and couplings in the model.

Numerical details

To obtain a model transition that aims to reproduce the experimentally measured transition T_1, the energy levels of the ground and excited states are set to $E_g = 12.13\,\text{eV}$ and $E_e = 67.52\,\text{eV}$, respectively. In principle it is the coupling to the continuum which defines the linewidth $\Gamma_e = 2\pi|V_{ci}|^2$, such that conversely, the literature value $\Gamma_e = 0.122\,\text{eV}$ is used to determine the configuration interaction, $\Longrightarrow V_{ci} = 0.027$ a.u.. To actually obtain the correct experimental linewidth Γ_e, the linewidth of the continuum state can be tuned and is set to $\Gamma_c = 17.5\,\text{eV}$, which corresponds to a decay time of $\tau_c \approx 37\,\text{as}$ and is sufficiently fast to prevent a return of population from the continuum back to the other two states. Finally, the ratio d_{ge}/d_{gc} was defined by imposing that the (NIR-) field-free Fano parameter of the resonance is $q > 100$, which results in a quasi-Lorentzian line shape[2]. This constraint is met by $d_{ge}/d_{gc} = 10$, while $d_{ge} = 0.115$ a.u. was chosen to obtain an optical density that is comparable to the experimental data ($\Longrightarrow d_{gc} = 0.0115$ a.u.).

The electric fields $F_{XUV}(t)$ and $F_{NIR}(t)$ in the simulation are defined as Fourier limited pulses with Gaussian envelopes of duration $\Delta t_{XUV} = 150\,\text{as}$ and $\Delta t_{NIR} = 5\,\text{fs}$ at central photon energies of $\hbar\omega_{XUV} = 56\,\text{eV}$ and $\hbar\omega_{NIR} = 1.85\,\text{eV}$, respectively. The latter is blue shifted[3] with respect to its standard value of $\hbar\omega_{NIR} = 1.65\,\text{eV}$ to match the frequency of the buildup oscillations. The peak field strength of the XUV pulse is $\mathcal{F}_{0,XUV} = 10^{-4}$ a.u. ($\Longrightarrow I_{0,XUV} = 3.5 \cdot 10^8\,\text{W/cm}^2$) and $\mathcal{F}_{0,NIR} \approx 0.053$ a.u. ($\Longrightarrow I_{0,NIR} = 1 \cdot 10^{14}\,\text{W/cm}^2$) for the NIR pulse.

[2] For comparison: the resonances of the $4d - np$ series in neutral xenon have $q \approx 200$ [115].
[3] An effect commonly observed in plasmas [182; 204] such as the partially ionized HHG and target gases.

The evolution of equation 6.6 is solved numerically by the split-step algorithm on a numerical time grid with length $T = 8550$ a.u. ≈ 200 fs and increment $\mathrm{d}t = 0.25$ a.u. ≈ 6 as, which is chosen to ensure an energy sampling of $\mathrm{d}E = 20$ meV up to an energy of 70 eV. Atomic units (appendix A.1) are used throughout the simulations as it simplifies the numerical treatment.

The objective of the simulation now is to track the evolution of the time-dependent, complex coefficients c_g, c_e and c_c of the model states from which the time-dependent dipole moment of the system can be calculated according to equation 2.35. The TDDM in turn serves to compute the optical density (equation 2.52) for a certain pulse configuration. Just as in the measurement, a complete time-delay scan is obtained by sequentially performing numerical experiments with different delays between the pulses, with the advantage that parallelization on several computer cores can run some of these simultaneously. From the simulation results, we can retrieve the phase of the dipole and thus the asymmetry of the line by using either of the approaches presented at the beginning of this chapter; fitting the ODs or extraction directly from the dipole moment. Because here the data is quasi noise free, the latter approach is preferred for speed and because it avoids the limitations of the fit model.

Simulation results

To get a first impression of the results of the simulations, figure 6.9 shows the experimental ΔODs of a time-delay scan along with the optical densities obtained by introducing each of the three model parameters $\tilde{d}_{ge}$, $\tilde{d}_{gc}$ and $\widetilde{V}_{ci}$ individually while leaving the other two fixed at zero. Each parameter leads to a characteristic effect on the simulated ion line, which will be briefly discussed. The modification of the bound-bound dipole matrix element $\tilde{d}_{ge}$ introduces an overshoot in the buildup as the XUV pulse scans over the field maxima of the NIR. Given the structure of the model this is a straightforward consequence of the periodic enhancement of the coupling constant that defines the transition strength of the resonance. No notable asymmetry is introduced through this effect, but within the constraints of the model it can be considered as a candidate for the origin of the overshoots observed in the experimental buildup of the ion lines.

The second modified dipole coupling to the continuum state $\tilde{d}_{gc}$ already offers a much more interesting structure. Here, a clear asymmetry on the model resonance is observed without affecting the strength of the transition as strongly as the previous parameter, which is possible since it only affects the excited state $|e\rangle$ indirectly through the coupling with the continuum state $|c\rangle$ via configuration interaction, which is constant here.

At last, the time-dependent configuration interaction suppresses the line in a modulated manner as can be expected by periodically increasing the coupling strength to the loss channel which the continuum state presents. Again, no clear deviation from a symmetric line shape can be made out for this parameter. To study the asymmetry of the line in detail, the next step in the analysis is to focus on the phase shift each model parameter

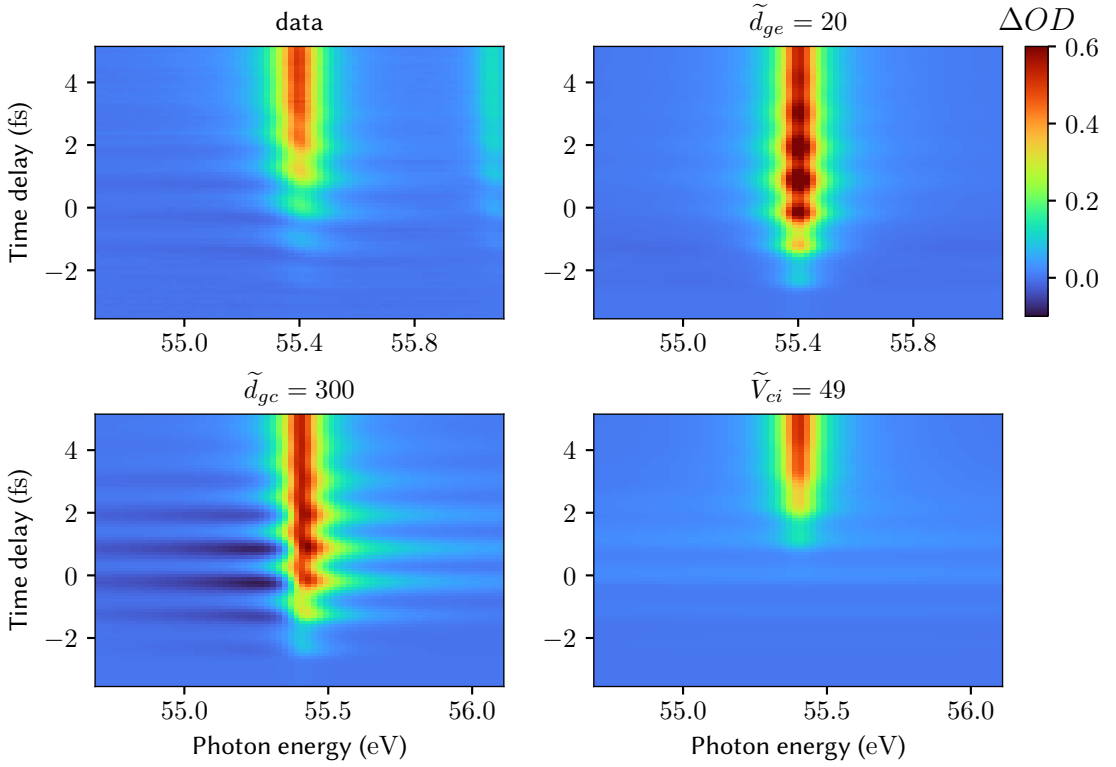

Figure 6.9.: Comparison between the measured optical density of resonance T_1 and the simulation results for each of the free model parameters. The respective other parameters are set to zero.

imprints onto the dipole moment. Before proceeding to do so, it can be noted that any modification of the configuration interaction of $\widetilde{V}_{ci} \gtrapprox 49$ results in a nonsensical phase, since the dipole moment is largely suppressed to zero.

Figure 6.10 serves to analyze the phase changes introduced by the model parameters. Here, it can be seen that $\widetilde{V}_{ci}$ actually introduces a phase shift, but on a smaller scale than $\widetilde{d}_{gc}$. In addition, the suppression of the dipole moment's amplitude is already close to the limit for those values where the associated phase would start to matter. As was already noted above, $\widetilde{d}_{ge}$ really does not introduce any asymmetry on the line shape that was conceivable above the noise level in the phase analysis. It was therefore left out of the plot. Confirming the observation made by examining the optical densities, $\widetilde{d}_{gc}$ introduces half-cycle phase oscillations on the same order of magnitude seen in the experiment which can be scaled to reach the amplitudes reached there ($\approx$ 1 rad). The phase excursions go back and forth to a zero baseline, which is also congruent with the measured phases. The model parameter not discussed so far, the nonlinearity parameter n which power scales the field in equation 6.5, can be used to influence the shape of the phase modifications, but does not change the essence of the results presented here. The higher n the more the phase excursions are restricted to the field maxima and the faster

they fall off towards the wings of the pulse. That being said, the phase excursions follow the electric field instantaneously as indicated by the dashed lines. The phase oscillations introduced by $\widetilde{V}_{ci}$ feature a slight shift to earlier delays a observation that will be taken up again later.

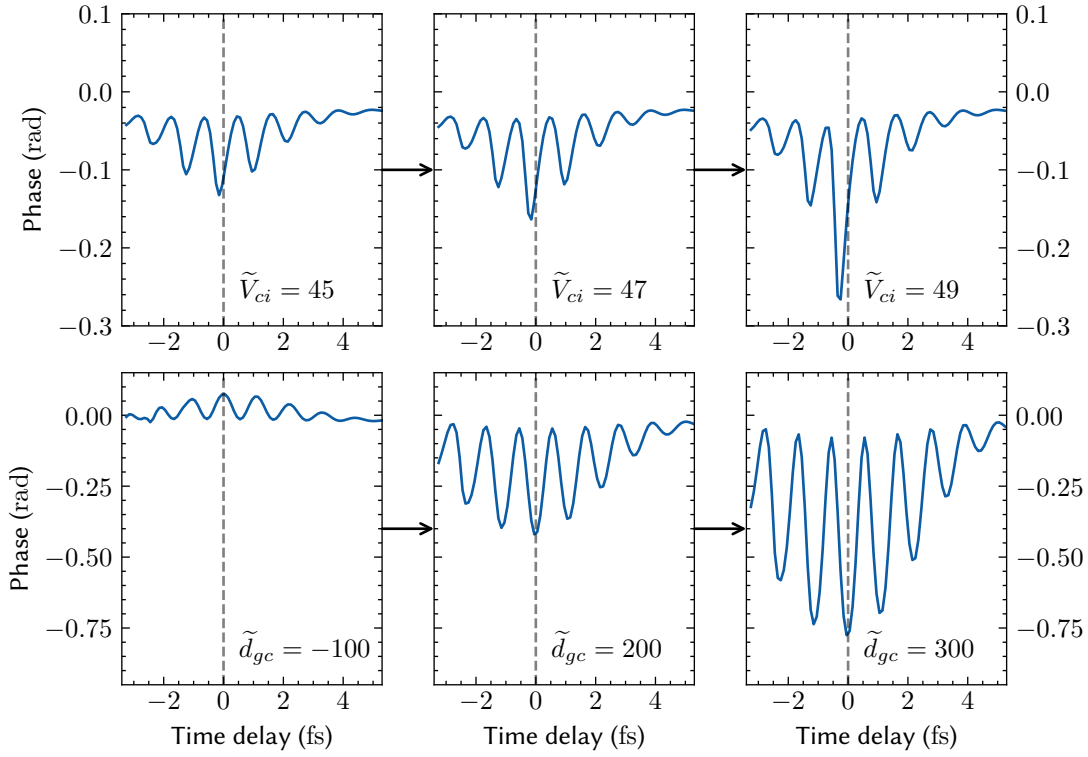

Figure 6.10.: Phase oscillations imprinted onto the dipole moment through the model parameters $\widetilde{V}_{ci}$ and $\tilde{d}_{gc}$. $\tilde{d}_{ge}$ is not considered since it introduces no conceivable phase changes above the numerical noise level. Let it be noted that the amplitude of the experimentally measured phases reaches ≈ 1 rad. The dashed lines indicate time-delay zero, where the XUV pulse sits on top of the peak of the NIR pulse.

To further evaluate the model without having to manually sample the whole parameter space a fit routine was set up. Its objective was to minimize the least-squares difference between the simulated phase evolution and a measured one over the time-delay range −2.5 to 5 fs. The measured data was extracted from the scans taken at iris position 4, which corresponds to an intensity of ≈ $1.4 \cdot 10^{14}\,\mathrm{W/cm^2}$, because this scan features both, high excursions in the phase and low noise compared to lower iris positions.

With the temporal grid settings mentioned above, the computation of a single spectrum takes < 1 s on a standard PC and a sparse time-delay scan can be performed in half a minute with an octa-core processor. With this a single evaluation of the automatic phase fit procedure[4] took four to fourteen hours depending on number of free parameters in the model and the optimization algorithm.

The optimal parameters $\tilde{d}_{ge}$, $\tilde{d}_{gc}$ and $\widetilde{V}_{ci}$ determined by the optimization routine for the model presented here are listed in table 6.2 and the corresponding phases are plotted in figure 6.11.

algorithm	$\tilde{d}_{ge}$	$\tilde{d}_{gc}$	$\widetilde{V}_{ci}$
DS	$8 \cdot 10^{-4}$	280.11	12.36
GD	22.35	238.28	24.36
manual	0	200	30

Table 6.2.: Model parameters determined from the fit procedure. DS: downhill-simplex algorithm, GD: conjugate-gradient descent algorithm.

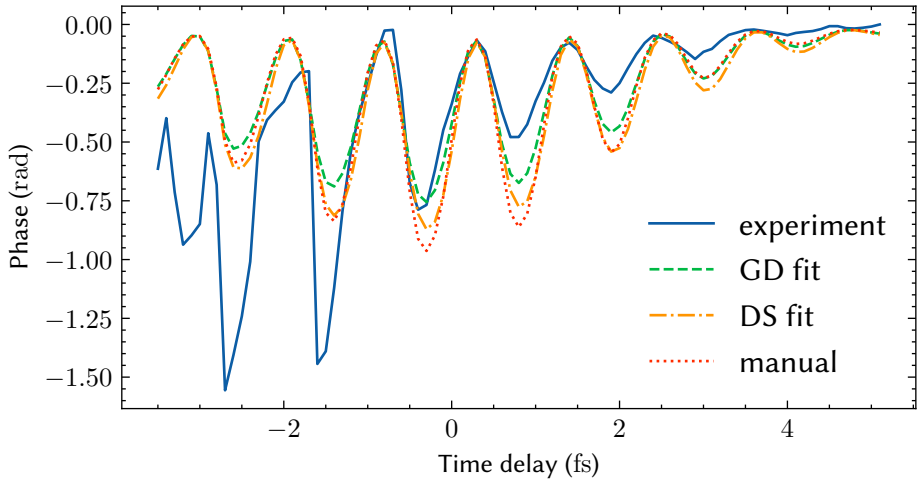

Figure 6.11.: Results of fitting the model parameters to the experimental phase oscillations. The coarse manual adjustment for initialization and the results of two minimization algorithms are shown.

The modeled phases indeed capture the shape of the experimentally observed curve taking into account that the exact shape of the NIR field is not known and that the experimental signal becomes increasingly uncertain at negative time delays where the amplitude of the absorption line is low.

[4]Different algorithms from the Python3 package `scipy.optimize`[205] were used.

Taking the fit results from the gradient descent algorithm as an example, it is insightful to examine the relative changes of the coupling matrix elements introduced by the NIR field dependence. Figure 6.12 presents the time-varying model parameters $d_{ge}(t)$, $d_{gc}(t)$ and $V_{ci}(t)$ and the resulting $q(t)$. The asymmetry parameter is half-cycle modulated with large peaks at the field-nodes (Lorentzian line shape, $\phi = 0$) and valleys down to $q = 2$ (Fano line) at the peak of the pulse. Looking at the relative changes of the model parameters it now also makes sense that $d_{ge}(t)$ cannot be used to introduce a line-shape asymmetry: considering that it constitutes the numerator of equation 6.4 for the q-parameter, reducing the naturally high $q \approx 100$ can only be achieved for $d_{ge} \longrightarrow 0$. This in turn is only possible for the peak of the central half-cycle with the NIR-dependencies taken into account here, since a negative field-scaling to reduce the offset given through the field-free matrix element quickly leads to negative values in $d_{ge}(t)$ that result in unphysical negative optical densities. For d_{gc} and V_{ci} in the denominator the situation is different. Here, increasing the coupling helps bringing the q-parameter down towards zero, which corresponds to an enhancement of the asymmetry. In the model the asymmetry is thus dominated by the ground-continuum dipole matrix element because the absorption line is strongly suppressed for the case of large configuration interaction. The experimentally observed phase evolution $\phi(\tau)$ can now be understood as probing the real-time-varying asymmetry with an XUV pulse at a given delay, which corresponds to the convolution of $\phi(t)$ with the finite pulse.

6.4.4. Model evaluation and discussion

Summarizing the findings of the few-level simulations of a time-dependent Fano system, it is found that the experimentally observed results can be qualitatively reproduced by the model. Oscillations of the line-shape asymmetry as a function of time-delay are a signature of the NIR-field-induced modulation of the coupling between the ground state of the system and the continuum state, while the buildup overshoots can also be a feature of the temporal variation of the dipole matrix element between the bound states. Laser-induced configuration interaction has the power to influence both, amplitude and phase, although the latter only as a secondary effect, while the former results mainly in suppression of the absorption line.

Finally, the following physical interpretation of the Fano model is proposed: At the lower intensities considered here, the NIR laser pulses dress the neutral ground state wave function such that it forms a superposition between one part that is driven away from the nucleus and ionized at the peak of every NIR half-cycle, while the remainder is only rearranged to return to its equilibrium position after the laser is gone. This latter part is polarized by the field such that it is redistributed to states that projected onto the field-free eigenstates of the Hamiltonian have a valence hole that can be filled from the $4d$ shell via absorption of an XUV photon. While this absorption makes up for the occurrence of the overshoots, the dipole-coupling between these field-polarized states can be expected to be different from that of the field-free states. Thus, the excitation of

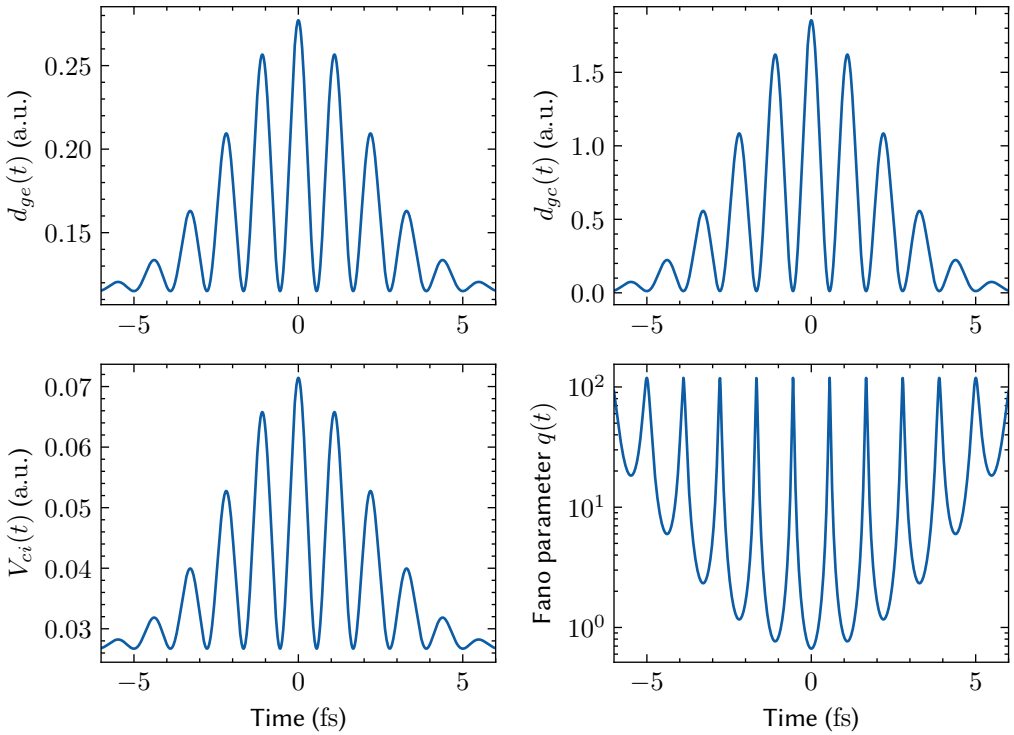

Figure 6.12.: Relative changes of the time-dependent coupling matrix elements and the corresponding modulation of the Fano q-parameter. The relative change of d_{gc} dominates the asymmetry. The field-free matrix elements are $d_{ge} = 0.115$, $d_{gc} = 0.0115$ and $V_{ci} \approx 0.027$. The time-dependent parameters were taken from the GD fit to the measurement data (see table 6.2).

the dipole takes place in a different environment and with different couplings than its decay after the laser pulse is gone, which is exactly the physical context in which to see the few-level model. This asymmetry between excitation and decay is reflected in the phase oscillations and the asymmetric line shapes.

A theoretical study by Pabst et al. [91] goes along similar lines. It is the only study discussing line-shape modifications that occur for overlapping pump and probe pulses and concludes that the 'phase shift comes from field-induced mixing of the excited N-electron states with the neutral ground state'. While no phase oscillations or sub-cycle evolution is reported in the study, the 'field-induced mixing' describes exactly the polarization discussed in the paragraph above.

Even with the approach to fit some of the model parameters in a prescribed manner, only a small portion of the whole parameter space of the model could be sampled in an adequate manner and relies partly still on the choices of the investigator. On top, the fit procedure by design expects the model to describe the dynamics underlying the experimental data in their entirety which is certainly a strong assumption. Other phenomena such as the Stark effect that was previously excluded to produce the phase oscillations on

its own, could still contribute to the overall phase. To be able to quantify this impact, the difference in polarizabilities $\Delta\alpha$ between the valence-hole and core-hole configurations $5p^{-1}$ and $4d^{-1}$ would need to be supplied.

One advantage of the Fano model in contrast to other conceivable models is its focus onto the couplings in the system. In this manner it does not differentiate, whether the ground- or excited state wave functions are perturbed, which gives it a touch of universality. Going forward, apart from implementing other models, a treatment of mixed states through a density matrix formalism can be favorable to account for mixtures of atoms that, e.g., sample different NIR intensities that result in different coupling strengths between quantum states.

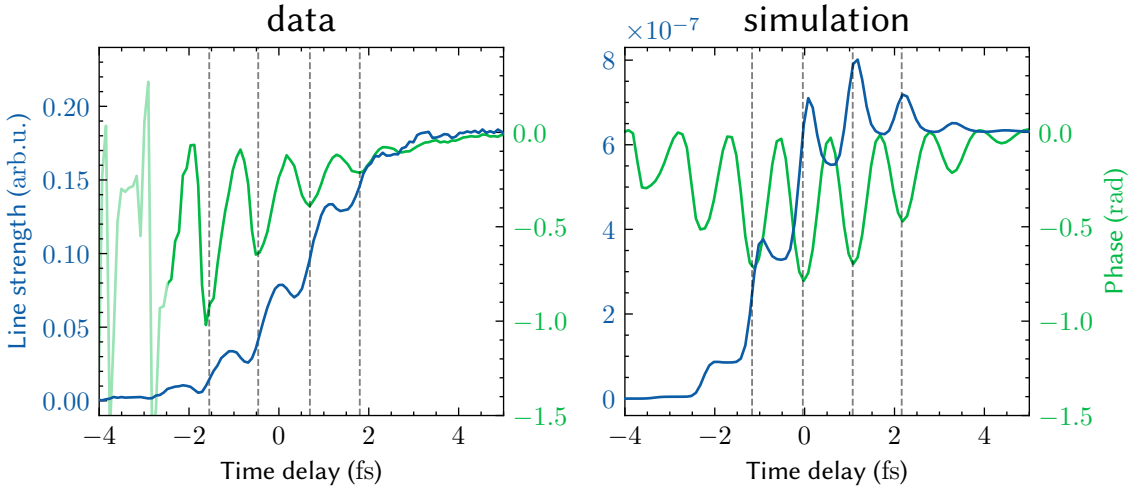

Figure 6.13.: Line strengths (blue) and phases (green) as a function of time delay from both, measured data (left) and numerical simulations (right). The dashed lines serve to indicate the maxima of the phase excursions to facilitate the comparison with the buildup structure.

A general advantage of the approach to employ a line-shape analysis to gain insights into the experimental data is illustrated in figure 6.13. Here, line strengths and phases of the main absorption line of interest T_1 are plotted for a single time-delay scan giving access to a complete characterization of the buildup in a comprehensive picture. Extracting precisely the same information directly from the dipole moment calculated in the simulations allows to relay the insights gained there to the actual quantum system. Although a look at the overshoots in the simulation shows that it does not yet describe exactly what is going on in the measurement, it constitutes a big step in the right direction. For example a detail such as the relative position between the valleys of the phase excursions indicated by the markers to the peaks and dips in the buildup of the line is reproduced relatively well and can be interpreted thanks to having complete access to the NIR field in the simulation. There, it was seen in figure 6.10 that the phase excursions are either linked to the field directly or with a slight advance depending on the matrix element under investigation. Once the model is improved one can therefore envisage statements

about possible delays between the overshoots in the population and the phase as seen in the experimental data. On top, since the effect of the different model parameters on the dipole phase varies greatly, optimizing only the phase evolution in the fit procedure does not treat them on an equal footing and disregards additional information such as the buildup structure. Combining both observables in one routine is the logical next step.

6.5. Intensity dependence

Finally, the question how to explain the intensity dependence of the line-shape asymmetry is still untouched. Besides the oscillations of the dipole phase $\phi(\tau)$ as a function of time delay addressed so far, one can observe a decrease in the amplitude of these oscillations as a function of the NIR intensity (see figure 6.2). From Sabbar et al. [57] it is known that the overshoots in the ion buildup decrease with intensity, an effect that is reproduced here. The explanation is a competition between the polarization dynamics that cause the overshoots and the ionization that provides the monotonous increase in ion population. Because the latter is strongly non-linear (ADK), while the former scales proportional to the squared field $\propto |F_{NIR}(t)|^2$, polarization effects are overtaken by ionization at high field strengths but dominate at low intensities where the threshold for ionization is higher. Qualitatively, the same happens with the phase oscillations. Figure 6.14 shows

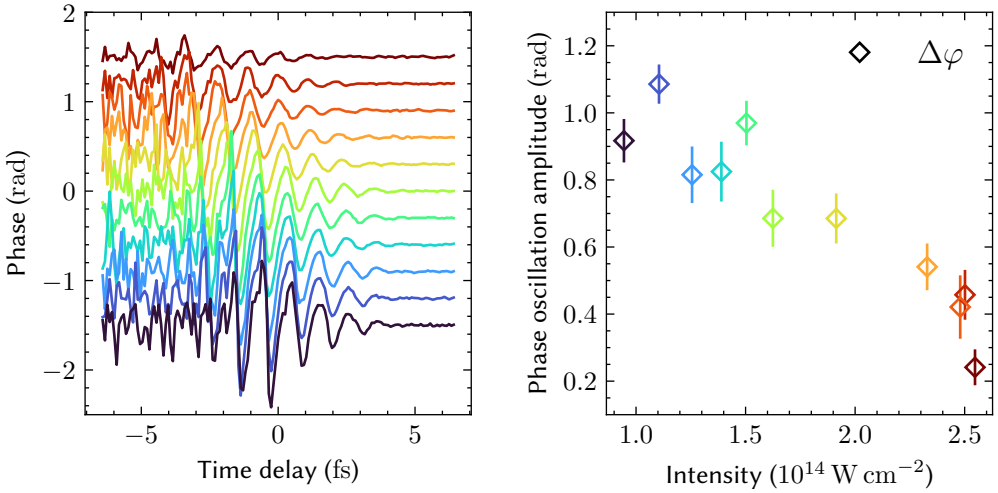

Figure 6.14.: Scaling of the phase oscillations with intensity. (left) Low-pass filtered phases as a function of time delay with an offset of 0.3 rad between consecutive curves. (right) Maximum phase amplitudes $\Delta\varphi = \varphi_{max} - \varphi_{min}$ as a function of the measured intensities.

the low-pass filtered oscillations, which were obtained by convoluting the phases $\phi(\tau)$ with a cosine window-function with the width of a full NIR cycle. The amplitude of the remaining oscillations decreases with intensity, where the best functional description of

the decline is an inverse proportionality with intensity. As the intensity increases, the part of the wave function that is irreversibly ionized increases at the cost of the portion that remains. Since this 'reversible' part to put it in the words of [57] was responsible for the observed overshoots and oscillations, the effects decrease as a function of intensity.

For the higher intensities, the competition between polarization and ionization is even encoded in a single time-delay scan. In the leading edge of the pulse small overshoots in the buildup are still visible, while later in the pulse, when the neutral ground state is depleted, only flat plateaus remain since there is nothing left to polarize. The same trend can be noticed for the phase oscillations, which fade out earlier the higher the intensity. This observation can serve as a starting point to improve the original Fano model. When the consequence of the depletion of the neutral ground state is a reduction of the polarization phenomena studied here, this effect can be taken into account in the model as a modification of the time-dependent couplings. In a first approach, the temporal variation of the coupling matrix elements is scaled proportionally to the decreasing neutral population $P_0(t)$ during the time evolution. The result is depicted in figure 6.15 and reveals that this model indeed improves the simulation results. Especially two aspects are noticeable: the overshoots at late time delays are suppressed, which is in better agreement with the measurement and led to the formulation of the idea implemented here. On top, the maximum of the phase excursions has moved towards the leading edge of the NIR pulse, which matches the experimental data as well. Together, these observations lead to the conclusion that inhibition of polarization dynamics through depletion of the neutral ground state has to be taken into account.

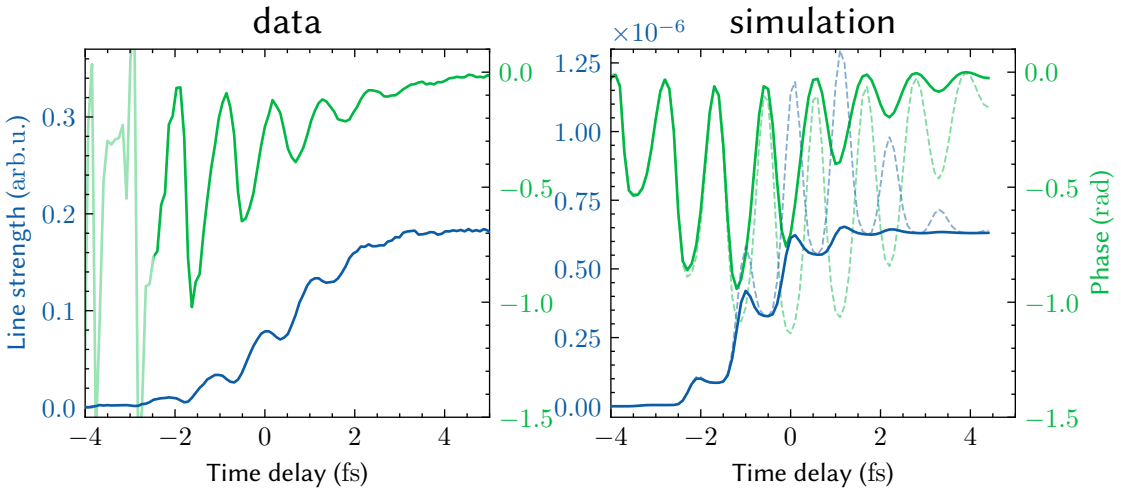

Figure 6.15.: Line strengths (blue) and phases (green) as a function of time delay from both, measured data (left) and simulations (right) with the original (dashed) and extended (solid) model, which takes ground-state depletion into account. The model parameters for curves shown here were found by applying the phase fit routine with the extended model.

6.6. Synchronicity and delay of double ionization

Apart from fitting the line strengths, linewidths and phases of the transitions in singly ionized transitions, the fitting procedure employed at the beginning of this chapter included the three dominant transitions in Xe^{2+} as well. Due to their reduced production and the resulting low SNR, they were included in the fit as Lorentzians with a linewidth fixed at the literature value. The fit results of the amplitudes are shown in figure 6.16. A new finding here, which only comes to light at the highest intensities and which has not been reported yet, is that the ultrafast buildup of the doubly ionized species is governed by the same overshoots that have been reported and explained for Xe^{+}. This shows that polarization dynamics play a role for Xe^{+} and the double ionization and at the same time demonstrates the combined excellent spectral and temporal resolution of our setup.

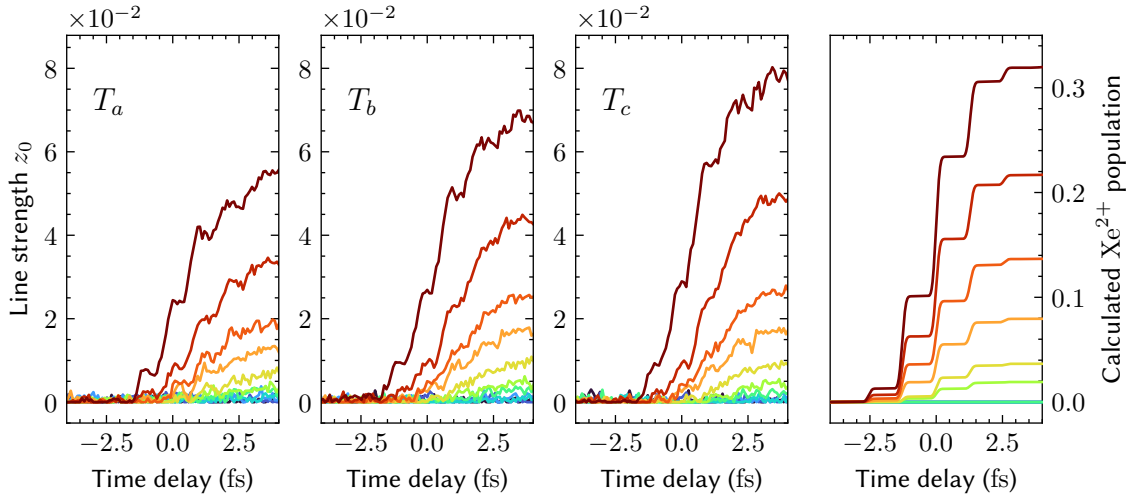

Figure 6.16.: Half-cycle buildup of Xe^{2+} ion population. The intensity of the NIR pump pulse is encoded in the color of the different lines and increases from blue to red. In the rightmost panel the ion population was calculated according to ADK rates for single and double ionization. To coarsely match the curves the intensities in the calculation were evenly sampled between the experimental minimum and maximum.

Since the Xe^{2+} lines are best visible at the highest intensity, the line strengths of the three Xe^{2+} transitions are plotted alongside that of the Xe^{+} transition T_1 in figure 6.17 and the calculated ion populations for the two species. The step-wise increase in the buildup is synchronous for all of these, even though the ionization of the singly ionized species occurs earlier in the pulse. This makes sense in the ADK picture, where the ionization shifts to the front of the pulse because of saturation and the higher ionization potential of Xe^{2+} compared to Xe^{+} . At the same time, these plots suggest that the double ionization is the result of a sequential process, where the first ionization occurs in a half-cycle in the leading edge of the pulse followed by a second ionization event near its peak. The results presented here allow to monitor the sub-cycle nature of the buildup in half-cycle steps

every ≈ 1.12 fs and the onset of the Xe^{2+} ion lines is delayed by a full cycle with respect to Xe^{+}. This is not in agreement with the report by Kobayashi et al. [42] of attosecond delays (< 1 fs) in the ionization between the two species, based on fitting step functions to the buildup. Together with a quantification of the delays for the individual absorption lines, this calls for further investigation of this topic of double ionization delays.

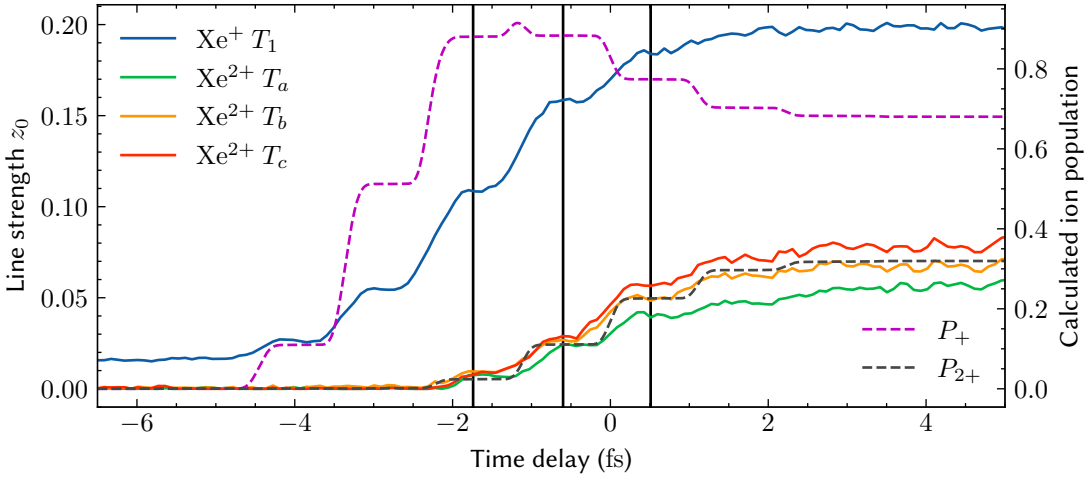

Figure 6.17.: Line strengths of the Xe^{2+} transitions and the transition T_1 of Xe^{+} together with calculated ion populations P_+ of Xe^{+} and P_{2+} of Xe^{2+}. The vertical lines are guides to the eye to indicate the coarse synchronicity of the half-cycle steps in the buildup.

6.7. Conclusion

To conclude this chapter, the results of the line-shape analysis of xenon resonances for overlapping pump and probe pulses are briefly summarized here. The experimental data that was evaluated in this chapter stems from a campaign that recorded time-delay scans as a function of NIR intensity. Two approaches to analyze these scans were presented: line-shape fits can be used to extract amplitudes, phases and widths of individual resonances as a function of time delay and intensity under the assumption that the fit model is suitable to describe the data. With the fit results as a starting point, a second method was pursued, which transforms the spectra to the time domain in order to investigate the time-dependent dipole moment. Both methods reveal a half-cycle modulation of the asymmetry of the line shapes of the Xe^{+} transitions as a function of time delay, which manifestation of a variation of the initial phases of the dipole. The origin of this phase modulation was investigated by implementing simulations that numerically solve the temporal evolution of a model atom subjected to a strong NIR pulse. The model of a prototypical Fano system, in which the coupling matrix elements become field-dependent, provide an intuitive interpretation of the observed oscillation of the dipole phase as a

function of time delay. The intensity dependence is discussed in terms of competing reversible polarization and irreversible ionization dynamics. Further, the role of ground-state depletion as a factor that suppresses the polarization is unraveled by expanding the original model.

Of course due care with these results has to be taken as the few-level model solved here only constitutes a first approach to develop an understanding of the ongoing physics and makes strong assumptions on the system and its dynamics. Nevertheless, these findings evoke the theoretical analysis of Pabst et al. [91], where a phase change due to the dressing of the neutral ground state is predicted. This interpretation can be conciliated with our picture although they do not observe a sub-cycle modulation of the phase, which might be attributed to their 2 fs short NIR pulse. For a more definite interpretation an *ab initio* grid simulation [206] that can project actual spatial wave functions onto the field-free configurations is indispensable. Still, a first, intuitive approach to explain the experimental observations has been formulated.

An important implication of this experimental study is to lay bare the shortcomings of the ionization model. While different and more evolved analytical models for strong-field ionization apart from the ADK model used here exist (see section 2.2.2), they all use the single-active electron approximation and thereby exclude important aspects of the actual multi-electron dynamics. Apart from the overshoots in the ion buildup that have been observed before [24; 57; 87], the phase oscillations reported here constitute a phenomenon that warrants the inclusion of multi-electron polarization dynamics into the ionization model. Lately [207–210], polarization in strong fields and its effects on SFI gained a lot of attention, possibly because advances in computational power allow to include it in grid simulations. In some of these studies the multi-electron dynamics are modeled by effective single-electron potentials [211; 212] to simplify the system. The solution of the Schrödinger equation still needs extensive computations even for simplified wave functions that can be used with these effective potentials, but constitutes a first step towards an analytical description of polarization dynamics.

6.8. Outlook

As discussed above, the intensity dependence of both the overshoots in the buildup as well as the phase oscillations can be explained by a competition between polarization and ionization effects. While the intensity scan presented here reaches the upper limit to which this contest can be driven, it did not explore the low intensity limit, where one might look for exclusive polarization prior to irreversible ionization. In a measurement, the goal here would be to detect transient absorption lines only when the XUV pulse overlaps with the peaks of the NIR pulse as the signature of the buildup overshoots without the said buildup itself. Since the threshold for ionization is higher than for this polarization effect there should be an intensity window where the electrons in xenon can be rearranged such by the laser field that it forms effective valence-shell holes which

allow to transiently absorb XUV light. The proposed experiment would thus aim to scan the intensity down from a point where just a minimum amount of ions is created to the point where no ion signal is left in the live analysis, since at the level of precision needed here to detect transient lines in the pulse overlap will most likely only reveal results in post-analysis.

From the reported results on Xe^{2+} ion dynamics it is evident that a more thorough approach to investigate the buildup and double-ionization dynamics is still pending. Both, intensity-dependent and transition-line-specific delays in the double-ionization can be examined to get a first handle on the interplay between polarization and ionization with the possibility to compare between transitions of different charge states. Eventually the goal is to compare the experimental results to *ab initio* simulations, but more work can also be dedicated to more evolved ionization models to gain further insights on the way.

Speaking about delays, which is currently an ubiquitous topic in the field of quantum dynamics, the question how the polarization response of the quantum system follows the electric field is a logical consequence. A first step towards answering it was made by studying the dipole phases which result from different coupling mechanisms of the Fano model presented here. More importantly, by comparing both the buildup of the resonance and its asymmetry as a function of time delay, both quantities can be referenced to each other, which allows a quantitative evaluation that would not be possible by focusing on any of the two observables alone. While the Fano model does not yet have the power to allow any definitive statements, the approach presented here shows how the problem may be tackled with a more advanced model.

7. Conclusion and outlook

The central theme of this thesis revolves around the time-resolved study of strong-field ionization (SFI) triggered by femtosecond, near-infrared laser pulses. Although the basic description of SFI [67] and analytical ionization rates [56] have been around for decades, experimental investigations were limited to the detection of asymptotic ion or electron yields. With the advances in attosecond science [29; 30], the capability to resolve optical field cycles has been achieved, but application to the direct investigation of SFI dynamics remains scarce [24; 87]. Recently, attosecond transient absorption spectroscopy was used to monitor the ionization process in a time-resolved manner to reveal that sub-cycle polarization of the target atoms leads to transient overshoots in the ion population [57]. Because they are intrinsically linked to the NIR waveform these overshoots can be used to track delays in the probe step. In a first study, the delays imprinted to different spectral components of the XUV pulses through dispersion in metal-foil filters are retrieved and it is shown that the method has a precision of 5 as. Furthermore, the investigation of SFI dynamics is extended to an analysis of the observed absorption line shapes. Focusing on the line-shape asymmetry instead of the transition strength we can access the effect of the strong-field ionization onto the time-dependent dipole response of the atoms. The observed, delay-dependent modulation in the initial phases of the dipole moment are interpreted as a strong-field dressing of the system.

The measurement series presented here were performed before and after the whole experimental equipment was moved to a new laboratory. To facilitate this, the layout of the new laboratory and the optical tables was planned and along the re-installation of the laser, optics and vacuum beamline, the infrastructure for power, gas and vacuum supply was set up and improved. Apart from the recommission and the verification of the performance of our setup, several upgrades were undertaken over the course of this thesis. To compress our laser pulses to < 5 fs at full power (5.4 W) while keeping the beam mode stable, we designed and installed our own doubly-differentially pumped hollow-core fiber. To measure and stabilize the carrier-envelope phase of the laser pulses where it is needed the most, an $f - 2f$ interferometer was transferred from the laser directly to the front of the vacuum beamline. A CEP stabilization with an RMS error of down to 163 mrad was achieved. An external incoupling of the NIR pulses was designed and implemented to enable more variability in our interferometric measurements. From first proof-of-principle measurements to the full-fledged implementation, we have developed a technique to record reference spectra *in situ* that will play an important role in the future of absorption spectroscopy. It is particularly well-suited for the measurement of broad spectral structures and therefore for the access of real-time attosecond dynamics. Together with the temporal resolution of 85 as and spectral resolution of ≈ 20 meV, it promotes our beamline to a state-of-the-art device with a sensitivity of 10 mOD per single spectrum.

Together with the installation of a new electron time-of-flight spectrometer, a parallel development was pursued in the design and fabrication of an absorption target cell that would allow to operate the electron spectrometer while recording absorption spectra with sufficient signal at the same time. As an implementation of a gas jet array our new hybrid cell fulfills this requirement and has enabled us to perform attosecond streaking and absorption measurements simultaneously. To the best of my knowledge, this is the first time such a setup has been realized. In a first step it enables to characterize both the NIR and XUV pulses in the absorption measurements *in situ*, while in the future the synergy of both methods may reveal additional information based on the complementary, correlated data sets.

Spectroscopically, the prime subjects of investigation in this thesis are the $4d$-core to $5p$-valence transitions in singly ionized xenon. Through their excitation by an attosecond XUV pulse, the presence of xenon ion population can be probed as it is produced via strong-field ionization through an NIR laser pulse. Contrary to the established SFI theories, where the ionized fraction of atoms increases monotonically in time across the pump pulse, the true buildup features overshoots that can be attributed to reversible polarization dynamics. One result of the work presented here, is that the oscillatory structure of the time-delay-dependent buildup can be used as a timing reference by extracting its phase across different resonances. Introducing the dispersion in aluminum metal-foil filters as an experimental control parameter, the chirp imprinted onto the XUV pulses could be accessed with attosecond precision, a result that is underpinned by additional numerical modeling. Having found that delays in the excitation can be tracked with a precision of 5 as, several interesting measurement schemes are proposed. Benefiting from the aforementioned *in situ* reference in particular, the temporal modulation of the continuum absorption as an atom is ionized could provide a method to retrieve the spectral phase of the XUV pulse and the phases of the continuum dipole matrix elements. In molecules, the site-specificity of the XUV probe could elucidate how charges rearrange after strong-field valence ionization. Last but not least, having demonstrated that multiple ionization of xenon is possible with our setup, an intensity-dependent study of the xenon giant-dipole resonance in ATAS could reveal temporal dynamics in the contraction of the $4f$ wave function, which has been investigated in static absorption spectroscopy for decades.

The other measurement series reported here features an intensity scan of the NIR pump pulse in the range $1–2.5 \cdot 10^{14}\,\mathrm{W/cm^2}$, which corresponds to just barely ionizing xenon at the start to eventually saturating the singly ionized species with the onset of double ionization. The buildup of double ionization appears to be delayed to the single ionization by a full field-cycle of the laser field, which points to a sequential process. The central finding of the intensity scan are the line-shape changes that are observed when the pump and probe pulses overlap. Both, parametrized line-shape fits and an investigation of the reconstructed time-dependent dipole moment reveal that the observed line-shape asymmetries are caused by an initial non-zero phase of the dipole emission that is the quantum mechanical origin of the absorption lines. The peculiarity of this

measurement series is that the phase shows intensity-dependent oscillations across the time-delay overlap, which cannot be explained solely by a Stark shift of the involved states. Setting up numerical few-level simulations of a model atom, it is found that phase oscillations occur when the configuration interaction and dipole transition matrix elements in the system are made field-dependent. Bearing in mind that the field strengths at play are high enough to ionize the system, it can be reasoned that the atomic potential is strongly distorted at the peaks of the field. The field-dependent modulation of the couplings in the model now mimics this effect, by altering the environment in which the excitation by an XUV photon takes place, which is a strongly polarized atom. The intensity dependence of the phase oscillations is discussed as the result of a competition between reversible polarization and irreversible ionization dynamics and it is found that depletion of the neutral ground state plays a role in the suppression of the polarization at higher intensities. While the few-level simulation at hand certainly has its caveats, the intuitive interpretation provides first insights into a strongly driven system on the basis of the line-shape analysis. While the next steps in this study will certainly involve grid-based *ab initio* simulations, the shortcomings of simple ionization models such as ADK theory become clear. Using the single-active electron approximation, where all but one electron are only represented by a screening potential, is insufficient to capture the details of the polarization of the atom in its temporal complexity. In addition to the buildup overshoots that have been studied previously, the effect reported here for the first time, namely the sub-cycle phase oscillations, escapes this treatment as well. I resume that strong-field ionization does not only lead to the ejection of electrons that leave behind an ion, but it is worth taking a closer look at the details of these dynamics.

To conclude, I find that this thesis has raised at least as many new questions as it answered. Setting out with the goal of performing spectroscopy on ions, I found that this can be challenging at best and needs a machine and crew working at peak performance. Apart from the results reported here, there is more to learn by studying strong-field ionization with ATAS and some ideas that fellow students may pursue are outlined in the individual chapters. Talking about all these experiments, I find it easier to convey them in the (to physicists) well-known jargon of a pump and probe scheme, where the ions are created by the NIR and subsequently probed by the XUV pulse. However, the true beauty of ATAS resides in turning the time-delay axis around as the intensity scan analysis shows with an intricate interplay between the pulses. While a part of the NIR is needed to provide ions to be probed, the dipole that decays after the XUV excitation is dressed by the remaining NIR fraction. While this might seem messy, I find that it is the ideal playground to investigate strong-field induced effects at a level where not even the destruction (ionization) of the system poses a limit, while remaining highly sensitive to the dynamics that occur due to the selectivity of absorption pathways. As stated in different parts within this work, I think that focusing on the extraction of real time attosecond dynamics through the observation of broad continuum structures will be an important branch of ATAS experiments in the future.

A. Appendix

A.1. Atomic units

Especially within theoretical context it is often convenient to adapt the scales on which physical quantities are measured based on the underlying physics. Within the field of atomic and molecular physics, the prototype system hydrogen provides these scales and is used to define the system of atomic units (a.u.). In this system the following conventions $m_e = e = \hbar = \frac{1}{4\pi\epsilon_0} = 1$ apply. Some derived units, that are important for this work are presented in table A.1. These units directly illustrate, which order of magnitude can be expected for the dimensions and dynamics of atomic systems.

Unit	Definition	Value
Length	$a_0 = \frac{4\pi\epsilon_0\hbar^2}{m_e e^2}$	$5.292 \cdot 10^{-11}$ m
Energy	$E_h = \frac{e^2}{4\pi\epsilon_0 a_0} = \alpha^2 m_e c^2$	27.2114 eV
Velocity	$v_0 = \frac{e^2}{4\pi\epsilon_0\hbar c} = \alpha c$	$2.188 \cdot 10^6$ m/s
Time	$\frac{a_0}{v_0} = \frac{\hbar}{E_h}$	$2.419 \cdot 10^{-17}$ s
Field strength	$E_0 = \frac{e}{4\pi\epsilon_0 {a_0}^2}$	$5.142 \cdot 10^{11}$ V/m
Intensity	$I_0 = \frac{1}{2}\epsilon_0 c E_0^2$	$3.509 \cdot 10^{16}$ W/cm^2

Table A.1.: Important quantities used in the study of laser-atom interactions rescaled in atomic units.

A.2. Spectral resampling and rescaling

Because of the dispersive properties of gratings, photon spectra are recorded on scales that are roughly proportional to wavelength. When the spectrum in the frequency domain is needed, a change of variables has to be performed, which—when done properly—preserves the photon flux when integrating over a part of the spectrum in either domain.

Let $S(\lambda)$ and $S(\omega)$ be the respective spectra in the wavelength and frequency domain. With the transformation $\lambda \longrightarrow f(\omega) = \frac{c}{\omega}$ one might naively assume that $S(\lambda) \longrightarrow S(f(\omega)) = S(\omega)$, which is wrong. Through the nonlinear transformation $f(\omega)$, the spectrum gets distorted. In the domain, in which the spectrum is recorded, the counts per bin correspond to an actual photon flux, i.e. a physical observable that should be preserved in the transformation. To achieve this, the determinant of the Jacobian of the transformation has to be taken into account, here $\det(J(\omega)) = \frac{\partial\lambda}{\partial\omega} = \frac{\partial f(\omega)}{\partial\omega} = -\frac{c}{\omega^2}$. The Jacobian rescales the amplitudes of the transformed spectrum such that the integral over different spectral regions is the same in both domains.

$$S(\lambda) \longrightarrow S(f(\omega))|\det(J(\omega))| = S(\omega). \tag{A.1}$$

For illustration purposes, I chose a specific transformation as an example. But of course this applies to any nonlinear transformation between different scales.

To make things more user friendly, here is a pseudo-Python code snippet, that performs the resampling and rescaling:

```
# import packages
import numpy as np
import scipy.constants as const
from scipy.interpolate import interp1d
import attopy.unit_converter as uc     # attopy does not exist just yet

# load data
wavelength = np.loadtxt('Wavelength.dat')
spectrum_wavelength = np.loadtxt('Spectrum.dat')

#compute transformation scale and define linear interpolation array
photonenergy_nonlinear = uc.nm_to_ev(wavelength)
photonenergy_linear = np.arange(start_index, end_index, 1) * energy_multiplier
#compute amplitude rescaling
jacobian = const.c/photonenergy**2

# resampling
f = interpolate.interp1d(photonenergy_nonlinear,spectrum)
spectrum_photonenergy = f(photonenergy)
# rescaling
spectrum_photonenergy *= jacobian
```

A.3. Color scale

I want to express the opinion that any two-dimensional color plot is in principle a clever lie presented by the author for the reader to consume. Color scales are perceptually very different, everyone has one or a few color maps he/she prefers and is used to and by careful design a lot of information can be hidden or overemphasized based on the wishes of the author. To summarize: they are not objective. Wherever possible the relevant information is therefore presented in graphs, that use color only to differentiate between different lines. Where this was not possible I used the perceptually uniform color map described here [213] and shown in figure A.1. All plots and images were generated and/or modified either with the Python package Matplotlib [214] or Corel Draw.

Figure A.1.: Color map *turbo*, used throughout this thesis.

A.4. Things that broke

In a rather humorous mood, I compiled this list of things, that for one reason or the other stopped performing the function they were expected to. It may either serve to demonstrate that experiments are more than just the result of completing a fixed task (as many people outside the scientific domain seem to think) or may console future students, that desperate at the fact, that something just broke, to show, that it has always worked this way and that you have got to keep pushing. It also shows that uncertain measures have to be taken sometimes to ensure continuous improvement.

Ordered by high to low severity of the incident, which fortunately corresponds to an increase in the number of events per item in the list:

- The DM-50 amplifier pump laser reached the lifetime of its diodes. Laser 4 months down.
- The AOFS crystal in the oscillator: 1 month of diagnostic work.
- The pump-combination amplifier end-mirror. Human error: 2 week interruption.
- EDX vacuum pre-pump. First only a rotor got stuck, but it was eventually destroyed because the exhaust did not work the way it was supposed to.
- Fibers. Countless hollow-core fibers fell victim to our desire to push the average beam power before the double-differentially pumped HCF. With the correct alignment procedure (!!!) this one has lasted more than 6 month. Some common fibers in the D-Scan solarized in the SHG branch of the setup. We now have one special UV fiber for this spectral range.
- Mirrors. When something is weird on the way to the beamline, it might be a good idea to check for damaged mirrors. When the inner mirror in the beamline needs to be exchanged, make sure to mount a camera from above prior to the procedure, to monitor the process and to simplify the positioning of the new mirror.
- Brewster windows. Many. They like clean environment. For the fiber, a ceolith trap helped to get rid of abrasion from the scroll pump. At the beamline the change from steel to Macor cells proved valuable to reduce ablation of material that ends up on the optics.
- Target cells, nozzles. The old steel target cells were usually slitted after some time. Macor for the win! The glass target nozzles were fried a few times as well; it remains to see how well the new hybrid cells fare.
- Pellicle filters. Some last longer than others, but two were actually burned in my intensity scans, which was new. The Kapton filters are thicker (dispersion) but certainly stronger. We should probably find a company that delivers the pellicles with a hole, such that we do not get the chance to mess this up on our own.
- Metal-foil filters. Due to their nanometer thickness their certain death is inevitable. At the very latest, when the beamline is vented by a power failure. But most probably died in the construction of our concentric filters.

A.5. Abbreviations

AC/DC	alternating current / direct current
ADK	Ammosov, Delone and Krainov
AOI	angle of incidence
APT	attosecond pulse train
ATAS	attosecond transient absorption spectroscopy
ATI	above-threshold ionization
BSI	barrier-suppression ionization
CAD	computer-aided design
CCD	charge-coupled device
CEP	carrier-envelope phase
DCM	dipole-control model
FWHM	full width at half maximum
GD / GDD	group delay / group delay dispersion
HCF	hollow-core fiber
HHG	high-harmonic generation
IAP	isolated attosecond pulse
MCP	microchannel plate
NIR	near-infrared
NSDI	non-sequential double ionization
NIST	National Institute of Standards and Technology
OBI	over-the-barrier ionization
OD	optical density
RABBITT	reconstruction of attosecond beating by interference of two-photon transitions
RMS	root-mean-square (error)
SFI	strong-field ionization
SNR	signal-to-noise ratio
TDDM	time-dependent dipole moment
TEM	transmission electron microscopy
TOD	third-order dispersion
TOF	time of flight
VLS	variable line spacing
XUV	extreme ultraviolet

Bibliography

[1] Maximilian Hartmann, Veit Stooß, Paul Birk, Gergana Borisova, Christian Ott, and Thomas Pfeifer. Attosecond precision in delay measurements using transient absorption spectroscopy. *Optics Letters*, 2019. (Cited on page VII, 3, 67)

[2] Veit Stooß, Maximilian Hartmann, Paul Birk, Gergana D. Borisova, Thomas Ding, Alexander Blättermann, Christian Ott, and Thomas Pfeifer. XUV-beamline for attosecond transient absorption measurements featuring a broadband common beam-path time-delay unit and in situ reference spectrometer for high stability and sensitivity. *Review of Scientific Instruments*, 90(5):053108, 2019. (Cited on page VII, 3, 35, 43, 48, 59, 64)

[3] Shuyuan Hu, Maximilian Hartmann, Anne Harth, Christian Ott, and Thomas Pfeifer. Noise effects and the impact of detector responses on the characterization of extreme ultraviolet attosecond pulses. *Applied Optics*, 2020. (Cited on page VII, 32, 54)

[4] Veit Stooß, Paul Birk, Alexander Blättermann, Maximilian Hartmann, Gergana D. Borisova, Christian Ott, and Thomas Pfeifer. Strong-field-gated buildup of a Rydberg series. *Physical Review Research*, 2(3):032041, 2020. (Cited on page VII, 2, 26, 29)

[5] Paul Birk, Veit Stooß, Maximilian Hartmann, Gergana D Borisova, Alexander Blättermann, Tobias Heldt, Klaus Bartschat, Christian Ott, and Thomas Pfeifer. Attosecond transient absorption of a continuum threshold. *Journal of Physics B: Atomic, Molecular and Optical Physics*, 2020. (Cited on page VII, 49)

[6] Gergana D Borisova, Veit Stooß, Andreas Dingeldey, Andreas Kaldun, Thomas Ding, Paul Birk, Maximilian Hartmann, Tobias Heldt, Christian Ott, and Thomas Pfeifer. Strong-field-induced single and double ionization dynamics from single and double excitations in a two-electron atom. *Journal of Physics Communications*, 2020. (Cited on page VII)

[7] Daria Kolbasova, Maximilian Hartmann, Rui Jin, Alexander Blättermann, Christian Ott, Sang-Kil Son, Thomas Pfeifer, and Robin Santra. Probing ultrafast coherent dynamics in core-excited xenon by using attosecond XUV-NIR transient absorption spectroscopy. *Physical Review A*, 103(4):043102, 2021. (Cited on page VIII, 29, 47, 51)

[8] Thomas Ding, Marc Rebholz, Lennart Aufleger, Maximilian Hartmann, Veit Stooß, Alexander Magunia, Paul Birk, Gergana Dimitrova Borisova, David Wachs, Carina da Costa Castanheira, Patrick Rupprecht, Yonghao Mi, Andrew R. Attar, Thomas Gaumnitz, Zhi-Heng Loh, Sebastian Roling, Marco Butz, Helmut Zacharias, Stefan Düsterer, Rolf Treusch, Arvid Eislage, Stefano M. Cavaletto, Christian Ott, and Thomas Pfeifer. Measuring the frequency chirp of extreme-ultraviolet free-electron laser pulses by transient absorption spectroscopy. *Nature Communications*, 12(1):643, 2021. (Cited on page VIII, 17)

[9] Thomas Ding, Marc Rebholz, Lennart Aufleger, Maximilian Hartmann, Veit Stooß, Alexander Magunia, Paul Birk, Gergana Dimitrova Borisova, Carina da Costa Castanheira, Patrick Rupprecht, Yonghao Mi, Thomas Gaumnitz, Zhiheng Loh, Sebastian Roling, Marco Butz, Hellmut Zacharias, Stefan Düsterer, Rolf Treusch, Christian Ott, and Thomas Pfeifer. XUV pump - XUV probe transient-absorption spectroscopy at FELs. *Faraday Discussions*, 2020. (Cited on page VIII, 17)

[10] L. Aufleger, P. Friebel, P. Rupprecht, A. Magunia, T. Ding, M. Rebholz, M. Hartmann, V. Stooß, C. Ott, and T. Pfeifer. Pulse length effects on autoionizing states under the influence of intense SASE XUV fields. *Journal of Physics B: Atomic, Molecular and Optical Physics*, 53(23):234002, 2020. (Cited on page VIII, 17)

[11] Christian Ott, Lennart Aufleger, Thomas Ding, Marc Rebholz, Alexander Magunia, Maximilian Hartmann, Veit Stooß, David Wachs, Paul Birk, Gergana D. Borisova, Kristina Meyer, Patrick Rupprecht, Carina Da Costa Castanheira, Robert Moshammer, Andrew R. Attar, Thomas Gaumnitz, Zhi Heng Loh, Stefan Düsterer, Rolf Treusch, Joachim Ullrich, Yuhai Jiang, Michael Meyer, Peter Lambropoulos, and Thomas Pfeifer. Strong-Field Extreme-Ultraviolet Dressing of Atomic Double Excitation. *Physical Review Letters*, 123(16), 2019. (Cited on page VIII, 17)

[12] Thomas Ding, Marc Rebholz, Lennart Aufleger, Maximilian Hartmann, Kristina Meyer, Veit Stooß, Alexander Magunia, David Wachs, Paul Birk, Yonghao Mi, Gergana Dimitrova Borisova, Carina Da Costa Castanheira, Patrick Rupprecht, Zhi Heng Loh, Andrew R. Attar, Thomas Gaumnitz, Sebastian Roling, Marco Butz, Helmut Zacharias, Stefan Düsterer, Rolf Treusch, Stefano M. Cavaletto, Christian Ott, and Thomas Pfeifer. Nonlinear Coherence Effects in Transient-Absorption Ion Spectroscopy with Stochastic Extreme-Ultraviolet Free-Electron Laser Pulses. *Physical Review Letters*, 123(10):103001, 2019. (Cited on page IX, 17, 75)

[13] Thomas Ding, Christian Ott, Andreas Kaldun, Alexander Blättermann, Kristina Meyer, Veit Stooß, Marc Rebholz, Paul Birk, Maximilian Hartmann, Andrew Brown, Hugo Van Der Hart, and Thomas Pfeifer. Time-resolved four-wave-mixing spectroscopy for inner-valence transitions. *Optics Letters*, 41(4):709, 2016. (Cited on page IX, 2, 46, 67, 77)

[14] Elisa Di Giorgio, Marco Lunghi, Francesca Simion, and Giorgio Vallortigara. Visual cues of motion that trigger animacy perception at birth: the case of self-propulsion. *Developmental Science*, 20(4): e12394, 2017. (Cited on page 1)

[15] Michel Mayor and Didier Queloz. A jupiter-mass companion to a solar-type star. *Nature*, 378 (6555):355–359, 1995. (Cited on page 1)

[16] A. Eckart and R. Genzel. Observations of stellar proper motions near the Galactic Centre. *Nature*, 383(6599):415–417, 1996. (Cited on page 1)

[17] A. M. Ghez, B. L. Klein, M. Morris, and E. E. Becklin. High Proper-Motion Stars in the Vicinity of Sagittarius A*: Evidence for a Supermassive Black Hole at the Center of Our Galaxy. *The Astrophysical Journal*, 509(2):678–686, 1998. (Cited on page 1)

[18] B. P. Abbott, R. Abbott, T. D. Abbott, et al. Observation of gravitational waves from a binary black hole merger. *Physical Review Letters*, 116(6):061102, 2016. (Cited on page 1)

[19] Ahmed H. Zewail. Femtochemistry: Atomic-scale dynamics of the chemical bond. *Journal of Physical Chemistry A*, 104(24):5660–5694, 2000. (Cited on page 1)

[20] D. E. Spence, P. N. Kean, and W. Sibbett. 60-fsec pulse generation from a self-mode-locked Ti:sapphire laser. *Optics Letters*, 16(1):42, 1991. (Cited on page 1, 35)

[21] U. Keller, G. W. 'tHooft, W. H. Knox, and J. E. Cunningham. Femtosecond pulses from a continuously self-starting passively mode-locked Ti:sapphire laser. *Optics Letters*, 16(13):1022, 1991. (Cited on page 1, 35)

[22] Donna Strickland and Gerard Mourou. Compression of amplified chirped optical pulses. *Optics Communications*, 56(3):219–221, 1985. (Cited on page 1, 36)

[23] Tamas Nagy, Steffen Hädrich, Peter Simon, Andreas Blumenstein, Nico Walther, Robert Klas, Joachim Buldt, Henning Stark, Sven Breitkopf, Péter Jójárt, Imre Seres, Zoltán Várallyay, Tino Eidam, and Jens Limpert. Generation of three-cycle multi-millijoule laser pulses at 318 W average power. *Optica*, 6(11):1423, 2019. (Cited on page 1, 39)

[24] A. Wirth, M. Th Hassan, I. Grguraš, J. Gagnon, A. Moulet, T. T. Luu, S. Pabst, R. Santra, Z. A. Alahmed, A. M. Azzeer, V. S. Yakovlev, V. Pervak, F. Krausz, and E. Goulielmakis. Synthesized light transients. *Science*, 334(6053):195–200, 2011. (Cited on page 1, 5, 15, 76, 77, 101, 103)

[25] A. McPherson, G. Gibson, H. Jara, U. Johann, T. S. Luk, I. A. McIntyre, K. Boyer, and C. K. Rhodes. Studies of multiphoton production of vacuum-ultraviolet radiation in the rare gases. *Journal of the Optical Society of America B*, 4(4):595, 1987. (Cited on page 1)

[26] M. Ferray, A. L'Huillier, X. F. Li, L. A. Lompre, G. Mainfray, and C. Manus. Multiple-harmonic conversion of 1064 nm radiation in rare gases. *Journal of Physics B: Atomic, Molecular and Optical Physics*, 21(3):L31, 1988. (Cited on page 1)

[27] A L'Huillier, K J Schafer, and K C Kulander. Theoretical aspects of intense field harmonic generation. *Journal of Physics B: Atomic, Molecular and Optical Physics*, 24(15):3315, 1991. (Cited on page 1)

[28] Matthias F. Kling and Marc J.J. Vrakking. Attosecond Electron Dynamics. *Annual Review of Physical Chemistry*, 59(1):463–492, 2008. (Cited on page 1)

[29] Ferenc Krausz and Misha Ivanov. Attosecond physics. *Reviews of Modern Physics*, 81(1):163–234, 2009. (Cited on page 1, 103)

[30] Francesca Calegari, Giuseppe Sansone, Salvatore Stagira, Caterina Vozzi, and Mauro Nisoli. Advances in attosecond science. *Journal of Physics B: Atomic, Molecular and Optical Physics*, 49(6), 2016. (Cited on page 1, 103)

[31] H. G. Muller. Reconstruction of attosecond harmonic beating by interference of two-photon transitions. *Applied Physics B: Lasers and Optics*, 74(SUPPL.):17–21, 2002. (Cited on page 1, 33)

[32] R. Kienberger, Eleftherios Goulielmakis, M. Uiberacker, A. Baltuska, V. Yakovlev, F. Bammer, A. Scrinzi, Th Westerwalbesioh, U. Kleineberg, U. Heinzmann, M. Drescher, and F. Krausz. Atomic transient recorder. *Nature*, 427(6977):817–821, 2004. (Cited on page 1, 32)

[33] W T Pollard and R A Mathies. Analysis of Femtosecond Dynamic Absorption Spectra of Nonstationary States. *Annual Review of Physical Chemistry*, 43(1):497–523, 1992. (Cited on page 1)

[34] Mengxi Wu, Shaohao Chen, Seth Camp, Kenneth J Schafer, and Mette B Gaarde. Theory of strong-field attosecond transient absorption. *Journal of Physics B: Atomic, Molecular and Optical Physics*, 49(6):062003, 2016. (Cited on page 1, 25)

[35] Robin Santra, Vladislav S. Yakovlev, Thomas Pfeifer, and Zhi Heng Loh. Theory of attosecond transient absorption spectroscopy of strong-field-generated ions. *Physical Review A - Atomic, Molecular, and Optical Physics*, 83(3):033405, 2011. (Cited on page 2, 18)

[36] J. C. Baggesen, E. Lindroth, and L. B. Madsen. Theory of attosecond absorption spectroscopy in krypton. *Physical Review A - Atomic, Molecular, and Optical Physics*, 85(1), 2012. (Cited on page 2)

[37] Alexander Blättermann, Christian Ott, Andreas Kaldun, Thomas Ding, and Thomas Pfeifer. Two-dimensional spectral interpretation of time-dependent absorption near laser-coupled resonances. *Journal of Physics B: Atomic, Molecular and Optical Physics*, 47(12):124008, 2014. (Cited on page 2, 27, 56, 57)

[38] Veit Stooß, S. M. Cavaletto, S. Donsa, Alexander Blättermann, P. Birk, C. H. Keitel, I. Březinová, J. Burgdörfer, C. Ott, and T. Pfeifer. Real-Time Reconstruction of the Strong-Field-Driven Dipole Response. *Physical Review Letters*, 121(17):173005, 2018. (Cited on page 2, 26, 51, 56)

[39] Zhi Heng Loh, Munira Khalil, Raoul E Correa, Robin Santra, Christian Buth, and Stephen R Leone. Quantum state-resolved probing of strong-field-ionized Xenon atoms using femtosecond high-order harmonic transient absorption spectroscopy. *Physical Review Letters*, 98(14), 2007. (Cited on page 2, 31, 77)

[40] Eleftherios Goulielmakis, Zhi Heng Loh, Adrian Wirth, Robin Santra, Nina Rohringer, Vladislav S. Yakovlev, Sergey Zherebtsov, Thomas Pfeifer, Abdallah M. Azzeer, Matthias F. Kling, Stephen R. Leone, and Ferenc Krausz. Real-time observation of valence electron motion. *Nature*, 466(7307): 739–743, 2010. (Cited on page 2, 56, 67, 76, 77)

[41] Scott G. Sayres, Erik R. Hosler, and Stephen R. Leone. Exposing the role of electron correlation in strong-field double ionization: X-ray transient absorption of orbital alignment in Xe+ and Xe2+. *Journal of Physical Chemistry A*, 118(37):8614–8624, 2014. (Cited on page 2, 57, 77)

[42] Yuki Kobayashi, Maurizio Reduzzi, Kristina F. Chang, Henry Timmers, Daniel M. Neumark, and Stephen R. Leone. Selectivity of Electronic Coherence and Attosecond Ionization Delays in Strong-Field Double Ionization. *Physical Review Letters*, 120(23), 2018. (Cited on page 2, 56, 57, 77, 100)

[43] Yuki Kobayashi, Kristina F Chang, Tao Zeng, Daniel M Neumark, and Stephen R Leone. Direct mapping of curve-crossing dynamics in IBr by attosecond transient absorption spectroscopy. *Science*, 364(6448):79–83, 2019. (Cited on page 2, 75)

[44] M. Rebholz, T. Ding, V. Despré, et al. All-XUV pump-probe transient absorption spectroscopy of the structural molecular dynamics of diiodomethane. *Physical Review X*, 2021. (*Submitted*). (Cited on page 2)

[45] A. Kaldun, A. Blättermann, V. Stooß, S. Donsa, H. Wei, R. Pazourek, S. Nagele, C. Ott, C. D. Lin, J. Burgdörfer, and T. Pfeifer. Observing the ultrafast buildup of a Fano resonance in the time domain. *Science*, 354(6313):738–741, 2016. (Cited on page 2, 57, 77)

[46] Armin Scrinzi, Michael Geissler, and Thomas Brabec. Ionization above the coulomb barrier. *Physical Review Letters*, 83(4):706–709, 1999. (Cited on page 2, 13)

[47] P. B. Corkum. Plasma perspective on strong field multiphoton ionization. *Physical Review Letters*, 71(13):1994–1997, 1993. (Cited on page 2, 15)

[48] M. Lewenstein, Ph Balcou, M. Yu Ivanov, Anne L'Huillier, and P. B. Corkum. Theory of high-harmonic generation by low-frequency laser fields. *Physical Review A*, 49(3):2117–2132, 1994. (Cited on page 2, 16)

[49] P. Agostini, F. Fabre, G. Mainfray, G. Petite, and N. K. Rahman. Free-free transitions following six-photon ionization of xenon atoms. *Physical Review Letters*, 42(17):1127–1130, 1979. (Cited on page 2, 55)

[50] Peter Amendt, David C. Eder, and Scott C. Wilks. X-ray lasing by optical-field-induced ionization. *Physical Review Letters*, 66(20):2589–2592, 1991. (Cited on page 2)

[51] Tamar Seideman, M. Yu Ivanov, and P. B. Corkum. Role of electron localization in intense-field molecular ionization. *Physical Review Letters*, 75(15):2819–2822, 1995. (Cited on page 2)

[52] Chunlei Guo, Ming Li, and George N. Gibson. Charge asymmetric dissociation induced by sequential and nonsequential strong field ionization. *Physical Review Letters*, 82(12):2492–2495, 1999. (Cited on page 2)

[53] A. L'Huillier, L. A. Lompre, G. Mainfray, and C. Manus. Multiply charged ions induced by multiphoton absorption in rare gases at 0.53 μm. *Physical Review A*, 27(5):2503–2512, 1983. (Cited on page 2, 55)

[54] M. Meckel, D. Comtois, D. Zeidler, A. Staudte, D. Pavičić, H. C. Bandulet, H. Pépin, J. C. Kieffer, R. Dörner, D. M. Villeneuve, and P. B. Corkum. Laser-induced electron tunneling and diffraction. *Science*, 320(5882):1478–1482, 2008. (Cited on page 2)

[55] Dror Shafir, Hadas Soifer, Barry D. Bruner, Michal Dagan, Yann Mairesse, Serguei Patchkovskii, Misha Yu Ivanov, Olga Smirnova, and Nirit Dudovich. Resolving the time when an electron exits a tunnelling barrier. *Nature*, 485(7398):343–346, 2012. (Cited on page 2)

[56] Maxim V. Ammosov, Nikolai B. Delone, and Vladimir P. Krainov. Tunnel Ionization Of Complex Atoms And Atomic Ions In Electromagnetic Field. In John A. Alcock, editor, *High Intensity Laser Processes*, volume 0664, page 138. SPIE, 1986. (Cited on page 2, 13, 14, 103)

[57] Mazyar Sabbar, Henry Timmers, Yi-Jen Chen, Allison K. Pymer, Zhi-Heng Loh, Scott G. Sayres, Stefan Pabst, Robin Santra, and Stephen R. Leone. State-resolved attosecond reversible and irreversible dynamics in strong optical fields. *Nature Physics*, 13(5):472–478, 2017. (Cited on page 3, 15, 29, 56, 58, 68, 77, 78, 79, 80, 86, 97, 98, 101, 103)

[58] Christian Ott. *Attosecond multidimensional interferometry of single and two correlated electrons in atoms*. PhD thesis, Ruperto-Carola-University of Heidelberg, 2012. (Cited on page 3, 19, 48, 59)

[59] Alexander Blättermann. *Impulsive control of the atomic dipole response in the time and frequency domain*. PhD thesis, Ruperto-Carola-University of Heidelberg, 2016. (Cited on page 3, 27, 28, 29)

[60] Veit Stooß. *Strong-Field Spectroscopy: From Absorption to Time-Resolved Dynamics in Strong Fields*. PhD thesis, Ruperto-Carola-University of Heidelberg, 2018. (Cited on page 3, 22, 26, 49)

[61] Paul Birk. *The Dipole Response of an Ionization Threshold within Ultrashort and Strong Fields*. PhD thesis, Ruperto-Carola-University of Heidelberg, 2020. (Cited on page 3, 19, 22, 38, 49)

[62] Franz X. Kärtner, Erich P. Ippen, and Steven T. Cundiff. Femtosecond Laser Development. In *Femtosecond Optical Frequency Comb: Principle, Operation, and Applications*, pages 54–77. Kluwer Academic Publishers, 2006. (Cited on page 5)

[63] Jie Li, Xiaoming Ren, Yanchun Yin, Kun Zhao, Andrew Chew, Yan Cheng, Eric Cunningham, Yang Wang, Shuyuan Hu, Yi Wu, Michael Chini, and Zenghu Chang. 53-attosecond X-ray pulses reach the carbon K-edge. *Nature Communications*, 8(1), 2017. (Cited on page 5, 32)

[64] Thomas Gaumnitz, Arohi Jain, Yoann Pertot, Martin Huppert, Inga Jordan, Fernando Ardana-Lamas, and Hans Jakob Wörner. Streaking of 43-attosecond soft-X-ray pulses generated by a passively CEP-stable mid-infrared driver. *Optics Express*, 25(22):27506, 2017. (Cited on page 5, 32)

[65] Jean-Claude Diels and Wolfgang Rudolph. *Ultrashort laser pulse phenomena*. Elsevier, 2006. (Cited on page 5)

[66] Joseph W Goodman. *Introduction to Fourier optics*. Roberts and Company Publishers, 2005. (Cited on page 7)

[67] L. V. Keldysh. Ionization in the field of a strong electromagnetic wave. *Soviet Physics JETP*, 1965. (Cited on page 11, 103)

[68] M. V. Fedorov. L. V. Keldysh's "Ionization in the Field of a Strong Electromagnetic Wave" and modern physics of atomic interaction with a strong laser field. *Journal of Experimental and Theoretical Physics*, 122(3):449–455, 2016. (Cited on page 12)

[69] P. Eckle, A. N. Pfeiffer, C. Cirelli, A. Staudte, R. Dörner, H. G. Muller, M. Büttiker, and U. Keller. Attosecond ionization and tunneling delay time measurements in helium. *Science*, 322(5907):1525–1529, 2008. (Cited on page 12)

[70] Alexandra S Landsman, Matthias Weger, Jochen Maurer, Robert Boge, André Ludwig, Sebastian Heuser, Claudio Cirelli, Lukas Gallmann, and Ursula Keller. Ultrafast resolution of tunneling delay time. *Optica*, 1(5):343, 2014. (Cited on page 12)

[71] Michael Chini, Baozhen Zhao, He Wang, Yan Cheng, Suxing Hu, and Zenghu Chang. Sub-cycle AC Stark Shift. In *Conference on Lasers and Electro-Optics 2012*, page QTu3H.7, Washington, D.C., 2012. OSA. (Cited on page 12, 86)

[72] Michael Chini, Xiaowei Wang, Yan Cheng, Yi Wu, Di Zhao, Dmitry A. Telnov, Shih I. Chu, and Zenghu Chang. Sub-cycle oscillations in virtual states brought to light. *Scientific Reports*, 3(1):1–6, 2013. (Cited on page 12)

[73] Alexander Blättermann, Christian Ott, Andreas Kaldun, Thomas Ding, Veit Stooß, Martin Laux, Marc Rebholz, and Thomas Pfeifer. In situ characterization of few-cycle laser pulses in transient absorption spectroscopy. *Optics Letters*, 40(15):3464, 2015. (Cited on page 12, 29)

[74] N B Delone and Vladimir P Krainov. AC Stark shift of atomic energy levels. *Physics-Uspekhi*, 42 (7):669–687, 1999. (Cited on page 12)

[75] J Mitroy, M S Safronova, and Charles W Clark. Theory and applications of atomic and ionic polarizabilities. *Journal of Physics B: Atomic, Molecular and Optical Physics*, 43(20):202001, 2010. (Cited on page 12, 86)

[76] S. G. Porsev, M. S. Safronova, U. I. Safronova, and M. G. Kozlov. Multipolar Polarizabilities and Hyperpolarizabilities in the Sr Optical Lattice Clock. *Physical Review Letters*, 120(6):063204, 2018. (Cited on page 13)

[77] AM Perelomov, VS Popov, and MV Terent'ev. Ionization of atoms in an alternating electric field. *Sov. Phys. JETP*, 23(5):924–934, 1966. (Cited on page 13)

[78] F. H.M. Faisal. Multiple absorption of laser photons by atoms. *Journal of Physics B: Atomic and Molecular Physics*, 1973. (Cited on page 13)

[79] Howard R. Reiss. Effect of an intense electromagnetic field on a weakly bound system. *Physical Review A*, 1980. (Cited on page 13)

[80] Gennady L. Yudin and Misha Yu Ivanov. Nonadiabatic tunnel ionization: Looking inside a laser cycle. *Physical Review A - Atomic, Molecular, and Optical Physics*, 64(1):4, 2001. (Cited on page 13)

[81] Gennady L. Yudin and Misha Yu Ivanov. Physics of correlated double ionization of atoms in intense laser fields: Quasistatic tunneling limit. *Physical Review A - Atomic, Molecular, and Optical Physics*, 63(3):1–14, 2001. (Cited on page 13)

[82] S. Augst, D. Strickland, D. D. Meyerhofer, S. L. Chin, and J. H. Eberly. Tunneling ionization of noble gases in a high-intensity laser field. *Physical Review Letters*, 63(20):2212–2215, 1989. (Cited on page 13)

[83] S. Augst, D. D. Meyerhofer, D. Strickland, and S. L. Chint. Laser ionization of noble gases by Coulomb-barrier suppression. *Journal of the Optical Society of America B*, 8(4):858, 1991. (Cited on page 13)

[84] V. P. Krainov. Ionization rates and energy and angular distributions at the barrier-suppression ionization of complex atoms and atomic ions. *Journal of the Optical Society of America B*, 14(2):425, 1997. (Cited on page 13)

[85] Vladimir S Popov. Tunnel and multiphoton ionization of atoms and ions in a strong laser field (Keldysh theory). *Physics-Uspekhi*, 2004. (Cited on page 13)

[86] I. A. Ivanov, C. Hofmann, L. Ortmann, A. S. Landsman, Chang Hee Nam, and Kyung Taec Kim. Instantaneous ionization rate as a functional derivative. *Communications Physics*, 1(1):1–9, 2018. (Cited on page 14)

[87] M. Uiberacker, Th Uphues, M. Schultze, A. J. Verhoef, V. Yakovlev, M. F. Kling, J. Rauschenberger, N. M. Kabachnik, H. Schröder, M. Lezius, K. L. Kompa, H. G. Muller, M. J.J. Vrakking, S. Hendel, U. Kleineberg, U. Heinzmann, M. Drescher, and F. Krausz. Attosecond real-time observation of electron tunnelling in atoms. *Nature*, 446(7136):627–632, 2007. (Cited on page 15, 101, 103)

[88] Olga Smirnova, Michael Spanner, and Misha Ivanov. Coulomb and polarization effects in sub-cycle dynamics of strong-field ionization. *Journal of Physics B: Atomic, Molecular and Optical Physics*, 39 (13):S307, 2006. (Cited on page 15)

[89] Mette B Gaarde, Jennifer L Tate, and Kenneth J Schafer. Macroscopic aspects of attosecond pulse generation. *Journal of Physics B: Atomic, Molecular and Optical Physics*, 41(13):132001, 2008. (Cited on page 15, 16)

[90] C. M. Heyl, C. L. Arnold, A. Couairon, and A. L'Huillier. Introduction to macroscopic power scaling principles for high-order harmonic generation. *Journal of Physics B: Atomic, Molecular and Optical Physics*, 50(1):013001, 2017. (Cited on page 17)

[91] Stefan Pabst, Arina Sytcheva, Antoine Moulet, Adrian Wirth, Eleftherios Goulielmakis, and Robin Santra. Theory of attosecond transient-absorption spectroscopy of krypton for overlapping pump and probe pulses. *Physical Review A - Atomic, Molecular, and Optical Physics*, 86(6):063411, 2012. (Cited on page 18, 29, 69, 77, 78, 95, 101)

[92] Lev Davidovich Landau and Evgenii Mikhailovich Lifshitz. *Quantum mechanics: non-relativistic theory*, volume 3. Elsevier, 2013. (Cited on page 20)

[93] Torsten Fließbach. *Quantenmechanik*. Springer, 1991. (Cited on page 20)

[94] Ugo Fano. Sullo spettro di assorbimento dei gas nobili presso il limite dello spettro d'arco. *Il Nuovo Cimento*, 12(3):154–161, 1935. (Cited on page 20, 86)

[95] Ugo Fano, Guido Pupillo, Alberto Zannoni, and Charles W. Clark. On the absorption spectrum of noble gases at the arc spectrum limit. *Journal of Research of the National Institute of Standards and Technology*, 110(6):583–587, 2005. (Cited on page 20)

[96] U. Fano. Effects of configuration interaction on intensities and phase shifts, 1961. (Cited on page 20, 21, 86)

[97] P. Lambropoulos and P. Zoller. Autoionizing states in strong laser fields. *Physical Review A*, 24(1): 379–397, 1981. (Cited on page 20)

[98] Tobias Heldt. Strong-field-driven electron dynamics near an ionization threshold. Master's thesis, Ruperto-Carola-University of Heidelberg, 2020. (Cited on page 26, 47)

[99] Christian Ott, Andreas Kaldun, Philipp Raith, Kristina Meyer, Martin Laux, Jörg Evers, Christoph H. Keitel, Chris H. Greene, and Thomas Pfeifer. Lorentz Meets Fano in Spectral Line Shapes: A Universal Phase and Its Laser Control. *Science*, 340(6133):716–720, 2013. (Cited on page 28, 69, 77)

[100] J. B. West. Photoionization of atomic ions. *Journal of Physics B: Atomic, Molecular and Optical Physics*, 34(18):45–91, 2001. (Cited on page 29)

[101] Henrik Kjeldsen. Photoionization cross sections of atomic ions from merged-beam experiments. *Journal of Physics B: Atomic, Molecular and Optical Physics*, 39(21):R325–R377, 2006. (Cited on page 29)

[102] D. A. Verner, G. J. Ferland, K. T. Korista, and D. G. Yakovlev. Atomic Data for Astrophysics. II. New Analytic FITS for Photoionization Cross Sections of Atoms and Ions. *The Astrophysical Journal*, 465:487, 1996. (Cited on page 29, 75)

[103] Zikri Altun, Mickey Kutzner, and Hugh P. Kelly. Photoionization of the 4d subshell of xenon. *Physical Review A*, 37(12):4671–4678, 1988. (Cited on page 29)

[104] J.-M. Bizau, J.-M. Esteva, D. Cubaynes, F. J. Wuilleumier, C. Blancard, A. Compant La Fontaine, C. Couillaud, J. Lachkar, R. Marmoret, C. Rémond, J. Bruneau, D. Hitz, P. Ludwig, and M. Delaunay. Photoionization of Highly Charged Ions Using an ECR Ion Source and Undulator Radiation. *Physical Review Letters*, 84(3):435–438, 2000. (Cited on page 29)

[105] Yoh Itoh, Akira Ito, Masashi Kitajima, Tetsuo Koizumi, Takao M Kojima, Hiroshi Sakai, Mutsumi Sano, and Naoki Watanabe. Absolute photoionization cross section measurements of Xe+ ions in the 4d threshold energy region. *Journal of Physics B: Atomic, Molecular and Optical Physics*, 34(17): 3493, 2001. (Cited on page 29)

[106] J M Bizau, C Blancard, M Coreno, D Cubaynes, C Dehon, N El Hassan, F Folkmann, M F Gharaibeh, A Giuliani, J Lemaire, A R Milosavljević, C Nicolas, and R Thissen. Photoionization study of Kr+ and Xe+ ions with the combined use of a merged-beam set-up and an ion trap. *Journal of Physics B: Atomic, Molecular and Optical Physics*, 44(5):055205, 2011. (Cited on page 29)

[107] S Schippers, S Ricz, T Buhr, et al. Absolute cross sections for photoionization of Xe^{q+} ions ($1 \leq q \leq 5$) at the 3d ionization threshold. *Journal of Physics B: Atomic, Molecular and Optical Physics*, 47(11):115602, 2014. (Cited on page 29)

[108] D. L. Ederer. Photoionization of the 4d Electrons in Xenon. *Physical Review Letters*, 13(25):760–762, 1964. (Cited on page 29)

[109] H Kjeldsen, P Andersen, F Folkmann, J E Hansen, M Kitajima, and T Andersen. Experimental study of 4f wavefunction contraction: 4d-photoionization of low-charged ions of I, Xe, Cs and Ba. *Journal of Physics B: Atomic, Molecular and Optical Physics*, 35(13):2845, 2002. (Cited on page 29)

[110] P. Andersen, T. Andersen, F. Folkmann, K. Ivanov V, H. Kjeldsen, and J. B. West. Absolute cross sections for the photoionization of 4d electrons in Xe + and Xe 2+ ions. *Journal of Physics B: Atomic, Molecular and Optical Physics*, 34(10):2009–2019, 2001. (Cited on page 29, 30, 57, 63, 69, 78, 79)

[111] M. Sano, Y. Itoh, T. Koizumi, T. M. Kojima, S. D. Kravis, M. Oura, T. Sekioka, N. Watanabe, Y. Awaya, and F. Koike. Photoionization of 4d-electrons in singly charged Xe ions. *Journal of Physics B: Atomic, Molecular and Optical Physics*, 29(22):5305–5313, 1996. (Cited on page 29)

[112] T Koizumi, Y Awaya, A Fujino, Y Itoh, M Kitajima, T M Kojima, M Oura, R Okuma, M Sano, T Seikioka, N Watanabe, and F Koike. 4d Photoionization of multiply charged Xe^{q+}(q= 1-3) ions. *Physica Scripta*, T73:131–132, 1997. (Cited on page 29)

[113] Naoki Watanabe, Yohko Awaya, Atsushi Fujino, Yoh Itoh, Masashi Kitajima, Takao M. Kojima, Masaki Oura, Ryuji Okuma, Mutsumi Sano, Tsuguhisa Sekioka, and Tetsuo Koizumi. Photoion-yield spectra of in the 4d-threshold energy region. *Journal of Physics B: Atomic, Molecular and Optical Physics*, 31(18):4137–4141, 1998. (Cited on page 29)

[114] J. M. Bizau, C. Blancard, D. Cubaynes, F. Folkmann, J. P. Champeaux, J. L. Lemaire, and F. J. Wuilleumier. Absolute photoionization cross sections along the Xe isonuclear sequence: Xe3+ to Xe6+. *Physical Review A - Atomic, Molecular, and Optical Physics*, 73(2):022718, 2006. (Cited on page 29)

[115] D. L. Ederer and M. Manalis. Photoabsorption of the 4d electrons in xenon. *Journal of the Optical Society of America*, 65(6):634, 1975. (Cited on page 29, 63, 65, 69, 89)

[116] S Masui, E Shigemasa, A Yagishita, and I A Sellin. New measurements of the widths of the Xe 4d levels. *Journal of Physics B: Atomic, Molecular and Optical Physics*, 28(20):4529, 1995. (Cited on page 29)

[117] Birgitta Bernhardt, Annelise R. Beck, Xuan Li, Erika R. Warrick, M. Justine Bell, Daniel J. Haxton, C. William McCurdy, Daniel M. Neumark, and Stephen R. Leone. High-spectral-resolution attosecond absorption spectroscopy of autoionization in xenon. *Physical Review A - Atomic, Molecular, and Optical Physics*, 89(2), 2014. (Cited on page 30)

[118] Xuan Li, Birgitta Bernhardt, Annelise R. Beck, Erika R. Warrick, Adrian N. Pfeiffer, M. Justine Bell, Daniel J. Haxton, C. William McCurdy, Daniel M. Neumark, and Stephen R. Leone. Investigation of coupling mechanisms in attosecond transient absorption of autoionizing states: Comparison of theory and experiment in xenon. *Journal of Physics B: Atomic, Molecular and Optical Physics*, 48 (12), 2015. (Cited on page 30)

[119] Ming Fu Lin, Adrian N. Pfeiffer, Daniel M. Neumark, Stephen R. Leone, and Oliver Gessner. Strong-field induced XUV transmission and multiplet splitting in 4dˆ{-1}6p core-excited Xe studied by femtosecond XUV transient absorption spectroscopy. *Journal of Chemical Physics*, 137(24):244305, 2012. (Cited on page 30, 68)

[120] Yuki Kobayashi, Henry Timmers, Mazyar Sabbar, Stephen R. Leone, and Daniel M. Neumark. Attosecond transient-absorption dynamics of xenon core-excited states in a strong driving field. *Physical Review A*, 95(3), 2017. (Cited on page 30, 46, 57)

[121] M Anand, Stefan Pabst, Ojoon Kwon, and Dong Eon Kim. Attosecond counter-rotating-wave effect in xenon driven by strong fields. *Physical Review A*, 95(5):053420, 2017. (Cited on page 30)

[122] E. Goulielmakis, M. Uiberacker, R. Kienberger, A. Baltuska, V. Yakovlev, A. Scrinzi, Th Westerwalbesloh, U. Kleineberg, U. Heinzmann, M. Drescher, and F. Krausz. Direct measurement of light waves. *Science*, 305(5688):1267–1269, 2004. (Cited on page 32)

[123] Y. Mairesse and F. Quéré. Frequency-resolved optical gating for complete reconstruction of attosecond bursts. *Physical Review A - Atomic, Molecular, and Optical Physics*, 71(1):1–4, 2005. (Cited on page 32, 54)

[124] J. Gagnon, Eleftherios Goulielmakis, and V. S. Yakovlev. The accurate FROG characterization of attosecond pulses from streaking measurements. *Applied Physics B: Lasers and Optics*, 92(1):25–32, 2008. (Cited on page 32)

[125] Michael Chini, Steve Gilbertson, Sabih D Khan, and Zenghu Chang. Characterizing ultrabroadband attosecond lasers. *Optics express*, 18(12):13006–13016, 2010. (Cited on page 32)

[126] Michael Chini, Kun Zhao, and Zenghu Chang. The generation, characterization and applications of broadband isolated attosecond pulses. *Nature Photonics*, 8(3):178–186, 2014. (Cited on page 32, 44)

[127] M. Lucchini, M.H. Brügmann, A. Ludwig, L. Gallmann, U. Keller, and T. Feurer. Ptychographic reconstruction of attosecond pulses. *Optics Express*, 23(23):29502, 2015. (Cited on page 32)

[128] G. Sansone, E. Benedetti, F. Calegari, C. Vozzi, L. Avaldi, R. Flammini, L. Poletto, P. Villoresi, C. Altucci, R. Velotta, S. Stagira, S. De Silvestri, and M. Nisoli. Isolated single-cycle attosecond pulses. *Science*, 314(5798):443–446, 2006. (Cited on page 32)

[129] E. Goulielmakis, M. Schultze, M. Hofstetter, V. S. Yakovlev, J. Gagnon, M. Uiberacker, A. L. Aquila, E. M. Gullikson, D. T. Attwood, R. Kienberger, F. Krausz, and U. Kleineberg. Single-cycle nonlinear optics. *Science*, 2008. (Cited on page 32)

[130] Kun Zhao, Qi Zhang, Michael Chini, Yi Wu, Xiaowei Wang, and Zenghu Chang. Tailoring a 67 attosecond pulse through advantageous phase-mismatch. *Optics Letters*, 37(18):3891, 2012. (Cited on page 32)

[131] M. Schultze, M Fiess, N. Karpowicz, J. Gagnon, M. Korbman, M. Hofstetter, S. Neppl, A. L. Cavalieri, Y. Komninos, Th Mercouris, C. A. Nicolaides, R. Pazourek, S. Nagele, J. Feist, J. Burgdorfer, A. M. Azzeer, R. Ernstorfer, R. Kienberger, U. Kleineberg, Eleftherios Goulielmakis, F. Krausz, and V. S. Yakovlev. Delay in Photoemission. *Science*, 328(5986):1658–1662, 2010. (Cited on page 33, 54)

[132] A. L. Cavalieri, N. Müller, Th Uphues, V. S. Yakovlev, A. Baltuška, B. Horvath, B. Schmidt, L. Blümel, R. Holzwarth, S. Hendel, M. Drescher, U. Kleineberg, P. M. Echenique, R. Kienberger, F. Krausz, and U. Heinzmann. Attosecond spectroscopy in condensed matter. *Nature*, 449(7165):1029–1032, 2007. (Cited on page 33)

[133] M. Ossiander, F. Siegrist, V. Shirvanyan, R. Pazourek, A. Sommer, T. Latka, A. Guggenmos, S. Nagele, J. Feist, J. Burgdörfer, R. Kienberger, and M. Schultze. Attosecond correlation dynamics. *Nature Physics*, 13(3):280–285, 2017. (Cited on page 33)

[134] K. Klünder, J. M. Dahlström, M. Gisselbrecht, T. Fordell, M. Swoboda, D. Guénot, P. Johnsson, J. Caillat, J. Mauritsson, A. Maquet, R. Taïeb, and A. L'Huillier. Probing single-photon ionization on the attosecond time scale. *Physical Review Letters*, 106(14):143002, 2011. (Cited on page 33)

[135] D. Guénot, K. Klünder, C. L. Arnold, D. Kroon, J. M. Dahlström, M. Miranda, T. Fordell, M. Gisselbrecht, P. Johnsson, J. Mauritsson, E. Lindroth, A. Maquet, R. Taïeb, A. L'Huillier, and A. S. Kheifets. Photoemission-time-delay measurements and calculations close to the 3s-ionization-cross-section minimum in Ar. *Physical Review A - Atomic, Molecular, and Optical Physics*, 85(5):1–8, 2012. (Cited on page 33, 71)

[136] D Guénot, D Kroon, E Balogh, E W Larsen, M Kotur, M Miranda, T Fordell, P Johnsson, J Mauritsson, M Gisselbrecht, K Varjù, C L Arnold, T Carette, A S Kheifets, E Lindroth, A L'Huillier, and J M Dahlström. Measurements of relative photoemission time delays in noble gas atoms. *Journal of Physics B: Atomic, Molecular and Optical Physics*, 47(24):245602, 2014. (Cited on page 33)

[137] M. Isinger, D. Busto, S. Mikaelsson, S. Zhong, C. Guo, P. Salières, C. L. Arnold, A. L'Huillier, and M. Gisselbrecht. Accuracy and precision of the RABBIT technique. *Philosophical Transactions of the Royal Society A: Mathematical, Physical and Engineering Sciences*, 377(2145):20170475, 2019. (Cited on page 33)

[138] Sebastian Heuser, Álvaro Jiménez Galán, Claudio Cirelli, Carlos Marante, Mazyar Sabbar, Robert Boge, Matteo Lucchini, Lukas Gallmann, Igor Ivanov, Anatoli S. Kheifets, J. Marcus Dahlström, Eva Lindroth, Luca Argenti, Fernando Martín, and Ursula Keller. Angular dependence of photoemission time delay in helium. *Physical Review A*, 94(6), 2016. (Cited on page 33)

[139] M. Isinger, R. J. Squibb, D. Busto, S. Zhong, A. Harth, D. Kroon, S. Nandi, C. L. Arnold, M. Miranda, J. M. Dahlström, E. Lindroth, R. Feifel, M. Gisselbrecht, and A. L'Huillier. Photoionization in the time and frequency domain. *Science*, 358(6365):893–896, 2017. (Cited on page 33)

[140] I. Jordan, M. Huppert, Stefan Pabst, A. S. Kheifets, D. Baykusheva, and H. J. Wörner. Spin-orbit delays in photoemission. *Physical Review A*, 95(1):013404, 2017. (Cited on page 33)

[141] Arohi Jain, Thomas Gaumnitz, Alexander Bray, Anatoli Kheifets, and Hans Jakob Wörner. Photoionization delays in xenon using single-shot referencing in the collinear back-focusing geometry. *Optics Letters*, 43(18):4510, 2018. (Cited on page 33)

[142] Fabian Lücking, Andreas Assion, Alexander Apolonski, Ferenc Krausz, and Günter Steinmeyer. Long-term carrier-envelope-phase-stable few-cycle pulses by use of the feed-forward method. *Optics Letters*, 37(11):2076, 2012. (Cited on page 35)

[143] Francisco Silva, Benjamín Alonso, Warein Holgado, Rosa Romero, Julio San Román, Enrique Conejero Jarque, Hans Koop, Vladimir Pervak, Helder Crespo, and Íñigo J. Sola. Strategies for achieving intense single-cycle pulses with in-line post-compression setups. *Optics Letters*, 43(2):337, 2018. (Cited on page 37)

[144] M. Nisoli, S. De Silvestri, and O. Svelto. Generation of high energy 10 fs pulses by a new pulse compression technique. *Applied Physics Letters*, 68(20):2793–2795, 1996. (Cited on page 37)

[145] M. Nisoli, S. De Silvestri, O. Svelto, R. Szipöcs, K. Ferencz, Ch. Spielmann, S. Sartania, and F. Krausz. Compression of high-energy laser pulses below 5 fs. *Optics Letters*, 22(8):522, 1997. (Cited on page 37)

[146] Tamas Nagy, Michael Forster, and Peter Simon. Flexible hollow fiber for pulse compressors. *Applied Optics*, 47(18):3264–3268, 2008. (Cited on page 37)

[147] A. Trabattoni, T. Oksenhendler, H. Jousselin, G. Tempea, S. De Silvestri, G. Sansone, F. Calegari, and M. Nisoli. Self-referenced spectral interferometry for single-shot measurement of sub-5-fs pulses. *Review of Scientific Instruments*, 86(11):113106, 2015. (Cited on page 37)

[148] Vahe Shirvanyan. Generation of sub-4-fs, mj pulses via hollow-core fiber nonlinear pulse compression by the conjugate pressure-gradient method. Master's thesis, Technische Universität München, 2015. (Cited on page 37)

[149] Light Conversion. Optics Toolbox. Available at: `http://toolbox.lightcon.com/`, 2021. (Cited on page 39)

[150] Francisco Silva, Miguel Miranda, Benjamín Alonso, Jens Rauschenberger, Vladimir Pervak, and Helder Crespo. Simultaneous compression, characterization and phase stabilization of GW-level 14 cycle VIS-NIR femtosecond pulses using a single dispersion-scan setup. *Optics Express*, 22(9): 10181, 2014. (Cited on page 39, 40)

[151] Henry Timmers, Yuki Kobayashi, Kristina F Chang, Maurizio Reduzzi, Daniel M Neumark, and Stephen R Leone. Generating high-contrast, near single-cycle waveforms with third-order dispersion compensation. *Optics Letters*, 42(4):811, 2017. (Cited on page 39)

[152] Rick Trebino and Daniel J Kane. Using phase retrieval to measure the intensity and phase of ultrashort pulses: frequency-resolved optical gating. *JOSA A*, 10(5):1101–1111, 1993. (Cited on page 40)

[153] Daniel J Kane and Rick Trebino. Characterization of arbitrary femtosecond pulses using frequency-resolved optical gating. *Quantum Electronics, IEEE Journal of*, 29(2):571–579, 1993. (Cited on page 40)

[154] Vadim V. Lozovoy, Igor Pastirk, and Marcos Dantus. Multiphoton intrapulse interference IV Ultrashort laser pulse spectral phase characterization and compensation. *Optics Letters*, 29(7):775, 2004. (Cited on page 40)

[155] J-H Chung and A M Weiner. Ambuguity of Ultrashort Pulses Retrieved From the Intensity Autocorrelation and Power Spectrum Traces. *Selected Topics in Quantum Electronics, IEEE Journal on*, 7 (4):656–666, 2002. (Cited on page 40)

[156] Rick Trebino. *Frequency-resolved optical gating: the measurement of ultrashort laser pulses*. Springer Science & Business Media, 2012. (Cited on page 40)

[157] Kenneth W DeLong and Rick Trebino. Improved ultrashort pulse-retrieval algorithm for frequency-resolved optical gating. *JOSA A*, 11(9):2429–2437, 1994. (Cited on page 40)

[158] J. W. Nicholson, F. G. Omenetto, D. J. Funk, and A. J. Taylor. Evolving FROGS: phase retrieval from frequency-resolved optical gating measurements by use of genetic algorithms. *Optics Letters*, 24 (7):490, 1999. (Cited on page 40)

[159] Miguel Miranda, Cord L Arnold, Thomas Fordell, Francisco Silva, Benjamín Alonso, Rosa Weigand, Anne L'Huillier, and Helder Crespo. Characterization of broadband few-cycle laser pulses with the d-scan technique. *Optics Express*, 20(17):18732, 2012. (Cited on page 40)

[160] Miguel Miranda, Thomas Fordell, Cord L Arnold, Anne L'Huillier, and Helder Crespo. Simultaneous compression and characterization of ultrashort laser pulses using chirped mirrors and glass wedges. *Optics Express*, 20(1):688, 2012. (Cited on page 40)

[161] Benjamín Alonso, Miguel Miranda, Íñigo J. Sola, and Helder Crespo. Spatiotemporal characterization of few-cycle laser pulses. *Optics Express*, 20(16):17880, 2012. (Cited on page 40)

[162] Mathias Hoffmann, Tamas Nagy, Thomas Willemsen, Marco Jupé, Detlev Ristau, and Uwe Morgner. Pulse characterization by THG d-scan in absorbing nonlinear media. *Optics Express*, 22(5):5234, 2014. (Cited on page 40)

[163] Ayhan Tajalli, Bruno Chanteau, Martin Kretschmar, Heiko.G. Kurz, David Zuber, Milutin Kovačev, Uwe Morgner, and Tamas Nagy. Few-cycle optical pulse characterization via cross-polarized wave generation dispersion scan technique. *Optics Letters*, 41(22):5246, 2016. (Cited on page 40)

[164] Ayhan Tajalli Seifi, Marie Ouille, Aline Vernier, Frederik Bohle, Esmerando Escoto, Sven Kleinert, Rosa Romero, Janos Csontos, Uwe Morgner, Gunter Steinmeyer, Helder Crespo, Rodrigo Lopez-Martens, and Tamas Nagy. Propagation effects in the characterization of 1.5-cycle pulses by XPW dispersion scan. *IEEE Journal of Selected Topics in Quantum Electronics*, 2018. (Cited on page 40)

[165] Miguel Canhota, Francisco Silva, Rosa Weigand, and Helder M. Crespo. Inline self-diffraction dispersion-scan of over octave-spanning pulses in the single-cycle regime. *Optics Letters*, 42(15): 3048, 2017. (Cited on page 40)

[166] Nils C. Geib, Matthias Zilk, Thomas Pertsch, and Falk Eilenberger. Common pulse retrieval algorithm: a fast and universal method to retrieve ultrashort pulses. *Optica*, 6(4):495, 2019. (Cited on page 40)

[167] Miguel Miranda, João Penedones, Chen Guo, Anne Harth, Maïté Louisy, Lana Neoričić, Anne L'Huillier, and Cord L. Arnold. Fast iterative retrieval algorithm for ultrashort pulse characterization using dispersion scans. *Journal of the Optical Society of America B*, 34(1):190, 2017. (Cited on page 40)

[168] Esmerando Escoto, Ayhan Tajalli, Tamas Nagy, and Günter Steinmeyer. Advanced phase retrieval for dispersion scan: a comparative study. *Journal of the Optical Society of America B*, 35(1):8, 2018. (Cited on page 40)

[169] Sven Kleinert, Ayhan Tajalli, Tamas Nagy, and Uwe Morgner. Rapid phase retrieval of ultrashort pulses from dispersion scan traces using deep neural networks. *Optics Letters*, 44(4):979, 2019. (Cited on page 40)

[170] Miguel Miranda, Francisco Silva, Lana Neoričić, Chen Guo, Vladimir Pervak, Miguel Canhota, Ana S. Silva, Íñigo J. Sola, Rosa Romero, Paulo T. Guerreiro, Anne L'Huillier, Cord L. Arnold, and Helder Crespo. All-optical measurement of the complete waveform of octave-spanning ultrashort light pulses. *Optics Letters*, 44(2):191, 2019. (Cited on page 40)

[171] Maximilian Hartmann. Characterization of few-cycle laser pulses. Master's thesis, Ruperto-Carola-University of Heidelberg, 2016. (Cited on page 40, 49)

[172] Felix Herzog. Design and implementation of a gas jet array for ultrafast time-resolved absorption spectroscopy. Bachelor's thesis, Ruperto-Carola-University of Heidelberg, 2019. (Cited on page 41, 42, 52, 64)

[173] Center for X-Ray Optics (CXRO). X-ray transmission of gases and solids. URL: `https://henke.lbl.gov/optical_constants/`, 2021. (Cited on page 42, 47)

[174] Lukas Endres. Polarisation assisted amplitude gating. Bachelor's thesis, Ruperto-Carola-University of Heidelberg, 2017. (Cited on page 45, 63)

[175] Henry Timmers, Mazyar Sabbar, Yuki Kobayashi, Daniel M. Neumark, and Stephen R. Leone. Polarization assisted amplitude gating as a route to tunable, high-contrast single attosecond pulses. *Optica*, 3(7):707, 2016. (Cited on page 45)

[176] Marc Rebholz. Design and construction of an experimental setup for multidimensional spectroscopy in the xuv/ soft-x-ray spectral region. Master's thesis, Ruperto-Carola-University of Heidelberg, 2015. (Cited on page 46)

[177] M. Sabbar, S. Heuser, R. Boge, M. Lucchini, L. Gallmann, C. Cirelli, and U. Keller. Combining attosecond XUV pulses with coincidence spectroscopy. *Review of Scientific Instruments*, 85(10), 2014. (Cited on page 47)

[178] Sabine Rockenstein. Active carrier-envelope phase stabilisation of ultrashort laser pulses. Bachelor's thesis, Ruperto-Carola-University of Heidelberg, 2019. (Cited on page 48)

[179] Seth L. Cousin, Nicola Di Palo, Bárbara Buades, Stephan M. Teichmann, M. Reduzzi, M. Devetta, A. Kheifets, G. Sansone, and Jens Biegert. Attosecond streaking in the water window: A new regime of attosecond pulse characterization. *Physical Review X*, 7(4):041030, 2017. (Cited on page 48, 53, 54)

[180] Ximao Feng, Steve Gilbertson, Sabih D Khan, Michael Chini, Yi Wu, Kevin Carnes, and Zenghu Chang. Calibration of electron spectrometer resolution in attosecond streak camera. *Optics express*, 18(2):1316–1322, 2010. (Cited on page 50)

[181] Wolfgang Demtröder. *Experimentalphysik 3: Atome, Moleküle und Festkörper*. Springer-Verlag, 2010. (Cited on page 51)

[182] Fabian Kaap. Plasma-induzierte Blauverschiebung während der Erzeugung Hoher Harmonischer. Bachelor's thesis, Ruperto-Carola-University of Heidelberg, 2018. (Cited on page 51, 89)

[183] Daniel Irimia, Dimitar Dobrikov, Rob Kortekaas, Han Voet, Daan A. Van Den Ende, Wilhelm A. Groen, and Maurice H.M. Janssen. A short pulse (7 μs FWHM) and high repetition rate (dc-5kHz) cantilever piezovalve for pulsed atomic and molecular beams. *Review of Scientific Instruments*, 80 (11), 2009. (Cited on page 52)

[184] U. Even. The Even-Lavie valve as a source for high intensity supersonic beam. *EPJ Techniques and Instrumentation*, 2(1):1–22, 2015. (Cited on page 52)

[185] Rodrigo López-Martens, Katalin Varjú, Per Johnsson, Johan Mauritsson, Yann Mairesse, Pascal Salières, Mette B. Gaarde, Kenneth J. Schafer, Anders Persson, Sune Svanberg, Claes Göran Wahlström, and Anne L'Huillier. Amplitude and phase control of attosecond light pulses. *Physical Review Letters*, 94(3):033001, 2005. (Cited on page 54, 68, 71)

[186] Mark Mero, Fabio Frassetto, Paolo Villoresi, Luca Poletto, and Katalin Varjú. Compression methods for XUV attosecond pulses. *Optics Express*, 19(23):23420, 2011. (Cited on page 54, 71)

[187] A. Kramida, Yu. Ralchenko, J. Reader, and NIST ASD Team. NIST Atomic Spectra Database (ver. 5.7.1), [Online]. Available at: `https://physics.nist.gov/asd` [2020, August 4]. National Institute of Standards and Technology, Gaithersburg, MD., 2019. (Cited on page 55)

[188] Annelise R. Beck, Birgitta Bernhardt, Erika R. Warrick, Mengxi Wu, Shaohao Chen, Mette B. Gaarde, Kenneth J. Schafer, Daniel M. Neumark, and Stephen R. Leone. Attosecond transient absorption probing of electronic superpositions of bound states in neon: detection of quantum beats. *New Journal of Physics*, 16(11):113016, 2014. (Cited on page 56, 76, 77)

[189] Mikhail Volkov, Justinas Pupeikis, Christopher R. Phillips, Fabian Schlaepfer, Lukas Gallmann, and Ursula Keller. Reduction of laser-intensity-correlated noise in high-harmonic generation. *Optics Express*, 27(6):7886, 2019. (Cited on page 60)

[190] Romain Géneaux, Hung-Tzu Chang, Adam M. Schwartzberg, and Hugo J. B. Marroux. Source noise suppression in attosecond transient absorption spectroscopy by edge-pixel referencing. *Optics Express*, 29(2):951, 2021. (Cited on page 60, 61, 63)

[191] Shaohao Chen, M. Justine Bell, Annelise R. Beck, Hiroki Mashiko, Mengxi Wu, Adrian N. Pfeiffer, Mette B. Gaarde, Daniel M. Neumark, Stephen R. Leone, and Kenneth J. Schafer. Light-induced states in attosecond transient absorption spectra of laser-dressed helium. *Physical Review A - Atomic, Molecular, and Optical Physics*, 86(6):1–5, 2012. (Cited on page 67, 77)

[192] Alexander Magunia, Lennart Aufleger, Thomas Ding, Patrick Rupprecht, Marc Rebholz, Christian Ott, and Thomas Pfeifer. Bound-State Electron Dynamics Driven by Near-Resonantly Detuned Intense and Ultrashort Pulsed XUV Fields. *Applied Sciences*, 10(18):6153, 2020. (Cited on page 75)

[193] Erik R. Hosler and Stephen R. Leone. Characterization of vibrational wave packets by core-level high-harmonic transient absorption spectroscopy. *Physical Review A - Atomic, Molecular, and Optical Physics*, 88(2):023420, 2013. (Cited on page 75)

[194] Zhengrong Wei, Jialin Li, Lin Wang, Soo Teck See, Mark Hyunpong Jhon, Yingfeng Zhang, Fan Shi, Minghui Yang, and Zhi Heng Loh. Elucidating the origins of multimode vibrational coherences of polyatomic molecules induced by intense laser fields. *Nature Communications*, 8(1):1–7, 2017. (Cited on page 75)

[195] Olga Smirnova, Yann Mairesse, Serguei Patchkovskii, Nirit Dudovich, David Villeneuve, Paul Corkum, and Misha Yu Ivanov. High harmonic interferometry of multi-electron dynamics in molecules. *Nature*, 460(7258):972–977, 2009. (Cited on page 76)

[196] Shaohao Chen, Mengxi Wu, Mette B. Gaarde, and Kenneth J. Schafer. Quantum interference in attosecond transient absorption of laser-dressed helium atoms. *Physical Review A - Atomic, Molecular, and Optical Physics*, 87(3):033408, 2013. (Cited on page 77)

[197] Zhi Heng Loh, Chris H. Greene, and Stephen R. Leone. Femtosecond induced transparency and absorption in the extreme ultraviolet by coherent coupling of the He 2s2p (1Po) and 2p2 (1Se) double excitation states with 800 nm light. *Chemical Physics*, 350(1-3):7–13, 2008. (Cited on page 77)

[198] Mengxi Wu, Shaohao Chen, Mette B. Gaarde, and Kenneth J. Schafer. Time-domain perspective on Autler-Townes splitting in attosecond transient absorption of laser-dressed helium atoms. *Physical Review A - Atomic, Molecular, and Optical Physics*, 88(4):043416, 2013. (Cited on page 77)

[199] Christian Ott, Andreas Kaldun, Luca Argenti, Philipp Raith, Kristina Meyer, Martin Laux, Yizhu Zhang, Alexander Blättermann, Steffen Hagstotz, Thomas Ding, Robert Heck, Javier Madroñero, Fernando Martín, and Thomas Pfeifer. Reconstruction and control of a time-dependent two-electron wave packet. *Nature*, 516(7531):374–378, 2014. (Cited on page 77)

[200] Adrian Wirth, R. Santra, and Eleftherios Goulielmakis. Real time tracing of valence-shell electronic coherences with attosecond transient absorption spectroscopy. *Chemical Physics*, 414:149–159, 2013. (Cited on page 77)

[201] Bridgette Cooper and Vitali Averbukh. Single-photon laser-enabled auger spectroscopy for measuring attosecond electron-hole dynamics. *Physical Review Letters*, 111(8):083004, 2013. (Cited on page 88)

[202] D. Iablonskyi, K. Ueda, K. L. Ishikawa, A. S. Kheifets, P. Carpeggiani, M. Reduzzi, H. Ahmadi, A. Comby, G. Sansone, T. Csizmadia, S. Kuehn, E. Ovcharenko, T. Mazza, M. Meyer, A. Fischer, C. Callegari, O. Plekan, P. Finetti, E. Allaria, E. Ferrari, E. Roussel, D. Gauthier, L. Giannessi, and K. C. Prince. Observation and Control of Laser-Enabled Auger Decay. *Physical Review Letters*, 119 (7):073203, 2017. (Cited on page 88)

[203] P. Ranitovic, X. M. Tong, C. W. Hogle, X. Zhou, Y. Liu, N. Toshima, M. M. Murnane, and H. C. Kapteyn. Laser-enabled auger decay in rare-gas atoms. *Physical Review Letters*, 106(5):053002, 2011. (Cited on page 88)

[204] S. C. Rae and K. Burnett. Detailed simulations of plasma-induced spectral blueshifting. *Physical Review A*, 46(2):1084–1090, 1992. (Cited on page 89)

[205] Pauli Virtanen, Ralf Gommers, Travis E. Oliphant, et al. SciPy 1.0: Fundamental Algorithms for Scientific Computing in Python. *Nature Methods*, 17:261–272, 2020. (Cited on page 93)

[206] Andrew C. Brown, Gregory S.J. Armstrong, Jakub Benda, Daniel D.A. Clarke, Jack Wragg, Kathryn R. Hamilton, Zdeněk Mašín, Jimena D. Gorfinkiel, and Hugo W. van der Hart. RMT: R-matrix with time-dependence. Solving the semi-relativistic, time-dependent Schrödinger equation for general, multielectron atoms and molecules in intense, ultrashort, arbitrarily polarized laser pulses. *Computer Physics Communications*, 250:107062, 2020. (Cited on page 101)

[207] N. I. Shvetsov-Shilovski, D. Dimitrovski, and L. B. Madsen. Ionization in elliptically polarized pulses: Multielectron polarization effects and asymmetry of photoelectron momentum distributions. *Physical Review A*, 85(2):023428, 2012. (Cited on page 101)

[208] N. I. Shvetsov-Shilovski, M. Lein, and L. B. Madsen. Multielectron polarization effects in strong-field ionization: Narrowing of momentum distributions and imprints in interference structures. *Physical Review A*, 98(2):023406, 2018. (Cited on page 101)

[209] A. A. Romanov, A. A. Silaev, M. V. Frolov, and N. V. Vvedenskii. Influence of the polarization of a multielectron atom in a strong laser field on high-order harmonic generation. *Physical Review A*, 101(1):013435, 2020. (Cited on page 101)

[210] Mahmoud Abu-samha and Lars Bojer Madsen. Multielectron effects in strong-field ionization of the oriented OCS molecule. *Physical Review A*, 102(6):063111, 2020. (Cited on page 101)

[211] Mahmoud Abu-samha and Lars Bojer Madsen. Effect of multielectron polarization in the strong-field ionization of the oriented CO molecule. *Physical Review A*, 101(1):013433, 2020. (Cited on page 101)

[212] Jakub Kocák and Axel Schild. Many-electron effects of strong-field ionization described in an exact one-electron theory. *Physical Review Research*, 2(4):043365, 2020. (Cited on page 101)

[213] Anton Mikhailov. Turbo, an improved rainbow colormap for visualization. Available at: `https://ai.googleblog.com/2019/08/`, 2019. (Cited on page ii)

[214] J. D. Hunter. Matplotlib: A 2d graphics environment. *Computing in Science Engineering*, 9(3):90–95, 2007. (Cited on page ii)

Danksagung

Zu guter Letzt möchte ich mich bei all denjenigen bedanken, die zu dieser Arbeit beigetragen und mich unterstützt haben. Ein Projekt wie eine Doktorarbeit ist nie nur die Arbeit einer einzelnen Person, sondern das Ergebnis von Teamarbeit, was Konflikte, Kompromisse, Diskussionen, Austausch und die Atmosphäre in der Gruppe mit einschließt. Deshalb möchte ich allen Mitgliedern der Interatto/X-MuSIC-Gruppe danken: Ich habe viel von euch gelernt und den großartigen Teamgeist genossen.
Insbesondere möchte ich mich bedanken bei …

Prof. Dr. Thomas Pfeifer, der vor vielen Jahren durch einen Kolloquiumsvortrag mein Interesse an kurzen Laserpulsen geweckt und mir die Gelegenheit gegeben hat damit Forschung zu betreiben. Ich finde es toll, das deine Bürotür (fast) immer einen Spalt offen steht und man zum Reden bzw. zoomen vorbei kommen kann.

Prof. Dr. Selim Jochim für die Übernahme des Zweitgutachtens meiner Arbeit und seine Bemühungen uns im Grundlagenstudium die Quantenmechanik näher zu bringen.

Dr. Christian Ott für die Betreuung meines Projekts mit seinen Höhen und Tiefen. Vor allem dafür, mich in eine neue Richtungen zu stubsen, wann immer es nicht voran ging.

Dr. Alexander Blättermann als meinem spiritueller Führer. Danke für die 'Legende des weißen Mungos' und alle anderen Dinge, die du in den frühen 90ern geprägt hast.

Dem Kernteam: Dr. Veit Stooß, Dr. Paul Birk and Gergana Dimitrova Borisova, für all die Zeit im Labor und im Büro, die mich in den letzten Jahren geprägt hat. благодаря Гергана!

Thanks to Shuyuan Hu for picking up the work on attosecond streaking.

Der 'Roten Hosen Gang' Marc Rebholz und Frans Schotsch für ihren schlechten Einfluss auf mich.

I owe my deepest gratitude to Nikola Mollov for his quiet way of just keeping the laser running. Your work was easy to oversee, but was not taken for granted. много благодаря!

Dr. Thomas Ding und Dr. Martin Laux dafür, dass sie ihr Wissen und ihre Erfahrungen mit uns geteilt haben.

Meinen DoktorandenvertreterkollegInnen, insbesondere Rima Schüssler, meiner Vorgängerin, und Carina da Costa Castanheira als meiner Nachfolgerin.

Ich danke meinen Bachelor-Studenten David Wachs, Lukas Endres und Felix Herzog, die ich direkt betreut habe, und den anderen Studenten, die ich während ihrer Zeit in unserer Gruppe begleitet habe, u.a. Tobias Heldt, Sabine Rockenstein und Fabian Kaap.

Besonders dankbar bin ich Lukas, der beim Umzug ins neue Labor unermüdlich Ausrüstung hin- und hergetragen hat, um mir Zeit für die Datenauswertung zu geben, und Felix für seine Begeisterung für das Design einer neuen Zelle, die sich als Durchbruch erwiesen hat.

Prof. Andre Butz und Prof. Jörg Jäckel danke ich für die Vervollständigung meines Prüfungsausschusses.

Ich bin dankbar für die großartige technische Unterstützung an unserem Institut. Stellvertretend für die ganzen Teams, die dahinter stehen, möchte ich Herrn Spranz vom ZFT und Christian Kaiser danken.

Vielen Dank an alle Korrekturleser.

Ich danke meinen Eltern und Brüdern für ihre Unterstützung, insbesondere meiner Mutter für die gelegentlichen Fragen ”Wozu macht ihr das eigentlich?” und ”Willst du nicht langsam mal fertig werden?”.

Lia: Für alles was wir gemeinsam erlebt haben (inklusive dem verrückten letzten Jahr) und ganz besonders für Kira kann ich dir gar nicht genug danken! Ohne dich hätte ich das hier nicht geschafft.

Und dir Kira danke ich dafür, dass du in unser Leben getreten bist, alles umgekrempelt hast und jeden Tag neu mit Leben füllst!

Erklärung:

Ich versichere, dass ich diese Arbeit selbstständig verfasst, und keine anderen als die angegebenen Quellen und Hilfsmittel benutzt habe.

Heidelberg, den 20. Mai 2021 .....

Declaration:

I hereby certify that the thesis I am submitting is entirely my own original work except where otherwise indicated.

Heidelberg, May 20th 2021 .....